UNIVERSITY OF OKLAHOMA

GRADUATE COLLEGE

# IMPACTS OF LAND USE AND LAND COVER ON REMOTE SENSING ANALYSES OF THUNDERSTORMS AND THEIR ATTENDANT HAZARDS

A DISSERTATION

SUBMITTED TO THE GRADUATE FACULTY

in partial fulfillment of the requirements for the

Degree of

DOCTOR OF PHILOSOPHY

By

DARREL MICHAEL KINGFIELD
Norman, Oklahoma
2017

IMPACTS OF LAND USE AND LAND COVER ON REMOTE SENSING ANALYSES OF THUNDERSTORMS AND THEIR ATTENDANT HAZARDS

A DISSERTATION APPROVED FOR THE
DEPARTMENT OF GEOGRAPHY AND ENVIRONMENTAL SUSTAINABILITY

BY

_____
Dr. Kirsten de Beurs, Chair

_____
Dr. Jennifer Koch

_____
Dr. Mark Shafer

_____
Dr. Laurel Smith

_____
Dr. Mark Morrissey

© Copyright by DARREL MICHAEL KINGFIELD 2017
All Rights Reserved.

To Liz Quoetone; thank you for your compassion and willingness to listen to my adventureous ideas. Without you, I'd probably be lost in the Alaska wilderness, wishing I had stayed for my doctorate. We miss you every day.

# Contents

# List of Tables

# List of Figures

# Abstract

Due to their hazardous nature, most thunderstorm observations today come from remote sensing platforms such as radar, satellite, and lightning detection sensors. Advancements in these sensor networks provide the ability to identify and track thunderstorms at finer spatial and temporal scales than ever before. Thunderstorms, however, are products of interactions between the land and atmosphere with certain land use and land cover (LULC) types augmenting the frequency and intensity of thunderstorms. Yet, these LULC effects may not be directly apparent when examining the remote sensing fields in isolation. This dissertation represents three research endeavors, each containing a multi-year climatology of a unique remote sensing dataset, to examine how the addition of LULC information affects the identification of thunderstorms and their attendant hazards and the interpretation of remote sensing products.

First, a 20-year climatology of cloud-to-ground (CG) lightning data at 500 m spatial resolution quantifies an increase in isolated regions of high CG lightning frequencies in concert with the construction of antenna towers to accommodate the expansion of broadcasting and telecommunications technologies across the United States. CG lightning occurrence is correlated with antenna height and 96% of towers examined had a higher lightning density with 1 km of a tower compared to 2 km to 5 km away. Comparing tower strikes in the northern Great Plains reveals that shorter towers are more likely to observe larger CG lightning densities in the meteorological winter/fall months compared to the spring/summer months.

Second, a five-year multi-radar/multi-sensor retrospective examining the effects of city size on thunderstorm initiation and longevity reveals an increase in thunder-

storm frequency downwind of both cities larger than 1100 $km^2$ on convective days with ingredients historically shown to be conducive for urban-enhancement (i.e., summer months, afternoon initiation, synoptically weak days, non-supercell modes). As a result, downwind regions experienced a higher frequency of more intense composite reflectivity, vertically integrated liquid, and maximum expected size of hail values compared to equivalent distances upwind. Such effects were not observed in the smaller two cities and were not observed in any of the cities when examining the full five-year dataset.

Finally, Landsat 5 Thematic Mapper and Landsat 7 Enhanced Thematic Mapper Plus surface reflectance data were acquired to examine how tornadoes alter the spectral behavior of grassland, forest, and urban land cover. Generally, independent of land cover type, tornadoes tend to increase the surface reflectance in the visible and shortwave-infrared spectral bands and decrease surface reflectance as measured within the near-infrared (NIR) spectral band. This results in a higher tasseled cap brightness, lower tasseled cap greenness and wetness, and a lower Normalized Difference Vegetation Index (NDVI) values. With tornado damaged forests providing an analogous signature to forest clearing, a five-year climatology of Landsat imagery was acquired to compare NDVI, a common damage identification metric derived from the red and NIR spectral bands, to a disturbance index (DI) derived from the tasseled cap indices to examine tornado damage in forests. DI is more resilient to seasonal variability as its coefficients are derived on an image-by-image basis, making it an optimal metric for a pixel-based identification and tracking of damage and subsequent recovery.

# Chapter 1

# Introduction

## 1.1 A Brief History of Thunderstorm Observation & Remote Sensing

Thunderstorms are a byproduct of instability in Earth's atmosphere and result in the generation of lightning and precipitation with stronger thunderstorms capable of producing damaging winds, hail, and tornadoes (American Meteorological Society 2017). These phenomena likely occurred long before humans existed on Earth (Harland and Hacker 1966) and, due to the optical spectacle thunderstorms produce in the form of lightning, subsequently became integrated into religious texts of many ancient civilizations (Prinz 1977; Gary 1994; Rakov and Uman 2003). Beyond its use in stories, the ancient Greeks documented where weather occurred in both space and time for both agricultural planning and nautical exploration. These needs led to one of the first known sources of coordinated weather observation (Taub 2003). Further standardization of these observations would be driven by advancements in technology and instrumentation as meteorological phenomena such as thunderstorms do not respect geopolitical boundaries, time of year, or land use corresponding to visible aspects of place (Richards 2011).

In the United States, knowledge of how thunderstorms form has its roots in coordinated field observations over seasons and years (Galway 1992). Davis (1886) described one such field campaign occurring across New England in 1885. From this

campaign, descriptions of how thunderstorms propagate and theories on how individual smaller-scale storms are bounded by larger-scale synoptic circulations were formed. The execution of this field project required around 500 volunteers to build an observation network for data collection and communication. The limited scale at which observations were measured opened up questions as to their relevance in other parts of the United States. Regardless of these shortfalls, human collection of observations for transmission via telegraph would remain the standard method for data collection for several decades.

The study of thunderstorm hazards is not solely a meteorological problem as the damage left in its wake has multidisciplinary impacts (i.e., economic, social, physical), leading geographers during this time period to document where these hazards occurred (Montz and Tobin 2011). For example, Lemons (1942) describes a multi-year hail climatology describing occurrences by state/territory and examines the economic impacts on different crop types. However, studies like Lemons (1942) could only use in situ observations of these phenomena, assembling an incomplete picture of the hazardousness of place.

The concept of remote sensing, that is measuring attributes of a target without being in direct contact with said target, achieved widespread adoption once the technological developments occurring up to and during World War II became public knowledge (National Academies of Sciences, Engineering, and Medicine 2015). Photography had been commercially available for around a century, and while initially used to observe phenomena from the ground, cameras attached to balloons and kites showed its relevance at viewing the Earth's surface over wider areas. Photography is an example of passive remote sensing, which collect radiation emitted or reflected by an object. By World War I, cameras were mounted on airplanes as part of military reconnaissance missions (Campbell and Wynne 2011). In World War II, the need to track enemy movements at long ranges precipitated advancements in existing radio detection and

ranging (hereafter referred to as radar) technologies (Whiton et al. 1998a). Radar is an active remote sensing system that emits energy and measures the backscattered energy from the target to discriminate its attributes (e.g., distance, speed, size). In addition to returns from aircraft, echoes from thunderstorms were also being measured on radar (Whiton et al. 1998a). Concerns over the potential of weather contaminating the signal from military aircraft resulted in initial studies post-World War II related to how precipitation echoes affect the backscatter and attenuation characteristics of radar (Maynard 1945; Ryde 1946; Bent 1946; Probert-Jones 1990). These studies laid the foundation for the formation of ground-based networks of Doppler weather radars in the United States and abroad (Whiton et al. 1998a,b). Subsequent advancements in signal/image processing techniques and the portability of radar allowed for detailed examination of thunderstorm processes (e.g., Stout and Huff 1953; Atlas 1963; Brown et al. 1971; Ray et al. 1975; Davies-Jones et al. 1978). Spatiotemporal and intensity patterns documented in thunderstorms using Doppler radar over the decades provided the ability to create conceptual models for how thunderstorms form (e.g., Lemon and III 1979; Markowski 2002) and persist in different environments.

Since many of these radar/thunderstorm relationships occurred after World War II, another system was extensively used to identify the locations of thunderstorms. Lightning is not only visible to our eyes but also emits a broadband radio frequency pulse (i.e., sferic) that spans from the very low frequency (VLF, 3 kHz) to the very high frequency (VHF, 300 MHz) ranges of the electromagnetic spectrum (Rakov and Uman 2003). The Watson-Watt and Herd cathode ray direction finder (DF) used two antennas listening at 10 kHz to detect the magnetic field produced by lightning (Watson-Watt and Herd 1926; Cummins et al. 1998a). One DF could take this information and determine the direction of the lightning discharge. Taking the direction vectors from two DFs allowed for the identification of lightning location. The DF technique was the common way to detect lightning until Lewis et al. (1960) introduced an alternative

approach called time-of-arrival (TOA). By setting up a network of time-synchronized instruments and knowing when the sferic signal reaches each sensor, lightning location could be derived by examining the arrival time differences within the sensor network.

Improvements in direction finding hardware and software (Krider et al. 1976) lead to the implementation of regional lightning detection networks across the United States (Krider et al. 1980; Orville et al. 1983; Mach et al. 1986). In a similar fashion to the problems of scale faced in early observations of thunderstorms, there was an increased demand to merge these regional networks together to form a national observation network. From 1984 – 1988, these regional networks were combined, creating the National Lightning Detection Network (NLDN; Cummins et al. 1998a; Orville 2008). Since its inception, this network has been a cornerstone in developing seasonal and temporal relationships to lightning occurrence (Holle et al. 2016), establishing relationships with thunderstorm hazards (Schultz et al. 2011), and environmental conditions for different lightning polarities (Carey and Buffalo 2007).

Advancements in processing and dissemination technology not only aided in the assembly of radar and lightning remote sensing networks, but also the creation of satellite constellations that provide synoptic views of the Earth from space. As early as 1946, the U.S. military gathered information on how to design and launch an earth-observing satellite (RAND Corporation 1946; Lauer et al. 1997). The launch of Sputnik 1 in 1957 served as an impetus for rapid resource allocation to develop such satellites. In response to Sputnik, the 1958 National Aeronautics and Space Act created the National Aeronautics and Space Administration (NASA) and identified parallel military and civilian space exploration and exploitation endeavors (Mark 1988). This endeavor led to the construction and launch of satellites to monitor Earth's radiation budget (e.g., Explorer 6), take pictures of clouds and other meteorological phenomenon (e.g., Television and Infrared Observational Satellite (TIROS)), and examine land and water ecosystems on the Earth's surface (e.g., Landsat) (House et al. 1986; Lauer et al.

1997).

These initial satellites provided a ubiquitous view of meteorological features that could be compared to other radar and lightning systems. (Whitney Jr. 1963) documented cloud attributes from severe thunderstorms using TIROS-I satellite imagery and compared the signatures to terrestrial remote sensing systems. These initial observations laid the framework for future research endeavors identifying new thunderstorm features from initial case studies to long-term climatologies (Boucher 1967; Adler and Fenn 1979; McCann 1983; Heymsfield et al. 1991; Roberts and Rutledge 2003; Dworak et al. 2012). What TIROS did for atmospheric observations, Landsat did for land observations. The ability to examine human feedback on the Earth system through multispectral bands led to significant advancements in land cover identification, ecological modeling, and the launch of additional earth observation satellites (Cohen and Goward 2004). Satellite-derived land cover classification has greatly improved model parameterizations of land surface processes (i.e., heat fluxes, moisture) for forecasting meteorological phenomena, particularly around cities (e.g., Chen et al. 2011). In 2008, after 35 years of data acquisition, the Landsat archive became freely accessible (Woodcock et al. 2008; Wulder et al. 2012) opening the door for a greater integration within the meteorology community in the years ahead (e.g., Jedlovec et al. 2006). In addition to understanding the morphology of thunderstorms, these terrestrial and spaceborne technologies propelled the geographical study of natural hazard occurrence, leading to advances in analyses of risk, vulnerability, and disaster mitigation policy (Tobin and Montz 2004; Montz and Tobin 2011).

## 1.2 Research Overview

Much of what we know about thunderstorms today comes from multi-year observational retrospectives using remote sensing systems, a tool with a genealogy tracing

back to geography (Sheng 2011 and references therein). These data represent thunderstorms and their associated hazards in a form of absolute space (i.e., via mathematical/geospatial grids); however, thunderstorms are a product of relative space with both atmospheric (e.g., pressure systems, planetary waves) and terrestrial (e.g., heat fluxes, moisture transport) feedbacks on various scales affecting its timing and intensity.

Terrestrial features are comprised of physical (i.e., rock, soil), biological (i.e., plants, ecosystems), and cultural (i.e., land use, human modification) layers that combine to form a landscape; a key concept through the lens of physical geography (Antrop 2000; Gray 2009; Friess and Jazeel 2017). For many centuries, land use and land cover (LULC) change have substantially altered the natural landscape to accommodate human migration and socioeconomic demands (Foley et al. 2005). Examples of these changes include deforestation for infrastructure, expansion of agricultural output, and the creation/expansion of urbanized areas. These changing landscapes affect several surface characteristics (e.g., albedo, imperviousness, heat capacity) that alter Earth/atmospheric feedbacks at various scales (Pielke et al. 1991; Bonan 2001; Arnfield 2003; McPherson and Stensrud 2005; Pielke et al. 2007).

In concert with advancements in computing technology, numerical modeling systems used to forecast thunderstorms are able to capture information at spatial resolutions $\leq$ 1 km, allowing for the transfer of energy and momentum between the Earth's surface and lower atmosphere to be simulated (Trusilova et al. 2015). Since these feedbacks are dependent on LULC type, recent studies examine how to best represent these data in model simulations (e.g., Nemunaitis-Berry et al. 2017; Reames and Stensrud 2017). Remote sensing systems also have the ability to resolve information at resolutions $\leq$ 1 km; however, the role LULC plays in data capture and interpretation from these systems is dependent on the system employed and is an underexplored topic. This dissertation examines how prerequisite knowledge of LULC affects the collection and interpretation of remotely sensed observations of thunderstorms and

their attendant hazards. Each chapter corresponds to a multi-year retrospective using a unique remote sensing system and LULC dataset and is formatted as individual research articles for entry into peer-reviewed journals.

Chapter 2 examines lightning, the hazard that defines a thunderstorm. Around 1.4 billion lightning flashes occur across the earth each year (Christian et al. 2003). Lightning flashes take on two forms, those that remain in the cloud (i.e., intracloud or IC) and those that strike the ground (i.e., cloud-to-ground or CG). There generally are more IC flashes than CG strikes and this ratio is geographically dependent (Boccippio et al. 2001). Yet, CG lightning is more dangerous to life and property than IC flashes, resulting in a greater demand to detect its occurrence (Curran et al. 2000). Since 1995, the NLDN has been collecting observations of CG lightning occurrence with a median locational accuracy of around 500 m (Cummins and Murphy 2009). However, most studies map CG lightning occurrence at a coarser spatial resolution (~20 km; see review by Holle et al. 2016). At this coarse resolution, many different LULC types could be in a grid cell. This raised my initial question; do specific LULC types attract more lightning than others?

The initial hypothesis was that cities observe a higher frequency of lightning than non-city areas. However, in performing an exploratory analysis, it was discovered that a majority of grid cells with high lightning counts were displaced from cities. This led to a manual examination of these grid cells where it was subsequently observed that an antenna tower existed at most of these locations. Due to the coarse resolution chosen by past researchers studying the climatological distribution of lightning, these tower-based effects were being smoothed out. It is common knowledge that lightning has a propensity to strike tall artificial structures over natural elevation of equivalent height (McEachron 1939; Berger and Vogelsanger 1969), however, many analyses of tower-triggered lightning are focused in a fixed geographic location or encompass a single lightning producing event (Wang et al. 2008; Warner et al. 2012, 2014). With

20-years of NLDN lightning data, chapter 2 represents the highest spatial and temporal resolution analysis and largest climatology of tower-induced lightning to date. This chapter was accepted for publication in Geophysical Research Letters pending additional revisions.

Chapter 3 examines the role of city size in the augmentation of thunderstorms that pass over a city. The conversion from natural to urban land cover is an extreme case of LULC change (Shepherd 2005) dramatically altering the (1) heat capacity and causing urban heat islands (UHIs; Oke 1987); (2) percentage of impervious surfaces and surface roughness (e.g., Thielen et al. 2000); and (3) composition of atmospheric aerosols (e.g., van den Heever and Cotton 2007). Many of these variables are correlated with urban size (Oke 1973; Schmid and Niyogi 2013) with larger cities generally having higher temperatures compared to rural areas. Given that over half of the global population resides in urban areas, there is a precedent to continue studying these urban influences on the Earth/atmosphere system (see review by Mitra and Shepherd 2016).

This chapter describes an innovative set of methods to blend information from 19 Weather Service Radar 1988 Doppler (WSR-88D) sites, NLDN lightning, and model analysis data, into a 3D cube of data at least 1 km spatial and 1 min. temporal resolution. Thunderstorms were automatically defined and tracked through four cities of variable size located in the United States Great Plains. Values of composite reflectivity, a common radar-derived metric used in other studies (e.g. Ashley et al. 2012; Haberlie et al. 2015) in addition to two vertically integrated products novel to this field of study were quantified upwind and downwind of each city. This chapter was accepted for publication in the Journal of Applied Meteorology and Climatology pending additional revisions.

Chapter 4 migrates from hazard identification to response. Knowing where thunderstorm hazards (i.e., wind, hail, tornadoes) occur is valuable in determining a climatological frequency of such events for forecasting; however, there tends to be a

population bias with hazard reporting (King 1997; Doswell III et al. 2005). After tornadoes, National Weather Service (NWS) employees will perform a damage survey to document the damage that occurred; however, they tend to focus in urban areas as a majority of the Enhanced Fujita (EF; Wind Science and Engineering Center 2006) scale guidance is focused on human-made structures. In addition, urban areas generally consist of a higher population density, allowing more opportunities to report a hazard occurrence in contrast to rural areas with a lower population density. This has led to several papers recommending the use of multispectral satellite imagery to provide a synoptic view of the tornado damage track (e.g., Yuan et al. 2002; Jedlovec et al. 2006; Molthan et al. 2014) by using image-processing techniques.

Granted, image-processing techniques can highlight where damage occurred, however heretofore, a comprehensive study examining how tornadoes alter the spectral response of different LULC types has not been performed. Chapter 4 first examines how tornadoes alter the spectral behavior of the visible, near-infrared, and shortwave infrared wavelength regions captured by the Landsat 5 Thematic Mapper and Landsat 7 Enhanced Thematic Mapper Plus for urban, grassland, and forest land cover. These individual bands are used to calculate common image-transformation products such as the Normalized Difference Vegetation Index (NDVI; Rouse Jr. et al. 1973; Tucker 1979) and Tasseled Cap Indices (Kauth and Thomas 1976). Focusing on forest damage, an area not typically examined in ground-based damage surveys, Chapter 4 examines five years of Landsat imagery around one tornado outbreak to evaluate a Disturbance Index (DI; Healey et al. 2005), commonly used in ecological studies, to NDVI in both identifying initial tornado damage and monitoring damage recovery. This chapter was published in the Journal of Applied Meteorology and Climatology in April 2017. Additionally, the American Meteorological Society named this article a "Paper of Note", allowing for an expedited version of this paper to be published in the April 2017 issue of the Bulletin of the American Meteorological Society.

# Chapter 2

# Antenna Structures and Cloud-to-Ground Lightning Location: 1995–2015


## Abstract

Spatial analyses of cloud-to-ground (CG) lightning occurrence due to a rapid expansion in the number of antenna towers across the country are explored by gridding 20-years of National Lightning Detection Network (NLDN) data at 500 m spatial resolution. 99.8% of grid cells with $>$ 100 CGs were within 1 km of an antenna tower registered with the Federal Communications Commission. Tower height is positively correlated with CG occurrence; towers taller than 400 m AGL experience a median increase of 150% in CG lightning density compared to a region 2 km to 5 km away. In the northern Great Plains, the cumulative CG lightning density near the tower was around 138% (117%) higher than a region 2 to 5 km away in the September – February (March – August) months. Enhanced CG frequencies typically also occur in the first full year following new tower construction, creating new hot spots.


## 2.1 Introduction

For over 80 years, tall structures have facilitated analyses on lightning production and its electrical characteristics (McEachron 1939; Rakov and Uman 2003). In the last 30 years, humankind has observed an expansion in digital technologies and broad-

casting capabilities (Hilbert and López 2011). Concomitant to this expansion is the construction of antenna towers across the continental United States (CONUS) with the number of Federal Communications Commission (FCC) antenna registrations increasing from 38,514 before 1995 to 130,883 after 2015. In 1995, the National Lightning Detection Network (NLDN), a lightning location system covering North America, was renovated with updated sensors to improve cloud-to-ground (CG) detection efficiency (80%–90% for flashes $\geq$ 5 kA) and location accuracy (median error ~500 m) (Cummins et al. 1998b). Continued investment through the turn of the century has further improved these detection metrics with a uniform CG detection efficiency of 95% and a variable detection efficiency for cloud flashes (~16%–40%) (Cummins and Murphy 2009).

The performance of the NLDN has made it an essential tool in documenting the spatiotemporal distribution of lightning into maps, as reviewed by Holle et al. (2016). Due to the wide spatial area examined, many climatological studies rely on coarse gridding techniques ($\geq$ 20 km) to summarize CG occurrence, disregarding smaller-scale features (e.g., antenna towers) that could alter the frequency of lightning. Berger and Vogelsanger (1969) observed that lightning initiation was more prevalent from towers compared to mountain peaks of equal elevation, resulting in isolated regions of elevated lightning occurrence. The type of lightning occurring near a human-made structure can be either downward or upward (Rakov and Uman 2003) with upward lightning documented to occur with either the presence or lack of nearby flash activity (Wang et al. 2008; Mazur and Ruhnke 2011; Warner et al. 2012; Zhou et al. 2012). Contemporary studies have examined this human-made modification in lightning using NLDN in the CONUS (Stanley and Heavner 2003; Warner et al. 2012, 2014), Canada (Lafkovici et al. 2008), with analogous evaluations in Europe (Diendorfer et al. 2009; Azadifar et al. 2016) and Asia (Wang et al. 2008; Chen et al. 2012). These studies have encompassed a limited geographic domain and/or a particular season; however, both

geographic and seasonal mechanisms drive where lightning occurs (Holle et al. 2016).

This study provides a geographic perspective on the prevalence of tower-initiated lightning by first examining lightning occurrence across the CONUS through a 20-year, 500 m spatial gridding of NLDN data. The spatial association of elevated CG lightning locations to FCC towers and the effects of tower height, age, and season have in modifying the local lightning density are addressed herein.

## 2.2 Data & Methods

### 2.2.1 NLDN

The National Severe Storms Laboratory maintains an archive of quality-controlled NLDN data back to the first full operational year in 1989. Information regarding the detection time, location, polarity, and multiplicity were recorded for each CG strike. Our study period starts in 1995 following the first network upgrade (Cummins et al. 1998b) However, this upgrade also increased the detection efficiency of lower amplitude events, which several studies reveal to be intracloud (IC) flashes (e.g., Cummins et al. 1998b; Biagi et al. 2007; Cummins and Murphy 2009; Fleenor et al. 2009; Emersic et al. 2011). Following their suggestions and to increase the confidence in the NLDN detections being CGs, all positive CGs (+CGs) and negative CGs (–CGs) with a peak current less than 15 kA and 10 kA respectively were discarded. This removed 46.5% (23.7%) of +CGs (–CGs) detected over the 20-year period. With a focused interest in FCC-registered towers, the 29,196,768 +CGs and 316,893,494 –CGs detected over the CONUS were gridded at 500 m spatial resolution (Fig. 2.1a).

### 2.2.2 Antenna Tower Locations

The FCC Antenna Structure Registration database contains records of construction history, location, and heights for all new and proposed structures that require notification to the Federal Aviation Administration. This database is updated daily and when queried had 130,883 records with a construction date before 1 January 2016. From these records, 1,725 towers had a height above ground level (AGL) exceeding 200 m. The spatiotemporal accuracy of these towers were evaluated using satellite imagery within Google Earth. In 77 cases, a tower was missing or was located within 500 m of another tower. In cases where two towers were collocated, the taller tower was retained and the smaller tower was removed. In 45 cases where towers were demolished and replaced, these records were combined with the mean of the two tower heights recorded. Querying the tower proposal applications revealed seven cases where construction occurred but no FCC paperwork was filed. These towers were included and had their construction dates estimated by finding the first satellite image date where the tower existed. After quality control, 1,610 towers exceeding 200 m remained in the database. In order to examine the effects of tower height on lightning frequency while normalizing for thunderstorm occurrence, we first applied a 10 km spatial buffer to each of the towers exceeding 200 m and removed towers that overlapped spatially. This reduced the number of towers to 675. To maintain a consistent 20-year study period around each tower, only the 443 towers built before 1995 were examined (Fig. 2.3 b,c). These towers had their lightning density calculated within 1 km (inner domain) and between 2 km to 5 km away (outer domain). Finally, locations with a low thunderstorm occurrence could produce outliers when comparing the flash densities between these domains. This was mitigated by removing eight towers where the outer domain flash density was fewer than two flashes per $km^2$.

## 2.3 Results

The 20-year CG lightning climatology spatially reveals an increase in lightning occurrence from the northwest to southeast regions of the CONUS (Fig. 2.1a), comparable to observations in Holle et al. (2016). A spatially continuous region of enhanced lightning frequencies were observed along the coastline of the Gulf Coast states and extending northward up to North Carolina. A primary driver for this enhancement is the creation of land and sea breeze driven moisture convergence zones creating favorable thunderstorm updraft environments (e.g., Hill et al. 2010). The high spatial resolution of this climatology reveals an exponential decline in the percentage of CONUS area with higher lightning frequencies (Fig. 2.1b). The number of grid cells with 40+ CGs only makes up around 1% of the CONUS area but corresponds to approximately 4.25% of the cumulative 20-year lightning frequency (N=346,090,262).

While the southeast CONUS, particularly near the coastline, provides a conducive environment for enhanced lightning production, grid cells exceeding progressively higher CG counts are located away from this region (Fig. 2.2) At 75+ CGs (N=1,412; not shown), only 52.2% of grid cells were located $>$100 km from the southeastern coastline (gray shading; Fig. 2.2). At 100+ CGs (N=613) and 200+ CGs (N=154), 76.2% and 81.2% of the grid cells were located $>$100 km away from the coasts. Localized cells of higher CG counts are prevalent across the Great Plains, Midwest, and Ohio Valley regions. The highest CG count in a single grid cell (619) was located at 35.81°N/94.03°W, around 19 mi (30.5 km) southeast of Fayetteville, Arkansas.

Overlaying the entire FCC database reveals that 99.8% of grid cells with 100+ CGs also had a tower located within 1 km of its center (Fig. 2.3a) The single location with no FCC tower was located in Georgia where visual examination reveals a naval communications tower that likely contributed to the 105 CGs registered in this area. 98.2% (24.8%) of matches were associated with a tower height exceeding 200 (500)

m. Tower height is correlated with lightning occurrence with towers exceeding 500 m having a median frequency of 173 CGs compared to 138 CGs around shorter towers. In 76.6% of cases, the tallest tower existed prior to 1996 (Fig. 2.3b). Towers built before 1996 had a wider range of CG counts (100 to 619) compared to towers built after 1996 (100 to 465).

Departing from fixed CG frequency thresholds and examining modifications in lightning density around towers again reveals a positive correlation with height (Fig. 2.4a). Around 96% of the 435 isolated towers had a higher lightning density within 1 km from the tower (inner domain) compared to the density measured 2 km to 5 km away (outer domain). The median increase was 29% for towers between 200 m to 300 m tall and up to around 150% for towers $>$ 400 m tall. A comparison of peak currents by domain shows a larger overall percentage of –CGs and +CGs registered a higher peak current within the inner domain (Fig. 2.4b). This separation is more defined for –CGs with approximately 30% (22%) of inner (outer) domain –CGs having a peak current $>$ 30 kA. For +CGs, the separation in the distributions is smaller with the difference between the two probabilities never exceeding 2%. Yet, the +CG distribution in the inner domain yields a higher probability of occurrence between 16 kA and 84 kA. Thus, there is a strong likelihood that ground flashes either initiated by or interacting with these towers typically have higher peak amplitudes than non-tower flashes.

Mapping the percent change in the inner region (Fig. 2.4c) reveals that much of the CONUS experiences up to a 100% increase in the inner domain lightning density compared to the outer domain, particularly through the south-central and southeast CONUS. The northern Great Plains and upper Midwest (i.e., Nebraska northward and eastward to Michigan) measure larger departures with 47% of towers in these states having an inner domain CG density at least 100% higher over the outer domain. In 87% of these cases, these towers were $>$ 300 m. The highest percentage change of

631% occurred near a 512 m tower in Wisconsin (45.66°N/89.21°W) where 159 (22) CGs/km$^2$ occurred within the inner (outer) domains.

This region is also prone to experiencing both rain and snowfall regimes compared to southern latitudes (e.g., Groisman and Easterling 1994). Segmenting lightning occurrence into either the cold season (meteorological fall/winter; Fig. 2.5a) or warm season (meteorological spring/summer; Fig. 2.5b) reveals that 94% (98%) of cold (warm) season towers (N=100) had an elevated CG density in the inner domain. While a greater percentage of towers had an overall increase in CG density during the warm season, more towers exhibited a greater positive increase in CG density in the inner domain during the cold season. Eight towers (343 m to 609 m) had a 400%+ increase in CG density in the cold season compared to three warm season towers (457 m to 609 m). Accumulating these densities by season reveals that the inner domain had a 138% (117%) higher lightning density in the cold (warm) season. Segmenting by polarity yields that around 94% (86%) of CGs in the inner (outer) domain were –CGs in both seasons. The percentage of –CGs is correlated with tower height and reaches 95% in regions where the tower height exceeds 400 m.

Heretofore the tower dataset has been constrained to construction dates prior to 1995. For the 236 towers $>$ 200 m tall and built after 1 January 1995, approximately 74% had a higher inner domain CG density the year following construction. For the ten towers taller than 500 m, nine measured a higher inner domain CG density in the next full year. This elevated CG density persists and is observable across different CONUS regions (Fig. 2.6) For example, in Colorado, the inner domain saw a four-fold increase in lightning density (~10 CGs/km$^2$) in 2004 after construction of a 608 m tower. Similar trends are seen in other states where many of the yearly CG densities in the outer domain are $<$ 7.5 CGs/km$^2$ while towered locations frequently see higher densities, up to 27.5 CGs/km$^2$ as measured near a 609 m tower in Oklahoma in 2015.

## 2.4 Discussion

While it has long been understood that lightning is attracted to and initiated by tall objects (e.g., Mazur and Ruhnke 2011), the change in CG density (e.g., median ~150% increase for towers $>$ 400 m) near towers throughout the CONUS is more than a natural occurrence. Some flashes are likely the result of natural terminations; however, it is highly likely that others were either lightning-triggered or self-initiated upward lightning (e.g., Wang et al. 2008; Mazur and Ruhnke 2011; Warner et al. 2014). Thus, a majority of flashes would not have occurred in the absence of a tower.

Supporting evidence of upward lightning is seen with a greater percentage of –CGs occurring near the tower (95%) compared to further away (84%). As noted by both Mazur and Ruhnke (2011) and Warner et al. (2012), initial positive upward leaders from towers are unlikely to be recorded by the NLDN due to their low continuing current. Once an attachment happens, connecting with either a preceding IC flash or following a subsequent initiation within the storm charge center, the recoil streamers and/or return strokes will be recorded as a –CG or potentially multiple –CGs. This is likely why the overall percentage of –CGs is correlated with tower height.

The peak currents of flashes interacting with towers or other tall objects have so far only been evaluated in limited case studies (e.g., Garolera et al. 2015). Within this study, the population of –CGs and +CGs near a tower generally had a higher peak current than the population of flashes in the outer region. These differences were larger with –CGs (~8% more $>$ 30 kA) than +CGs. Overall, this could infer that tower-initiated lightning may provoke a larger charge transfer compared to natural lightning, noting, however, the caveats outlined in Warner et al. (2012) on the accuracy and polarity NLDN assigns to certain tower-initiated strikes.

As expected, CG lightning is less common during the colder months (September – February). In the northern Great Plains, there were 84% fewer CGs during this

period. Uniquely, however, shorter towers ($>$ 340 m) in this region registered higher CG densities (i.e., eight towers $>$ 400%) compared to their outer domains in the cold season. Furthermore, 56% of towers also registered a higher percentage change in the cold season over the warm season. This is indicative of towers being more susceptible to lightning due in part to generally lower altitude cloud bases and charging regions observed in winter convective modes (Schultz and Vavrek 2009).

This study is limited to isolated towers ($>$ 10 km), therefore we cannot examine more complex relationships such as concurrent return strokes by multiple towers (e.g., Kitterman 1981; Lu et al. 2009; Warner et al. 2012). Additionally, studies comparing video capture with NLDN reports note that many discharges are missed by the NLDN, possibly due to their low peak current (e.g., Warner et al. 2012). In addition to these flashes not detected by the NLDN, many more may be discarded in our study due to the thresholding of NLDN data to $>$ 10 kA (–CGs) and 15 kA (+CGs). Thus, there is likely an even higher percentage increase in lightning occurrence near towers than is reflected here.

In the future, the strong relationship between amplified CG rates and towers may allow for the use of CG lightning records to determine the construction dates of tall structures in the absence of formal records. The examples in Fig. 2.6 all denote an elevated lightning density by more than 100% in the year following construction. Though these flashes represent a small percentage of the overall NLDN record, continued construction of new structures could increase the number of lightning hot spots across the CONUS.

## 2.5 Summary

A 20-year, high-resolution (500 m) climatology of NLDN CG lightning reveals that while enhanced lightning occurrence is more prevalent along the coastline in the south-

eastern CONUS, isolated spatial peaks in lightning frequency ($>$ 100 CGs) could be observed in locations extending throughout the central CONUS. Subsequently, this study is the first to document and quantify the spatial distribution of highly localized lightning enhancements caused by human-made structures across the CONUS. Given the close spatial associations between towers and lightning maxima, we feel NLDN serves as a beneficial tool not only in broad mapping analyses of lightning occurrence, but also in documenting and examining these smaller-scale influences.

A majority of pixels with $>$ 100 CGs were located at least 100 km inland. Spatial comparisons with FCC towers reveal that all grid cells exceeding 105 CGs had a registered tower within 1 km. Additionally, 76.7% of matching towers were constructed before 1995, allowing for two decades of thunderstorm opportunities and tower interactions. CG frequency was positively correlated with tower height with 98.2% of matching towers having a height $>$ 200 m.

This positive correlation was corroborated when comparing the lightning densities within 1 km from a tower to an area 2 km to 5 km away. 96% of towers had a higher density closer to the tower with the median percentage increase being around 29% for towers between 200 m to 300 m and increasing to around 150% for towers above 400 m. These departures are amplified in the north-central CONUS where towers are generally struck by a higher percentage of less-frequent thunderstorm events compared to the southeast CONUS where thunderstorm events are more prevalent. This departure in CG density is even more disparate in the fall/winter months with towered locations seeing a higher overall percentage of lightning compared to events in the spring/summer months. Additionally, a four-fold increase in CG densities were measured around shorter tower heights during the cold season. Finally, these trends were also observed around new tower constructions. In the five towers examined, there was a three-fold increase in the lightning density within 1 km of the tower in the first year post-construction, even in regions with fewer thunderstorm opportunities. This is a

notable concern as additional communications and wind power turbines (e.g., Hitaj 2013) fill the skyline in the future.

## Acknowledgements

The authors thank Patrick Marsh for his guidance on gridding the lightning data. Funding was provided by the NOAA/Office of Oceanic and Atmospheric Research under the NOAA-University of Oklahoma Cooperative Agreement #NA11OAR4320072, U.S. Department of Commerce and the NASA Interdisciplinary Science Program project NNX12AM89G. The views expressed here are those of the authors and do not necessarily represent those of the NOAA, NSSL, or CIMMS.

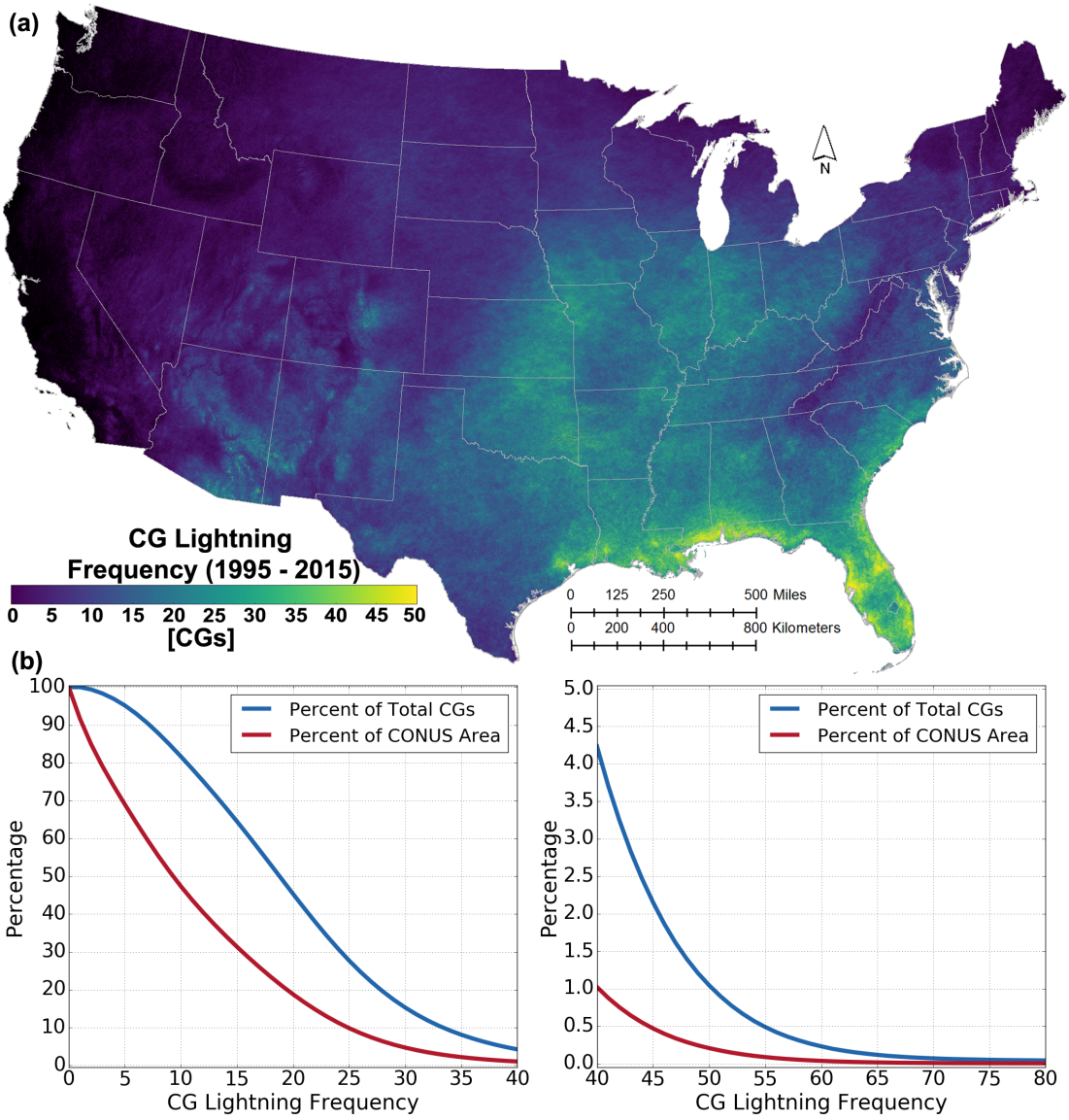


Figure 2.1: (a) A 20-year 500 m spatial resolution map of lightning frequency and associated CDF plots summarizing (b) the accumulated percentage of total CGs (blue line) and CONUS area (red line) exceeding a specified CG threshold. Around 10% of the CONUS area had no CGs and 1% had 40+ CGs.

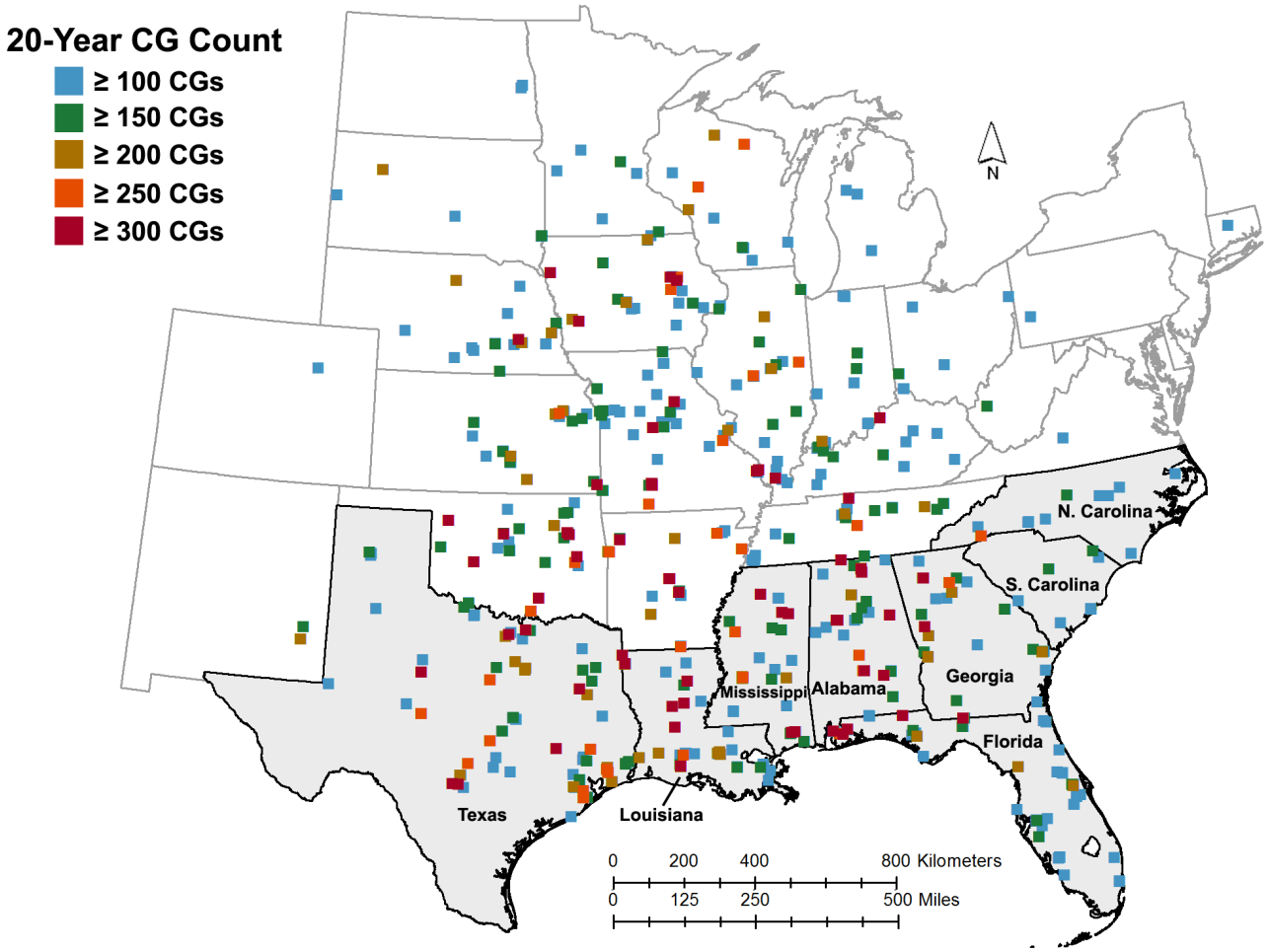


Figure 2.2: Map of grid cells exceeding 100 CGs (light blue boxes) up to 300 CGs (red boxes). The southeastern states are labelled and shaded in gray.

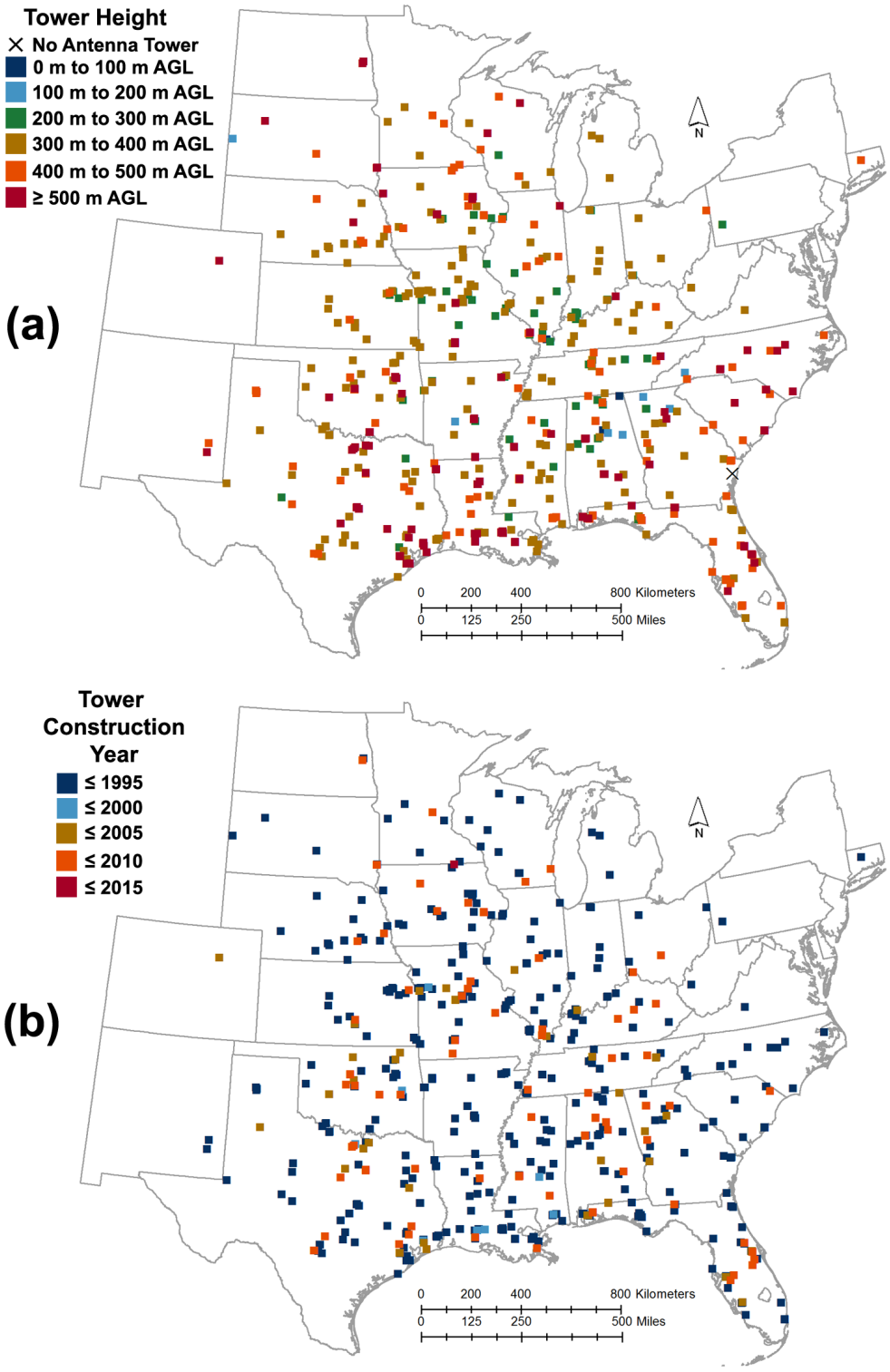


Figure 2.3: At locations where an FCC tower was within 1 km of a grid cell in Figure 2.2, the tallest tower had its (a) maximum height (AGL) and (b) construction date plotted. Cells with no FCC-registered tower are marked with an 'X' in (a)

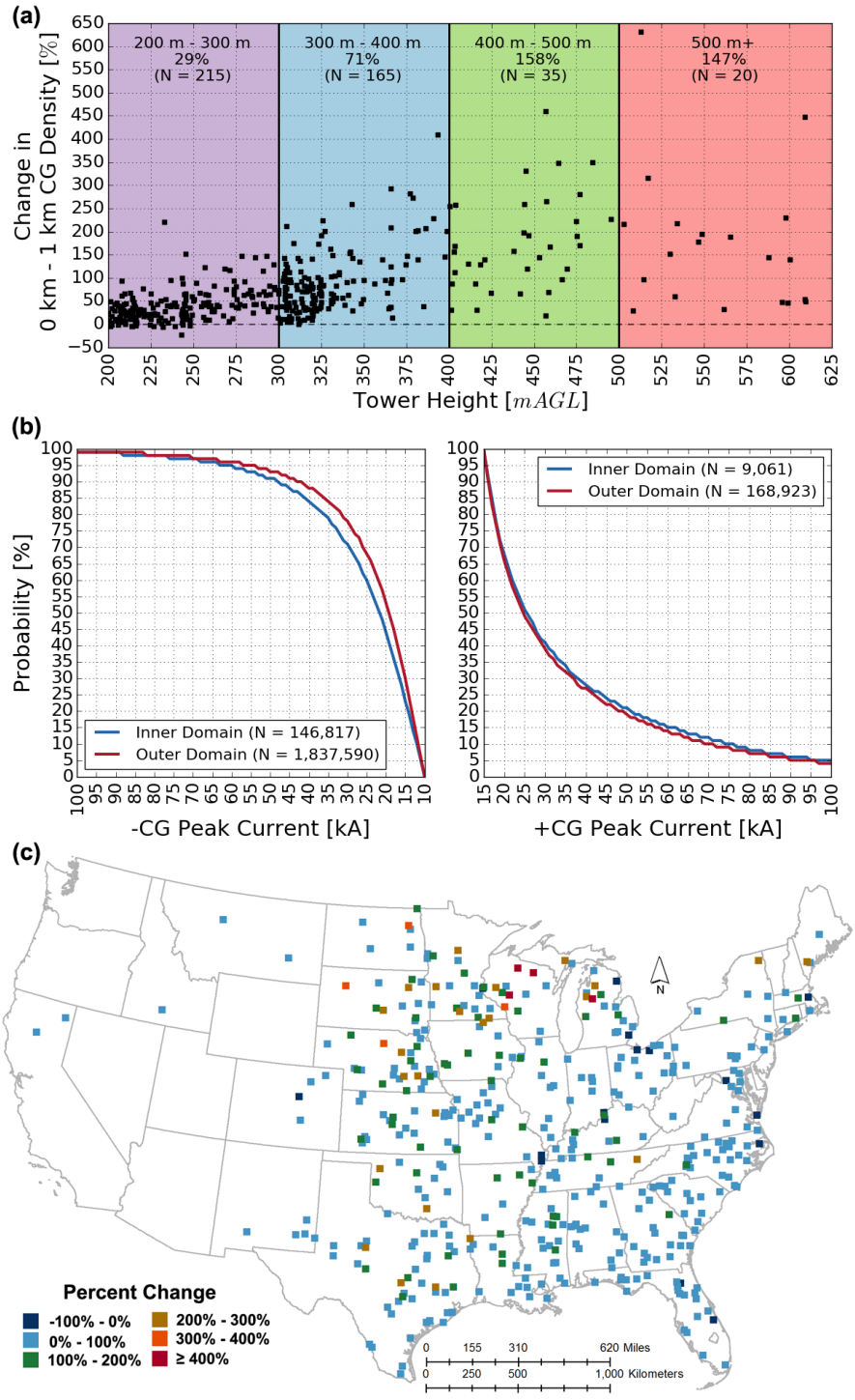


Figure 2.4: (a) Scatterplot of the percent departure in CG density measured within the inner and outer domains and segmented by tower height. The median percent change at 100 m intervals is annotated in each region. (b) CDF plots of peak current measured in the inner and outer domains by polarity. (c) A map of the percent change for the 435 FCC towers that were $\geq$ 200 m AGL and further than 10 km from another FCC tower $\geq$ 200 m AGL.

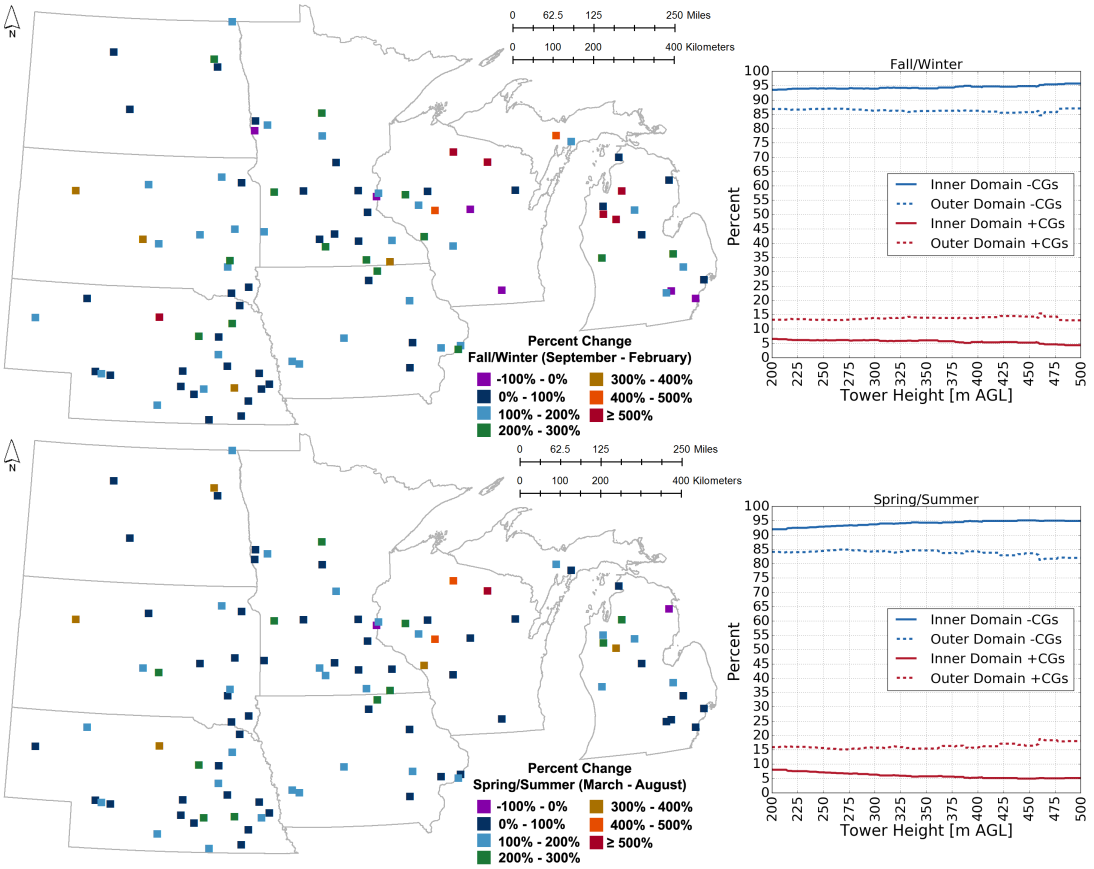


Figure 2.5: The percent change in CG density within 1 km of an antenna tower (inner domain) compared to 2–5 km away (outer domain) associated with CG producing events in the meteorological fall/winter months (top) and spring/summer months (bottom). The plots on the right correspond to the percentage of –CGs and +CGs measured in both domains as a function of tower height.

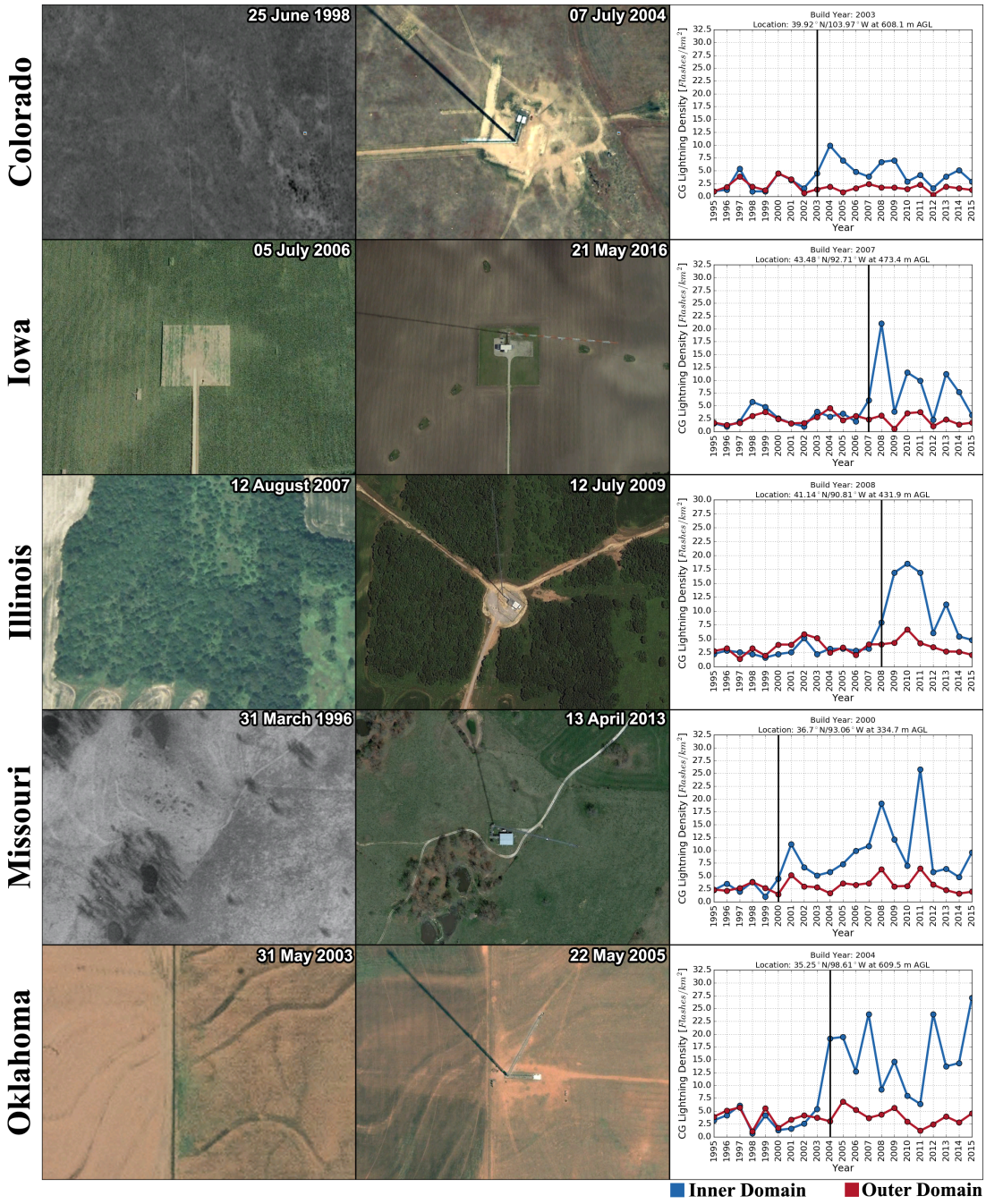


Figure 2.6: Google Earth imagery before (left column) and after (middle column) the construction of antenna towers along with a 20-year time-series of the yearly CG densities in the inner (blue line) and outer (red line) domains (right column). Construction years are marked with a black line in each time-series plot and clearly show an elevated CG density near each tower after construction.

# Chapter 3

# Effects of City Size on Thunderstorm Evolution Revealed through a Multi-Radar Climatology of the Central United States


## Abstract

Five years of 0.01°-by-0.01° multi-radar multi-sensor grids were assembled using radar, model, and cloud-to-ground lightning data to examine how city size augments thunderstorms around four cities: Dallas/Ft. Worth, TX; Minneapolis/St. Paul, MN; Oklahoma City, OK; and Omaha, NE. Thunderstorms were identified every minute using an automated storm tracking algorithm to collect values of composite reflectivity, vertically integrated liquid (VIL), and maximum expected size of hail (MESH). These fields were analyzed by independently sampling the maximum every 10 min., and accumulating its spatial footprint. Upwind and downwind regions were defined on a case-by-case basis using the mean storm motion. In addition to examining the full climatology of events, an urban favorable (UF) subset of non-supercells occurring in the late afternoon/evening in the meteorological summer on weak synoptically forced days were also examined.

In the full climatology, regions at variable ranges upwind of each city generally had stronger signatures and higher areal mean values of reflectivity, VIL, and MESH. In the UF subset, the larger two cities (Dallas/Ft. Worth and Minneapolis/St. Paul) had a 24%

- 50% increase in the number of downwind thunderstorms, resulting in an increase in the frequency of stronger radar-based values and a higher overall downwind areal mean reflectivity, VIL, and MESH. The two smaller cities - Oklahoma City and Omaha - do not show a uniform change in these radar parameters in the UF subset. This pattern suggests that larger cities could increase thunderstorm occurrence and their intensity downwind of the prevailing flow under appropriate environmental conditions.

## 3.1 Introduction

The rate of urbanization by the global population is on an upward trend, from 30% in 1950 to 54% today, with two-thirds of the world projected to be living in urban areas by 2050 (United Nations 2014). Population redistribution concomitant with economic development have resulted in many cities across the world experiencing an urban area expansion at more than double the rate of their respective urban population growth in the latter portion of the 20th century (Angel et al. 2011). Expanding urban landscapes reduce local biodiversity and enhance surface roughness due to the spatial distribution of impervious surfaces (Thielen et al. 2000; Seto et al. 2012), modify the atmospheric contributions of aerosols (van den Heever and Cotton 2007; Rosenfeld et al. 2008; Ntelekos et al. 2009), and alter surface energy budgets to generate Urban Heat Islands (UHIs; Oke 1973, 1987) As a result, there is a continued demand to study the meteorological impacts, among other topics, caused by these urban-induced environmental feedbacks (Melillo et al. 2014).

Studies investigating the effects of urban environments on precipitation modification have been occurring for nearly a century (see reviews by Lowry 1998; Shepherd 2005; Souch and Grimmond 2006; Shepherd 2013; Mitra and Shepherd 2016). One notable observational study, as summarized in Changnon Jr. (1968, 1980), suggested that Chicago is increasing both rainfall and hail hazards in La Porte, Indiana. This

study led to a seminal coordinated field program, the Metropolitan Meteorological Experiment (METROMEX), which explored inadvertent modification of precipitation patterns by the city of St. Louis, MO (Changnon Jr. et al. 1971). Results from this campaign revealed a 4%–25% increase in rainfall downwind, around 50 km to 75 km from the city, during the warm season (Changnon Jr. 1979; Changnon Jr. et al. 1991). METROMEX not only validated prior urban thunderstorm studies, it also served as the impetus for continued urban meteorological modification studies across the United States (e.g., Westcott 1995; Bornstein and Lin 2000; Shepherd et al. 2002; Dixon and Mote 2003; Burian and Shepherd 2005; Mote et al. 2007; Ntelekos et al. 2007; Rose et al. 2008; Hand and Shepherd 2009; Niyogi et al. 2011; Ashley et al. 2012; Smith et al. 2012b; Haberlie et al. 2015) and around the world (e.g., Jauregui and Romales 1996; Tayanc and Toros 1997; Robaa 2003; Kishtawal et al. 2010; Mitra et al. 2012; Zhang et al. 2014; Dou et al. 2015).

Contemporary observational studies use a variety of tools and datasets to document inadvertent precipitation modification by urban areas. Many past approaches have relied on the measurement of precipitation at a single point or assembly of observational points into a contour map (Huff and Changnon Jr. 1972; Jauregui and Romales 1996; Bornstein and Lin 2000; Burian and Shepherd 2005; Diem and Mote 2005). Using 19 rain gauges around the Houston, TX metro area, Burian and Shepherd (2005) found an increase in rainfall totals ranging from 59% within the urban footprint to 30% downwind of Houston compared to an upwind control area between noon and midnight. Diem and Mote (2005) found an increase in the number of summertime heavy-precipitation days at a station 30 km downwind of Atlanta, GA, which they postulate is due to increased urbanization of the metropolitan area. While gauge networks serve as a direct measurement of the amount of rainfall, thunderstorms and their associated precipitation magnitudes can be highly variable, causing an underestimate in precipitation totals with a sparse observation network (Smith et al. 1994; Souch and

Grimmond 2006).

Hand and Shepherd (2009) compared satellite-based radar from the Tropical Rainfall Measuring Mission (TRMM) Multisatellite Precipitation Analysis (TMPA) to rain gauges around Oklahoma City, OK. Not only did they observe a strong relationship between prevailing wind and a rainfall enhancement in a 25 km area NE of OKC; they also found that the satellite-based precipitation estimates were relatively accurate when compared to gauge networks. The global ubiquity of satellite data allows for the use of TRMM/TMPA data to explore the positive correlation between rapid urbanization and precipitation enhancement in India (Kishtawal et al. 2010; Mitra et al. 2012) and a measured decline in the number of precipitation days in Beijing (Zhang et al. 2014). However, due to its non-geostationary orbit, the TMPA system was unable to do sub-hourly analyses, limiting its ability to collect precipitation information at an event specific timescale (Shepherd and Burian 2003).

The integration of lightning detection networks partially addresses these temporal limitations by allowing for the identification of predominantly cloud-to-ground (CG) strikes across widespread areas at sub-minute resolution (see review by Stallins and Rose 2008). Urban aerosols can modify the microphysical processes associated the strength and duration of updrafts (van den Heever and Cotton 2007; Rosenfeld et al. 2008) and updraft strength is strongly correlated to total lightning production (Deierling and Petersen 2008). In the United States, Steiger et al. (2002) and Stallins et al. (2006) found enhanced CG lightning densities over and downwind of Houston, TX and Atlanta, GA respectively. Yet, CG lightning occurrence can be discontinuous in time and space, leading to challenges in spatial association with specific thunderstorms (Boussaton et al. 2007; Stallins and Rose 2008).

Ground-based radar provides a spatially continuous view of precipitation echoes and is a valuable tool to examine the urban feedbacks on thunderstorms (e.g. Matyas 2010). Atkinson (1971) used radar to track echo position and intensity of a single

thunderstorm and observed rapid cloud growth followed by a local precipitation maximum within the city limits of London, England. Bornstein and LeRoy (1990) used radar reflectivity to show echo maxima over New York City, NY associated with urban-initiated thunderstorms and highlight a propensity for storms that initiated upwind of the city to bifurcate after interacting with the city. In recent years, Doppler radar data, particularly from the Weather Service Radar-1988 Doppler (WSR-88D) network, have been used to develop climatologies of urban-induced thunderstorm initiation and intensity tracking (Mote et al. 2007; Niyogi et al. 2011; Ashley et al. 2012; Haberlie et al. 2015). Leveraging hourly precipitation data from the WSR-88D site co-located with Atlanta, GA, Mote et al. (2007) observed precipitation enhancement downwind of the city that is most evident in the early evening hours through the summer months of 2002-2006. Niyogi et al. (2011) evaluated 91 unique summertime thunderstorm events around Indianapolis, IN and found that 60% of storms interacting with the city changed structure (i.e., shape and size) with these changes occurring more frequently in daytime over nighttime convection. Ashley et al. (2012) evaluated 10 summers of 5 min. composite reflectivity data alongside CG lightning data to examine the influence of five urban and two rural areas in the Southeast United States have on thunderstorm activity occurring on synoptically benign days. Their observations suggest that major cities have a positive correlation to thunderstorm frequency and intensity while mid-size cities provide a more muted signal that is difficult to decouple from other local or regions physiographical processes. Furthermore, lightning was much more common around the urban environments compared to the rural areas. Haberlie et al. (2015) used an extended version of the composite reflectivity dataset from Bentley et al. (2010) and Ashley et al. (2012) to examine how the urban environment around Atlanta, GA affects the rate of isolated convective initiation (ICI) events. After segmenting to summer months and synoptically benign days, they found that ICI occurrence was most pronounced in the late afternoon/early evening hours (2100 UTC – 0300 UTC), partic-

ularly during weekdays compared to a rural control region west of the city. In addition, ICI occurrence tended to occur over and downwind of the city area, particularly for 700 hPa flows with a northerly component.

In general, most investigations using radar to understand urban-induced feedbacks have focused on summertime months when urban and rural temperature differences are the highest, however, these temperature differences exist year-round (Gallo and Owen 1999). The few multi-radar WSR-88D studies have focused on the southeastern United States (Bentley et al. 2010; Ashley et al. 2012; Haberlie et al. 2015) while observational studies outside this region have focused on single-radar analyses of reflectivity (Bornstein and LeRoy 1990; Niyogi et al. 2011) or rainfall (Smith et al. 2012b) for one metropolitan area. Huff and Changnon Jr. (1973) found inadvertent precipitation modification around six cities, three of which (Cleveland, Chicago, St. Louis) were located in the Central United States and displaced from the eastern seaboard where a majority of observational WSR-88D studies have occurred. Furthermore, several studies suggest that thunderstorm modification can lead to taller convective clouds, allowing for greater amounts of supercooled water to enter the -10°C to -20°C isothermal region, enhancing the potential for lightning and hail hazards (Shepherd 2005; van den Heever and Cotton 2007). Yet, the ability to observe and calculate the vertically-integrated signal of a radar echo is underexplored to date.

This study fills in some of the knowledge gaps above by first introducing a strategy to generate a multiple-radar multiple-sensor (MRMS; Smith et al. 2016) 3D reflectivity cube as well as 2D vertically-integrated fields for precipitation volume and hail growth. Second, this workflow is used to create a five-year (2010–2014), all season, radar dataset to quantify storm-based thunderstorm modification effects around four cities of variable size in the Central United States: Dallas/Fort-Worth, TX (DFW), Oklahoma City, OK (OKC), Omaha, NE (OAX), and Minneapolis/St. Paul, MN (MSP). This region is not only underexplored in contemporary studies, but represents an area

sharing a common ecological setting while being relatively sheltered from major physiographic factors (i.e., oceans and mountain ranges) that can influence thunderstorm activity and be difficult to decouple from urban influences (Ashley et al. 2012; Walker et al. 2015).

In addition to generating the MRMS framework, this study uses an automated thunderstorm identification and tracking system to identify thunderstorm areas (hereafter referred to as objects) and quantify several radar-based attributes over time. Using these event-specific objects, this study will expand upon past observational hypotheses in pursuit of answers to the following questions:

1. What role does city size play in the modification of a thunderstorm echo, expressed in terms of composite reflectivity, downwind of an urban area?

2. How are vertically-derived products, expressed using calculations of Vertically Integrated Liquid (VIL; Greene and Clark 1972), and Maximum Expected Size of Hail (MESH; Witt et al. 1998b) modified in proximity to an urban area?

One of the primary benefits to use a multi-radar blending approach over a single-radar analysis is because many WSR-88D radars are near urban areas and can underestimate intensity when a thunderstorm is nearby. On 24 May 2012, a convective cell passed directly over the KOAX WSR-88D site near OAX (Fig. 3.1). Tracking intensity by the 55 dBZ echo area shows a rapid decline as the storm passes near and over the radar site before increasing again. MRMS, due to its ability to blend information from multiple radars, does not show this rapid decline and maintains better continuity on overall storm intensity over time. This improvement is quite important considering a WSR-88D site exists within the urban footprint for two of the study cities (DFW and MSP), within 7 km from OAX, and 10 km from OKC.

## 3.2 Study Domain

The study domain expands from 49.6°N 102.5°W in the northwest corner down to 28.0°N 84.9°W in the southeast corner and encompasses a region commonly referred to as the United States Great Plains (Rossum and Lavin 2000) (Fig. 3.2). Four cities with different spatial urban footprints (Table 3.1) were chosen for analysis with urban size ranging from 702.4 $km^2$ in OAX to 4,607.9 $km^2$ in DFW. According to the 2011 version of the National Land Cover Database (NLCD; Homer et al. 2015), four categories – shrub/scrub (52), grassland (71), pasture/hay (81), and cultivated crops (82) – constitute the majority of the land cover within 25 km of each city. These categories constitute 70.4% of the land cover surrounding DFW, 62.6% around MSP, 69.6% around OKC, and 83.7% around OAX. As described in Walker et al. (2015), mean annual precipitation rates decline westward towards the Rockies and along a northwest-southeast gradient across the Great Plains. As a result, the northern two cities see around a 150 mm decline in average precipitation compared to the OKC and DFW domains. From 2010 through 2014, the SPC severe thunderstorm events database (Schaefer and Edwards 1999) shows at least 400 reports of significant severe hazards (i.e., hail $\geq$ 2 in., wind gusts $\geq$ 65 kts, or tornado) occurring within 200 km of each city. Thunderstorms occur more frequently in the southern latitudes and serves as a primary driver for the increased number of severe reports in the southern two cities (e.g., Brooks et al. 2003; Smith et al. 2012a; Cintineo et al. 2012).

## 3.3 Data

### 3.3.1 Radar Data

The WSR–88D Next-Generation Radar (NEXRAD) network, consisting of 160 S-band radars across the United States and outlying territories, was implemented as part

of the National Oceanic and Atmospheric Administration's (NOAA) National Weather Service (NWS) modernization and restructuring initiative in the 1990's with the goal of improving hazardous weather awareness and warning performance (Crum and Alberty 1993; Polger et al. 1994). Since its initial inception, numerous improvements in data quality control and resolution have been operationally implemented (Crum et al. 1998). This five-year study period represents one such era of improvement with the availability of "super-resolution" products for all NEXRAD radars of interest (Torres and Curtis 2007). Super-resolution enhances the quality of base radar variables by reducing the effective scanning beamwidth from 1.38° to 1.02°. This allows for vortex and other storm-scale features to be resolved at longer ranges from any single WSR-88D (Brown et al. 2002, 2005).

A Level-II archive of these data, containing at least three Doppler radar moments (i.e., reflectivity, velocity, and spectrum width) along with system status and interpretation information (Crum et al. 1993), are available for download by the National Centers for Environmental Information (NCEI). All available Level-II data between 1 January 2010 and 31 December 2014 for each of the 19 WSR-88D sites, amounting to 7,107,005 volume scans, were utilized in this study.

### 3.3.2 Lightning Data

The NLDN is a system of ground-based lightning sensors that detects electromagnetic radiation emitted by CG flashes and strokes as well as a small percentage of in-cloud pulses across the continental United States (CONUS) (Cummins et al. 1998b). Major network upgrades in 2003 provide uniform continental coverage with a high detection efficiency (~95%) for CG flashes and geographically variable detection efficiency for cloud flashes (16-40%, Cummins and Murphy 2009). Using the National Severe Storms Laboratory (NSSL) NLDN archive, 1,234,625 one-minute time-steps

were downloaded to identify the 39,664,548 CGs that occurred in the study domain.

### 3.3.3 Environmental Data

The Rapid Update Cycle (RUC; Benjamin et al. 2004) was the first operational Numerical Weather Prediction system to assimilate multi-sensor observations and provide both hourly analysis (i.e., current conditions) and short-range forecast grids to enhance situational awareness on near-term hazardous weather. In 2012, the improvements to the RUC assimilation framework were implemented and the system was re-branded as Rapid Refresh (RAP; Benjamin et al. 2016). This study uses the hourly analysis fields produced by the RUC and RAP (hereafter referred to as model) to improve the quality control of radar velocity data (e.g., Miller et al. 2013), create blended radar and environmental fields (e.g., Smith et al. 2016), and assist in the classification of thunderstorm convective modes (e.g., Hobson et al. 2012). Five years of the highest resolution model analysis data (either 20 km or 13 km), amounting to 43,613 hours, were downloaded from the NCEI National Model Archive and Distribution System. If an hourly analysis grid is missing, another grid up to three hours old was used to fill in the missing values, otherwise, that hour was excluded from the dataset. This was mainly an issue between 1 May 2012 and 8 May 2012 during the initial operational transition from RUC to RAP.

### 3.3.4 Urban Boundaries

There is a non-standardized process to define an urban area in the past literature. Urban areas have been defined by population (Kishtawal et al. 2010), uniform buffered areas extending from the city center (Hand and Shepherd 2009; Haberlie et al. 2015), the U.S. Census Bureau (Mote et al. 2007; Walker et al. 2015), and Landsat-classified land cover datasets (Ashley et al. 2012). In this study, two methods of urban identification

were used to create an urban boundary. The first method used the urban boundary coordinates from the United States Census Bureau (2010). The definition of an urban area consists of a spatially dense region of urban land use that contains greater than 50,000 people. The second method involved manually contouring an urban boundary from the urban/built-up categories (21-24) from the 2011 NLCD Database (Homer et al. 2015). Both methods provided very similar latitudinal and longitudinal distances for the city ($<$ 5 km) and fundamentally did not alter the overall results of the study.

## 3.4 Methods

### 3.4.1 Product Generation & Thunderstorm Tracking

All radar, model, and lightning outputs were processed using the Warning Decision Support System – Integrated Information (WDSS-II; Lakshmanan et al. 2007b) software platform. The processing steps (flowchart in Fig. 3.3) for each of the products are described below.

#### 3.4.1.1 CG Lightning Grids

The CG strike location and time information from the NLDN dataset were binned into 1 min. time-steps and gridded onto a 0.01° x 0.01° Cartesian grid (w2ltgcount). To account for the increased detection efficiency of lower amplitude events that may not actually be CGs (Cummins and Murphy 2009), all CGs with a peak amplitude less than 5 kA were excluded from the gridding process.

#### 3.4.1.2 Model Analysis Grids

Hourly model analysis data were ingested to re-project the basic meteorological fields (i.e., temperature, height, pressure, wind) at all vertical levels onto a common Cartesian

grid. These fields served as inputs into the near-storm environment (nse) algorithm to generate 2D convective instability fields, isothermal heights, and sounding profile products. These output fields were used to quality control the single-radar data (sub-section 3.4.1.3) and generate several multi-radar and tracking products (sub-sections 3.4.1.4 and 3.4.1.5).

#### 3.4.1.3 Single-Radar Product Generation & Quality Control

Level-II radar data at all 19 WSR-88D sites were ingested to generate the base products of reflectivity, aliased velocity, and spectrum width (ldm2netcdf). Previous studies have mitigated the impact of non-meteorological targets (e.g., birds/insects, ground clutter, electronic interference) and blockage by using a higher reflectivity minimum of 40 dBZ (Ashley et al. 2012; Haberlie et al. 2015). For this analysis, a neural network framework of Lakshmanan et al. (2007a) was used to identify and remove these sources of error while retaining lower reflectivity precipitation returns in a new ReflectivityQC field (w2qcnn). ReflectivityQC was used in conjunction with the NWS operational dealiasing algorithm from Jing and Wiener (1993) to mitigate measurement errors in the true radial projection of the environmental wind and generate a quality-controlled velocity field (dealias2d). Both of these fields were inputs in the generation of single and vertically integrated azimuthal shear (w2circ; Smith and Elmore 1994).

#### 3.4.1.4 Multi-Radar Grid Generation

The ReflectivityQC and vertically-derived azimuthal shear from the individual radar sites along with the model data were inputs into an intelligent agent framework of Lakshmanan et al. (2006) to generate 3D Cartesian grids for reflectivity (azimuthal shear) of at 0.01°-by-0.01° (0.005°-by-0.005°) spatial resolution, one min. temporal resolution, at 33 vertical levels (w2merger). These levels have 250 m vertical spacing

from 0.5 km AGL to 3 km AGL, 500 m vertical spacing from 3 km AGL to 9 km AGL, and 1 km vertical spacing from 9 km AGL to 20 km AGL. To calculate VIL at a grid cell, the 3D reflectivity field is vertically-interpolated using the Greene and Clark (1972) method. To exclude contamination from ice, interpolated reflectivity values exceeding 56 dBZ were capped at 56 dBZ. MESH was calculated using the method of Witt et al. (1998b) and uses both a vertical integration of reflectivity along with the 0°C and -20°C isothermal heights to estimate the maximum diameter of a hailstone.

#### 3.4.1.5 Automated Thunderstorm Tracking

The w2segmotionll algorithm in WDSS-II combines a watershed segmentation model (Lakshmanan et al. 2009) with K-means clustering (Bishop 2006) to identify thunderstorm objects based on a single observational variable (e.g., radar reflectivity) and calculate summary statistics of other MRMS gridded attributes (e.g., maximum MESH, lightning count, etc.) throughout the tracking lifetime. This algorithm was used to identify and track thunderstorm attributes in two stages. The first stage follows the methods outlined in Hobson et al. (2012) by identifying and tracking objects based on a minimum composite reflectivity of 20 dBZ (i.e., the maximum reflectivity measured in the vertical column). In addition to thunderstorm object creation, this method also classifies the convective mode of each thunderstorm object as either a supercell (Browning 1962) or non-supercell. This classification information and the MRMS gridded outputs were tracked a second time using the reflectivity at the -10°C isothermal level with a minimum reflectivity threshold of 20 dBZ as this field is less susceptible to dramatic change across time-steps that can prematurely break thunderstorm tracks (Herzog et al. 2014).

Many automated tracking systems make decisions based on the current information available. Quality control or hardware failures from a radar site can temporarily alter

the magnitude and extent of a thunderstorm, causing a tracking algorithm to re-classify it as a new object and prematurely break an existing thunderstorm track. To assess the integrity of the thunderstorm tracks, a post-event track attachment strategy similar to Lakshmanan et al. (2015) was used to validate that the end of tracking corresponds to the end of the storm lifecycle. This was accomplished by geometrically simplifying the thunderstorm object boundaries using a convex hull (Devadoss and O'Rourke 2011), buffering this hull (i.e., having its perimeter spatially expanded outward) by a radius of 5 km, and projecting this new object forward along the tracking propagation angle for an additional radar volume update interval (~5 min.). If a second storm object begins within the projected buffer, this second object track was appended to the end of the first object track. If more than one additional object appears within this post-tracking search domain, a selection was prioritized based on the (1) maximum storm lifetime, (2) closest start time, and (3) maximum spatial storm overlap with the search buffer.

### 3.4.2 Thunderstorm Case Selection

The spatial and attribute information from the thunderstorm objects were evaluated using two distinct methods. The first method examines how the maximum values of composite reflectivity, MESH, and VIL change using independent temporal samples of thunderstorms upwind and downwind of each city. The second method examines the spatial distribution of the three radar fields within these two regions. In order to provide a consistent dataset across the two methods, criteria to constrain the number of thunderstorm objects were applied. First, a thunderstorm object had to be tracked for at least 30 min. to remove tracks that could be classified as noise or failed thunderstorms (Haberlie et al. 2015). Second, the object centroid (i.e., the geographic center of the object area) had to pass within the urban boundary. This removed many cases where only a small fraction of larger, more organized storm system generally displaced from

the city from being included in the dataset. Finally, the storm had to achieve a 35 dBZ composite reflectivity value and 1 CG strike anywhere in its object area for at least one time-step. This threshold eliminated non-convective snow systems and stationary sources of noise that passed through radar quality control.

As noted in previous studies (e.g., Huff and Changnon Jr. 1972; Lowry 1998; Dixon and Mote 2003), examining thunderstorm days without any segmentation by season, synoptic regime, or diurnal limits could mask the effect urban areas have on thunderstorms. In addition to examining the full set of thunderstorm objects, a case subset was created using seasonal, diurnal, and synoptic conditions with an elevated likelihood of influence from urban effects. This "urban favorable" (hereafter referred to as UF) subset consisted of thunderstorm tracks that (1) occurred in the meteorological summer months (June–August) where the greatest urban-rural temperature differences are likely to occur (Gallo and Owen 1999); (2) initiated around the urban area in the mid-afternoon/evening hours, identified as the central half of a convective day (18 UTC – 06 UTC), to capitalize on this temperature difference and encase the time period where enhanced convective activity has been shown to occur (e.g., Mote et al. 2007; Haberlie et al. 2015); (3) occurred on days classified with a moist tropical (MT) airmass via the Spatial Synoptic Classification dataset of Sheridan (2002) as these days have been shown to yield greater UHI-induced precipitation events than dry airmass days (Dixon and Mote 2003; Hand and Shepherd 2009; Ashley et al. 2012); and (4) with $< 10\%$ of the storm track classified as a supercell per the Hobson et al. (2012) method as a second indicator of days with minimal vertical shear and meteorological forcing.

#### 3.4.2.1 Storm-Based Maximum Sampling

Due to the 1 min. sampling interval on these thunderstorm objects, there is a degree of dependence between successive observations. Herzog et al. (2014) found the opti-

mal de-correlation timescale is at least 9 min. when sampling individual thunderstorm attributes (i.e., maximum reflectivity). At every time-step, each thunderstorm object was categorized as either upwind (A), over the city (B), or downwind (C). For all objects meeting the above criteria, the maximum composite reflectivity, VIL, and MESH were sampled beginning at the 5 min. time-step and re-sampled every 10 min. afterwards. For instance, a storm lifetime of 30 min. would be sampled at 5, 15, and 25 min. respectively. This initial 5 min. time step (i.e., the average radar volume update time) was chosen to mitigate potentially sampling the initial or late stages of the thunderstorm. Additionally, previous studies have shown that city size and orientation can vary the magnitude of precipitation modification (Huff and Changnon Jr. 1973; Shepherd and Burian 2003; Schmid and Niyogi 2013). To account for this, a city-dependent buffer amounting to the larger of either the latitudinal or longitudinal distance was used to constrain the maximum distance a thunderstorm observation could be sampled from each city. The amounted to 127 km from DFW, 85 km from MSP, 56 km from OKC, and 47 km from OAX. Other permutations amounting to 50% and 150% of this initial distance were also examined but did little to change the overall narrative. Comparisons in the distributions of upwind and downwind observations were evaluated using a two-sample Kolmogorov-Smirnov test (Wilks 2006).

#### 3.4.2.2 Spatial Distribution of Radar and Lightning Data

In order to examine the spatial augmentation of thunderstorms, an upwind and downwind region needs to be defined. In the absence of the tracking individual objects, several past studies have used the 700 hPa prevailing flow from a local NWS office (Hand and Shepherd 2009; Haberlie et al. 2015) In this study, the upwind and downwind regions were defined on a case-by-case basis by using the direction of motion from the tracked thunderstorm object (Fig. 3.4). Once defined, the maximum value

of composite reflectivity, VIL, and MESH was spatially accumulated over the object lifetime. Hand and Shepherd (2009) noted the potential for variable magnitudes of precipitation modification to occur depending on the direction of the prevailing wind. Complex shapes and appendages of urban sprawl are associated with each city; these result in an inconsistent start (end) to the upwind (downwind) region. To standardize these zones, each city was geometrically simplified using a convex hull operation and the upwind and downwind regions were started an additional 10 km away from this convex boundary. From 10 km onward, radar values were binned in 1 km intervals and the amount of area covered in each bin was calculated. From this information, the areal mean value of each parameter was calculated and tested for significance using a non-parametric two-sample permutation test of the mean (Wilks 2006).

## 3.5 Results

### 3.5.1 Dataset Overview

The number of storms analyzed was dependent on city area with 718 storms around DFW, 644 around MSP, 460 around OKC, and 391 around OAX (Fig. 3.5). At the northern latitudes, MSP and OAX had the most thunderstorms occurring during the meteorological summer accounting for 56.5% and 45.5% of all observations. DFW and OKC had the most thunderstorms during meteorological spring (March – May) with 40.9% and 37.8% of the respective storms. Summertime was the second most active with 22.3% and 33.5% respectively. Southern latitudes also had more storm opportunities in the fall and winter months accounting for 36.7% of storms in DFW, 28.7% in OKC, 26.1% in OAX, and 11% in MSP.

Grouping thunderstorm occurrence relative to the city reveals that all cities had the highest number of thunderstorm objects occurring upwind and decaying below

the spatiotemporal thresholds for tracking over the city (AB). Storm object centroids initially tracking over the city and moving downwind (BC) account for the second most number of samples for all cities. Finally, the smallest percentage of storms were those that formed upwind of the city and were tracked through and downwind of the city (ABC). These tracks accounted for 10% of DFW storms, 18% of MSP storms, 30% of OKC storms, and 26% of OAX storms, inversely related to city size. The primary storm motion based on the centroid position for most events was from southwest to northeast in all cities, comparable to observations by Changnon Jr. and Huff (1961).

The number of storms occurring within the UF subset accounts for 5.7% of DFW storms, 14.5% of MSP storms, 6.1% of OKC storms, and 6.9% of OAX storms. In this UF subset, a higher percentage of storms formed over the city than upwind for DFW and MSP. Around OKC, there were 12 AB storms and 12 BC storms. OAX was the only city to have more AB storms (11) than BC storms (9). Thunderstorm direction on these synoptically weak days is not as uniform compared to tracks from the full climatology. 41% of DFW storms propagated from the north or northwest, MSP and OKC observed 40% and 46% of storms propagating from the west, and 66% of OAX storms moved from the northwest or southwest (Fig. 3.5).

### 3.5.2 Object–Based Maximum Sampling

Drawing independent samples of maximum composite reflectivity (hereafter referred to as reflectivity; Fig. 3.6a), VIL (Fig. 3.6b), and MESH (Fig. 3.6c) for all days (solid lines) and the UF subset (dashed lines) reveals similar results across all cities in the full climatology but variable results in the UF subset. In the full climatology, there were more independent reflectivity and VIL samples from storms downwind of DFW and MSP and upwind of OKC and OAX (see number of samples, N, in Fig. 3.6). Additionally, all four cities had a lower number of MESH samples in the downwind region.

In the UF subset, there were 35% more MESH observations downwind of DFW and one additional reflectivity/VIL observation downwind of OKC. The remaining cities and radar variables showed similar sampling trends as in the full climatology.

For DFW, all three distributions of reflectivity, VIL, and MESH from the full climatology and UF subset are significantly different ($p < 0.05$, left column of Fig. 3.6) between the upwind and downwind distributions. In the full climatology, there was a higher overall percentage and frequency of stronger storms upwind revealed through the number of reflectivity samples > 40 dBZ, VIL > 2 kgm$^{-2}$, and MESH $>$ 1 mm. In the UF subset, the downwind region had 106% more reflectivity/VIL samples and 36% more in MESH samples than the upwind region. Additionally, 70% of downwind (66) and 100% of upwind (46) samples were $>$ 50 dBZ within the UF subset. A similar pattern emerges within the UF subset using VIL with a lower overall percentage but higher frequency of downwind samples $>$ 23 kgm$^{-2}$ and $>$ 45 kgm$^{-2}$. The MESH distributions, while still significantly different, were much closer together compared to the other radar variables. Five downwind samples exceeded the criteria for severe hail (25 mm or 1 in.) compared to one upwind sample.

Around MSP (second column – Fig. 3.6), both the full climatology and UF subset had a greater number of downwind composite reflectivity/VIL samples and fewer MESH storm samples. In the full climatology, there were fewer reflectivity observations $>$ 40 dBZ, VIL samples $>$ 2 kgm$^{-2}$, and MESH observations $>$ 1 mm occurring in the downwind region. However, downwind reflectivity samples in the UF subset had a wider spread of values with 71% of samples $>$ 50 dBZ compared to 83% of upwind samples. When the sample area is constrained to 50% of the city diameter (42 km) instead of 100% (83 km), the differences between the two distributions are no longer statistically significant. Contrary to observations in the full climatology, VIL and MESH samples from the UF subset were generally higher in the downwind region with more samples of VIL $>$ 8 kgm$^{-2}$ and MESH $>$ 2 mm. Six downwind samples

of MESH in the UF subset met the severe hail criteria while no observations of this magnitude were observed upwind of MSP.

The downwind region of OKC had approximately 7% fewer reflectivity/VIL samples and 21% fewer MESH samples than the upwind area in the full climatology. In the UF subset, the downwind region had 2% more reflectivity/VIL samples 53% fewer MESH samples compared to the upwind region. Unlike the larger two cities, OKC shows a more consistent trend across both datasets. The distributions are significantly different from each other with a greater percentage and frequency of stronger samples of all parameters in the upwind region. In the full climatology, around 80% (70%) of reflectivity samples were $>$ 50 dBZ, 40% (23%) of VIL samples were $>$ 20 kgm$^{-2}$, and 43% (31%) of MESH samples were $>$ 10 mm in the upwind (downwind) region. The difference between these two distributions is more pronounced in the UF subset. 60% (10%) of upwind (downwind) VIL samples were above 20 kgm$^{-2}$. Similar percentages were also observed for MESH $>$ 10 mm.

OAX, due to its size, has the lowest number of overall samples compared to other cities in this study and a higher number of upwind samples in both the full climatology and UF subset. In the full climatology, the overall percentage of max reflectivity values in the upwind and downwind region converges between 55 dBZ to 60 dBZ with 186 (142) upwind (downwind) samples $>$ 60 dBZ. A similar pattern emerges in the full VIL dataset between 15 and 25 kgm$^{-2}$ with 189 (174) samples from the upwind (downwind) $>$ 25 kgm$^{-2}$ threshold. The differences between the upwind and downwind regions for all radar parameters for the UF subset and MESH in the full climatology are not statistically significant around OAX.

### 3.5.3 Storm–Based Gridded Climatology

Analyses incorporating the gridded object area and accumulating the composite reflectivity (Fig. 3.7), VIL (Fig. 3.8), and MESH (Fig. 3.9) across variable upwind and downwind distances ranging from 50% – 150% of the maximum city diameter reveal common trends across all parameters in both datasets around DFW and MSP, and some variable trends around OKC and OAX. Four ways to summarize these data within each range interval upwind and downwind are shown in Figs. 3.7–3.9 and include: (a) the total number of thunderstorm objects at each 1 km bin; (b) the areal sum of the radar parameter; (c) the overall area covered by a meteorological echo; and (d) the areal mean value, which is the value in (b) divided by the value in (c) to give the mean value experienced at any given 1 $km^2$ grid cell.

DFW experiences roughly an equal number of thunderstorm objects in the full climatology from 10 km to 64 km (i.e., 50% city diameter) (Fig. 3.7a), yet the downwind region sees a 9% increase in total reflectivity (Fig. 3.7b) and a 10% increase in areal coverage (Fig. 3.7c). A larger areal echo coverage occurring in the downwind region coupled with the lack of an equivalent increase in total reflectivity results in a lower areal mean reflectivity in this region that decreases at further ranges from the city (Fig. 3.7d). MSP experiences 10% more thunderstorm objects out to 43 km (50% city diameter) and 15% more thunderstorm objects out to 128 km (150% city diameter). Like DFW however, the areal mean reflectivity is lower in the downwind region (~40 dBZ/$km^2$) at all ranges compared to the upwind region (~42 dBZ/$km^2$)(Fig. 3.7d). The difference in the thunderstorm occurrence in the downwind region around OKC and OAX ranges from -3% to 3% at various ranges from the city and yields a lower overall areal mean reflectivity in the downwind region for both of these cities as well.

During UF time windows (Fig. 3.7 – right column), there are up to 51% and 33% more thunderstorm observations downwind of DFW and MSP respectively. This re-

sults in around a 153% (132%) and 73% (68%) increase in cumulative reflectivity (areal coverage) in these downwind regions and provides a 3 dBZ/km$^2$ and 1 dBZ/km$^2$ increase in downwind areal mean reflectivity around these two cities. OKC showed a 2% decline in the number of downwind storms out to 28 km (50% city diameter), however, the cumulative reflectivity was around 0.3% higher and covered an area 1.7% smaller than the upwind region, resulting in a statistically significant areal mean of 34.5 dBZ/km$^2$ in the downwind region compared to a 33.8 dBZ/km$^2$ mean in the upwind region. At 42 km (75% city diameter) and beyond, there are a higher number of thunderstorm objects in the downwind region, but the upwind region experiences a higher cumulative reflectivity over a larger area that results in a higher areal mean reflectivity at these further range windows. This means that the upwind region encompassing ranges greater than 42 km away from OKC experiences larger, stronger storms on average than the downwind area of equal distance, even in the UF subset. At all range intervals downwind of OAX in the UF subset, there were fewer thunderstorm observations in the downwind region, resulting in 9% to 19% decline in cumulative reflectivity over a 14% to 20% smaller area. From 10 – 28 km (50% city diameter), the percentage decline in cumulative reflectivity was slightly lower than the percentage decline in affected area, resulting in a marginally higher mean areal reflectivity in the upwind region (~0.1 dBZ). At subsequent ranges from OAX, there was a higher areal mean reflectivity in the downwind region.

A VIL value exists at every reflectivity pixel, resulting in an equal ratio of upwind and downwind observations that were summarized for reflectivity (Fig. 3.8 – left column). In the full thunderstorm climatology, cumulative VIL downwind of DFW is around 3% to 5% higher and occurs over a 10% to 21% larger area. This results in a lower areal mean VIL in the downwind region at all ranges. Around MSP, not only is there a lower cumulative VIL in the downwind region, the VIL area is around 16% to 24% larger than the VIL area in the upwind region. This results in a smaller areal mean

VIL that is at least 1 $kgm^{-2}/km^2$ lower in the downwind region. OKC experienced the same trend as MSP at ranges beyond 42 km with a 23% to 29% lower areal mean VIL in the downwind region. OAX was the only area to have a higher areal mean VIL in the downwind region within the full climatology resulting from a 7% to 9% increase in cumulative VIL over only a 2% to 3% increase in area.

In the UF subset (Fig. 3.8 – right column), similar patterns in VIL were seen around DFW and MSP as were identified with reflectivity. There was up to a 239% (132%) and 143% (68%) increase in total VIL (area affected) in the downwind region during these periods, resulting in a higher downwind areal mean VIL at all ranges from DFW and MSP respectively. Downwind of OKC, cumulative VIL values were 41% lower out to 84 km (150% city diameter) but only encompassed an area 5.5% smaller than the upwind region. This resulted in a lower mean VIL of 2.4 $kgm^{-2}/km^2$ compared to 3.9 $kgm^{-2}/km^2$ in the upwind region. Both the number of thunderstorm objects and the total affected area were lower in the downwind region at all ranges surrounding OAX, however, cumulative VIL increased with at ranges beyond 47 km (i.e., the OAX city diameter). From 10 km out to 71 km (150% city diameter), the cumulative VIL was 26% higher in the downwind area compared to the upwind area. As a result, areal mean VIL values downwind of OAX were 18% to 46% higher in the downwind region, comparable to observations from the full climatology. All differences in mean VIL were statistically significant in both datasets.

Unlike VIL, MESH values are not calculated at every pixel, particularly if there is no reflectivity signal at temperatures $<0°C$. This constrains the sample sizes of "hail producing" thunderstorms around all four cities. In the full climatology, all four cities had a lower number of MESH samples in the downwind region (Fig. 3.9 – left column). All range intervals downwind of DFW experienced a lower cumulative MESH but saw increase in the total MESH area, yielding a lower overall areal mean MESH. Areas downwind of MSP and OKC also had a lower cumulative MESH, like DFW, but

measured a smaller area affected by MESH. This resulted in an 8% to 32% decrease in downwind areal mean MESH for both of these cities. OAX had the opposite behavior with an increase in cumulative MESH and area affected at all range intervals. This resulted in around a 1% decline in the downwind areal mean MESH at most ranges.

In the UF subset (Fig. 3.9 – right column), both DFW and MSP show an increased number of thunderstorm objects, a higher cumulative MESH, and a larger downwind area affected, similar to observations of VIL. The highest areal mean MESH values were captured within 64 km from both DFW (50% city diameter) and MSP (75% city diameter). At ranges beyond 127 km from DFW, the difference in areal mean MESH was not statistically significant and was the only occurrence of such a result. Areas downwind of OKC had fewer thunderstorm objects, resulting in a lower cumulative MESH that affected a smaller total area. This resulted in mean MESH values at least 2 mm smaller in the downwind region. Similar to OKC, areas downwind of OAX had a lower number of thunderstorm observations. However, the areal coverage of MESH in this region was much larger, covering 14% - 55% more area than the upwind region. Cumulative MESH values also tended to be higher from 47 km (100% city diameter) and beyond, but not large enough to compensate for the increases in overall areal coverage. As a result, mean MESH was lower at all downwind ranges evaluated.

## 3.6 Discussion

This study incorporates the techniques from the MRMS framework to process over 100 terabytes of radar, lightning, and near-storm environmental fields to create grids of reflectivity, MESH, and VIL at the highest spatial ($\leq$ 1 km) and temporal (one-min.) resolution. The methods employed in this study address two main assumptions used in prior initiatives using fixed observational gauges (Huff and Changnon Jr. 1972; Jauregui and Romales 1996; Diem and Mote 2005) and remote sensing systems (Shepherd

et al. 2002; Dixon and Mote 2003; Mote et al. 2007; Hand and Shepherd 2009; Bentley et al. 2010).

First, many of these studies cannot quantify the number of storms that directly interacted with a city. Mote et al. (2007) examined hourly precipitation patterns near Atlanta and observed instances where precipitation downwind of Atlanta were actually initiated in the mountains. Our criteria that the thunderstorm object centroid passes within our defined urban domain provides a spatial constant that is shared across all cases. Second, prevailing wind not identified by manual analyses (e.g., Niyogi et al. 2011) has predominantly been estimated in past studies by using 700 hPa flow from NWS radiosonde observations Hand and Shepherd (2009); Haberlie et al. (2015) or model reanalysis data (e.g., Burian and Shepherd 2005). For this study, using the one-min thunderstorm centroid track as a guide allows for an upwind and downwind region to be defined uniquely for each case. Furthermore, these upwind and downwind regions can be standardized by its relative position from the city, allowing for the calculation of bulk statistics independent of geographic location at set ranges around each city.

Nonetheless, our analyses are not free from limitations. Thunderstorms do not always follow an ordinary lifecycle (i.e., growth, maturity, decay) in isolation, and are subject to interactions such as splitting and merging (Lakshmanan et al. 2009). While these features can be documented by smaller-scale and often time-consuming manual analyses of thunderstorms (e.g., Niyogi et al. 2011), we assume these impacts are minimized in larger-scale initiatives such as this study. Our criteria that each thunderstorm object's centroid passes within our defined urban domain and be tracked for at least 30 min. were essential to ensuring some form of an urban interaction and allowing radar attributes to be independently sampled at least three times per thunderstorm. Lowering this tracking threshold to 10 min. only increases the number of total cases by 7% around all cities. Regardless, thunderstorms with shorter lifetimes or thunderstorms

that form downwind of the city as a result of the role of potential urban-induced convergent zones (e.g., Bornstein and Lin 2000) are not included in this study. These kinds of thunderstorms are underexplored in this study, but merit future attention.

Both analysis methods, particularly the spatial gridding method, revealed similar patterns of enhanced reflectivity, VIL, and MESH magnitude and extent downwind of DFW (~4600 $km^2$) and MSP (~2650 $km^2$), the two larger cities in this study and were more evident on UF days compared to the full climatology. This pattern would imply that larger cities could alter thunderstorms sooner and at a greater magnitude than smaller cities given the appropriate conditions. Additionally, a higher number of thunderstorm objects occurred over the city and propagated downwind on these days, similar to the results of Haberlie et al. (2015) around Atlanta.

Around OKC, a city 40% the size of MSP, an increase in downwind areal mean reflectivity did occur when examining an area from 10 km – 28 km, but not within progressively larger areas around the city. Areal means of MESH and VIL as well as independent samples of the maximum reflectivity, MESH, and VIL tended to be higher in the upwind region around OKC on UF days. Hand and Shepherd (2009) identify the N-NE region downwind of OKC to be the climatologically wettest region, however, this region only aligns with six of the 28 thunderstorm objects evaluated in our UF subset and limits any sort of comparison that can be made given the constraints associated with this study. Regardless, any downwind augmentation is not as prevalent as was observed around DFW and MSP. Around OAX, an even smaller city that is 26% the size of MSP, there was no statistically significant difference between the independent upwind and downwind samples of maximum reflectivity, VIL, and MESH in the UF subset. Furthermore, unlike what was observed around DFW or MSP, there was no immediate downwind enhancement in areal mean reflectivity, VIL, or MESH on UF days. This, coupled with it being the smallest city in the study, introduces some uncertainty as to how OAX can augment thunderstorms over other geographi-

cally collocated factors such as the relatively homogeneous amount of cultivated crops surrounding this urban area. Clark and Arritt (1995) found that surfaces with moist soil and vegetation cover were most conducive to convective development. Gero and Pitman (2006) observed through numerical model simulations that the replacement of agricultural land with shrubland hindered storm development upwind from Sydney, AU. Additional numerical modeling and observational studies are needed to delineate the role of homogeneous versus heterogeneous land cover on storm initiation comparable to studies of the effects of topography (e.g., Lowry 1998; Niyogi et al. 2006).

Given that DFW (~4600 $km^2$) and MSP (~2650 $km^2$) both showed a downwind enhancement in composite reflectivity, MESH, and VIL from both analysis methods on UF days compared to OKC (~1060 $km^2$) and OAX (~700 $km^2$) indicates the contributing role city size can play in precipitation modification. Schmid and Niyogi (2013) modeled the effects of city size and found that both the maximum average heat island and the amount of precipitation modification increased linearly with city radii ranging from 5 km to 20 km with fairly constant effects observed beyond this threshold. While a definitive size threshold cannot be defined here, size is only one factor contributing to magnitude of urban modification. Other contributing factors such as the regional climate (Roth 2007), the variable influence of urban-induced aerosols on precipitation timing and magnitude (Rosenfeld et al. 2008; Lebo 2014; Schmid and Niyogi 2017), and surrounding regional landscape species variability (Rabin et al. 1990) coupled with urban size/shape could provide a geographically dependent alteration to the extent of precipitation modification.

## 3.7 Conclusions

Using the MRMS framework to create and spatially track thunderstorm objects, five years of composite reflectivity, MESH, and VIL grids were examined around four

cities of varying sizes (DFW, MSP, OKC, and OAX) to examine how city size augments thunderstorms. Overall, city size seems to be a contributing factor in enhancing the coverage and magnitude of these radar variables in the downwind region, however, these effects were not as clearly observed when examining objects across all seasons and synoptic regimes. Taking independent samples of each thunderstorm object every 10 min. reveals that a greater overall percentage and frequency of thunderstorm objects had a higher composite reflectivity, MESH, and VIL occurring upwind of all four cities. Spatially accumulating these fields revealed a higher areal mean of all three parameters occurring upwind of all four cities, with the exception of VIL around OAX.

Taking a subset of thunderstorm objects matching historical seasonal, temporal, and synoptic environments shown in the past literature where urban modification is likely, reveals an increased number of thunderstorm objects forming and moving downwind of DFW and MSP, the two largest cities examined. This resulted in a higher areal mean value of composite reflectivity, MESH, and VIL at several ranges downwind of both cities compared to the upwind region. This pattern was not as uniformly observed downwind of OKC and OAX, cities roughly 40% and 26% the size of MSP, particularly in analyses of the vertically-derived fields of MESH and VIL. This could be indicative of a lack of influence of small to midsized urban areas ($\leq$~1100 km$^2$ based on our city selection) on the enhancement of radar-derived maximum values and spatial area affected downwind of these cities. The thresholds used to delineate UF environments resulted in an 84% to 94% reduction in the number of thunderstorm cases based on observations of thunderstorm initiation augmentation measured in prior studies (Diem and Mote 2005; Mote et al. 2007; Haberlie et al. 2015). The contrast between the full climatology and UF subset reveals that the percentage of storms capable of being augmented by a city due to seasonal, temporal, and synoptic influences as defined in the literature is a small fraction of the number of storms that affects cities on a yearly basis. Based on the percentage of UF storms retained from the full climatology,

MSP (14.5%) compared to DFW (5.7%), OKC (6.1%) and OAX (6.9%) has the highest potential for the urban domain to influence storm structure and intensity. However, the inconsistent nature of these precipitation modification patterns in the lens of the full climatology of all cities makes us question whether the predictability of these patterns is achievable, since instantaneous measures of other suspected modification variables (e.g., spatial aerosol loading, van den Heever and Cotton 2007; Kawecki et al. 2016) may not be readily observable.

## Acknowledgements

The authors would like to thank Gregory Dean and Kiel Ortega for their assistance in downloading the large volume of radar data for this study. We also thank Bethany Hardzinski, Paul Downes, Jonathon King, and Benjamin Herzog for their assistance with initial data collection and algorithm evaluation. We acknowledge useful discussions with Kevin Manross on the methods of this paper. We would finally like to thank the three anonymous reviewers, whose comments and philosophical questions improved the content of this manuscript. This work is funded through the NASA Interdisciplinary Science Program project NNX12AM89G as part of the grant "Storms, Forms, and Complexity of the Urban Canopy: How Land Use, Settlement Patterns, and the Shapes of Cities Influence Severe Weather."

Table 3.1: Population and land area from the 2010 United States Census (United States Census Bureau 2010), latitudinal and longitudinal length from absolute bounds of NLCD urban area, 20th century mean annual precipitation from NOAA (NOAA NCEI 2014), significant severe thunderstorm hazards inside the urban footprint and within 200 km of the urban footprint from 2010-2014 from the Storm Prediction Center database (Schaefer and Edwards 1999).

| City | Population | Land Area [km$^2$] | Latitudinal Length [km] | Longitudinal Length [km] | Mean Annual Precipitation [mm] | Significant Severe Hazards within Urban Footprint | Significant Severe Hazards within 200 km of Urban Footprint |
|---|---|---|---|---|---|---|---|
| Omaha, NE | 725,008 | 702.4 | 39.8 | 46.9 | 723 | 16 | 625 |
| Oklahoma City, OK | 861,505 | 1063.5 | 56.0 | 52.8 | 874 | 55 | 658 |
| Minneapolis/St. Paul, MN | 2,650,890 | 2646.5 | 82.9 | 85.0 | 717 | 27 | 409 |
| Dallas/Ft. Worth, TX | 5,121,892 | 4607.9 | 103.4 | 127.2 | 869 | 86 | 578 |

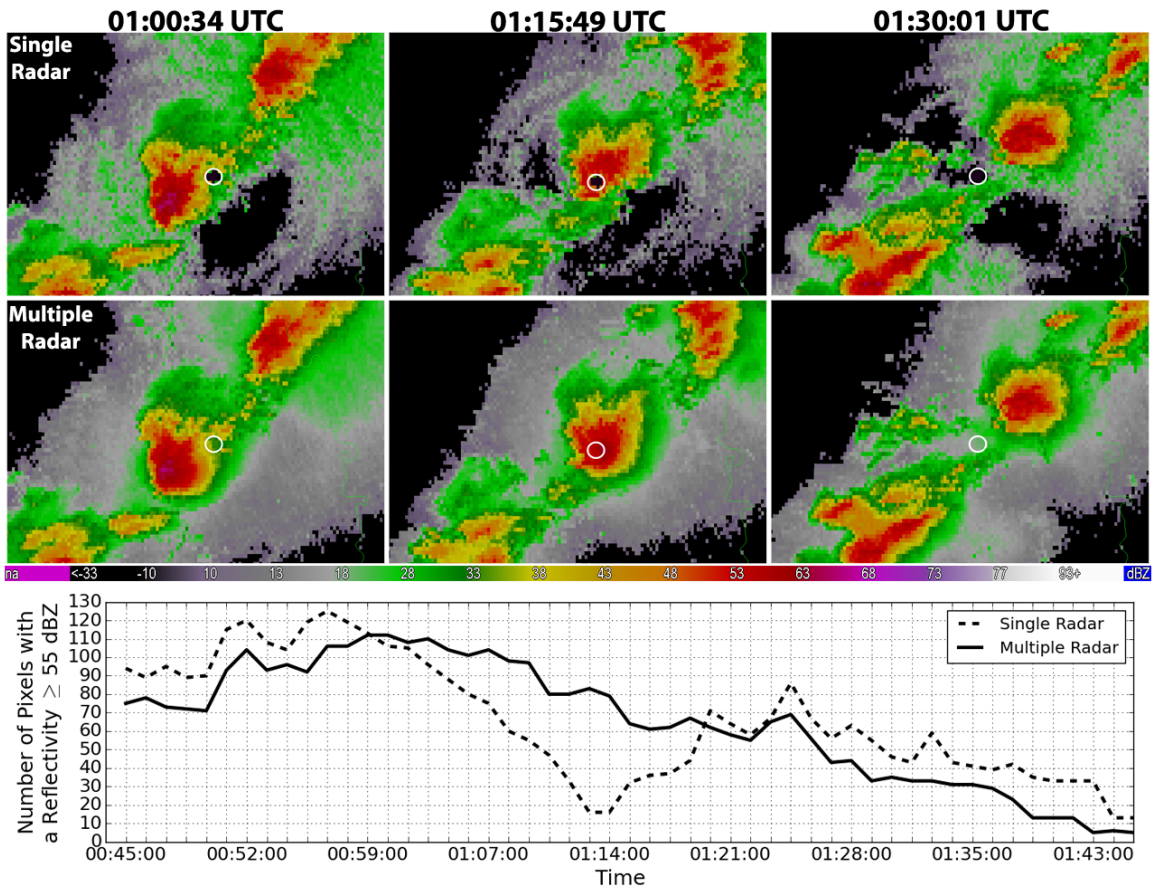


Figure 3.1: Time series of the 55 dBZ echo area of a thunderstorm passing over the KOAX WSR-88D site (white circle) on 24 May 2012 derived from a single-radar and multiple-radar analysis. In the single-radar analysis, there is an artificial decline in this echo area as the storm moves over the radar site due to sampling limitations. Leveraging data from multiple radars mitigates this issue and provides a cleaner evaluation of storm intensity.

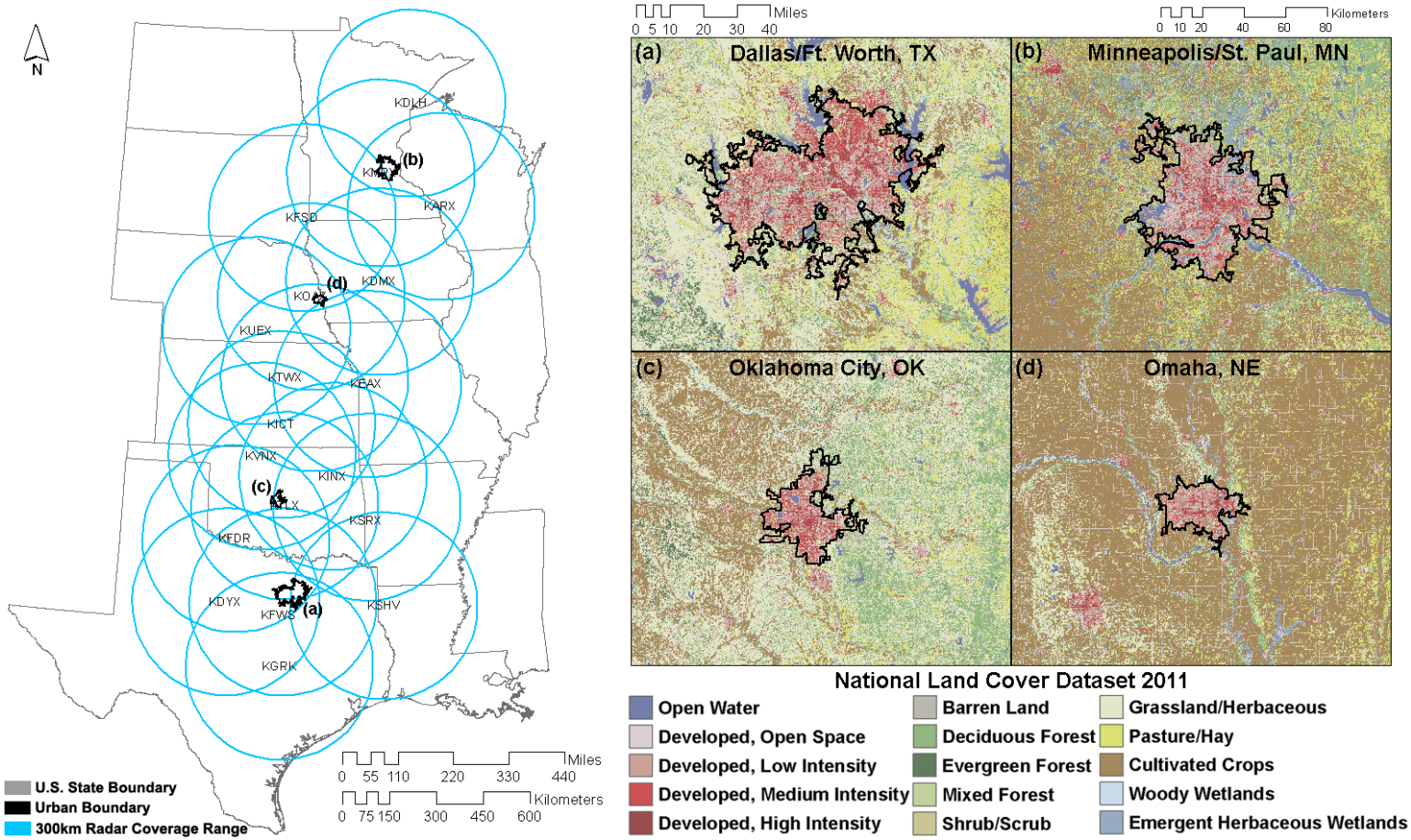


Figure 3.2: The study domain covering 2,177,084 km$^2$ of the Central Plains within the United States. The cities using the TIGER dataset (black contours; U.S. Census Bureau 2010) and 300 km radar coverage regions utilized in this study (blue circles) are shown on the left side. Land cover classification by the 2011 NLCD dataset around each city is on the right side.

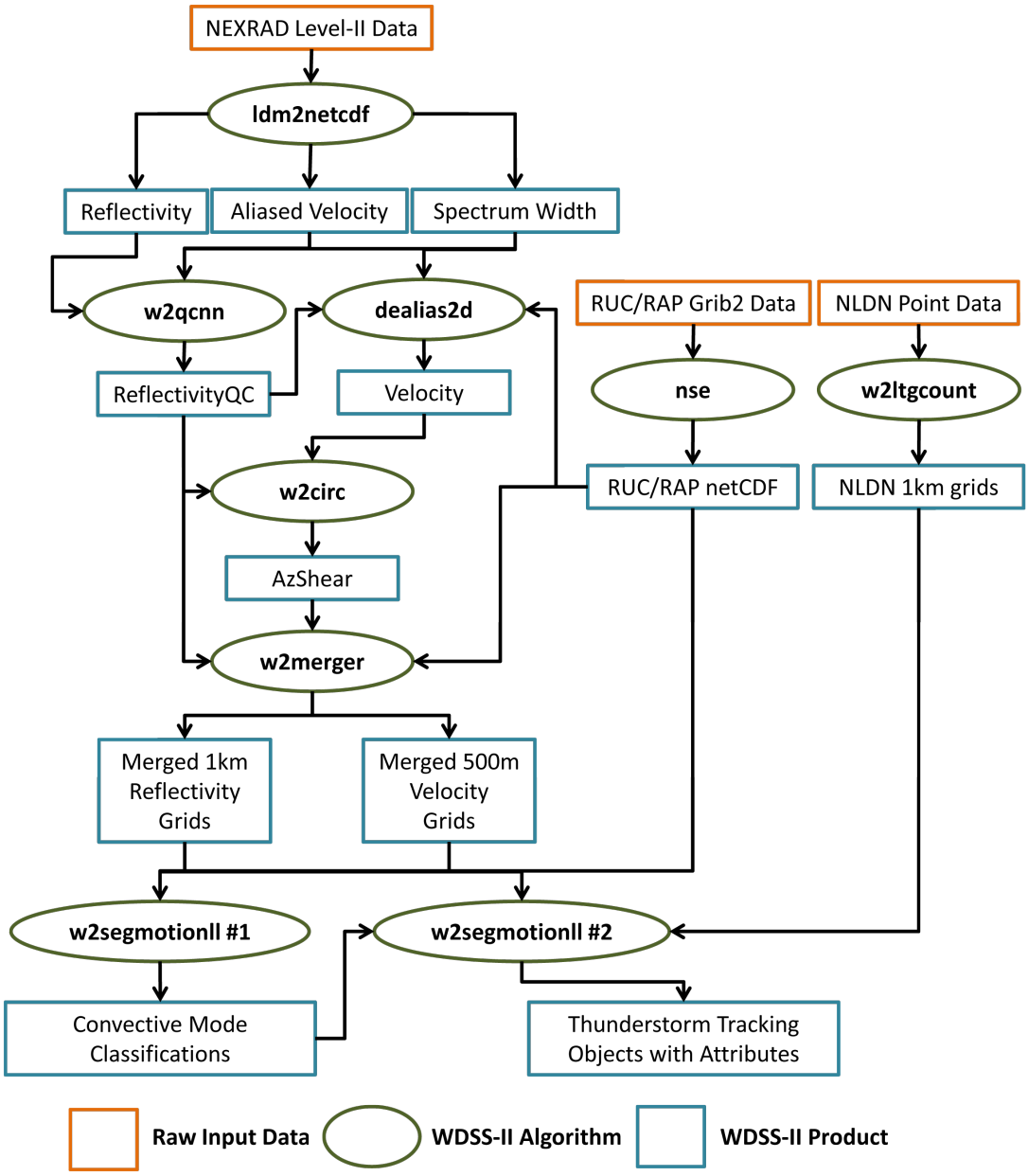


Figure 3.3: Radar, model, and lightning processing workflow using WDSS-II.

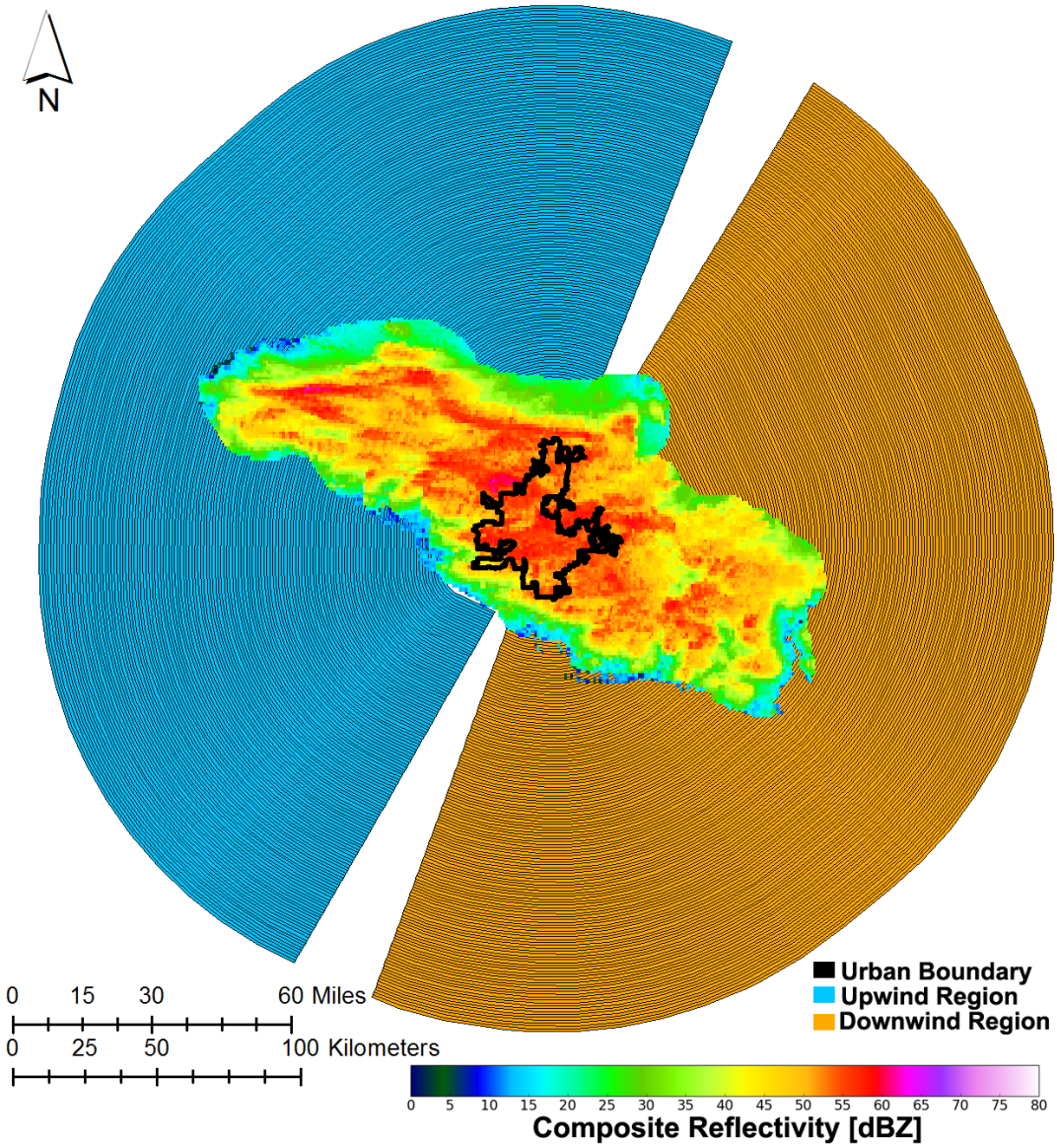


Figure 3.4: Maximum time-accumulated composite reflectivity in the upwind (blue) and downwind (orange) region for a tracked object passing over OKC on 31 May 2010. The gray lines in each region correspond to a 1 km sector to segment the reflectivity field by distance upwind or downwind from the urban area.

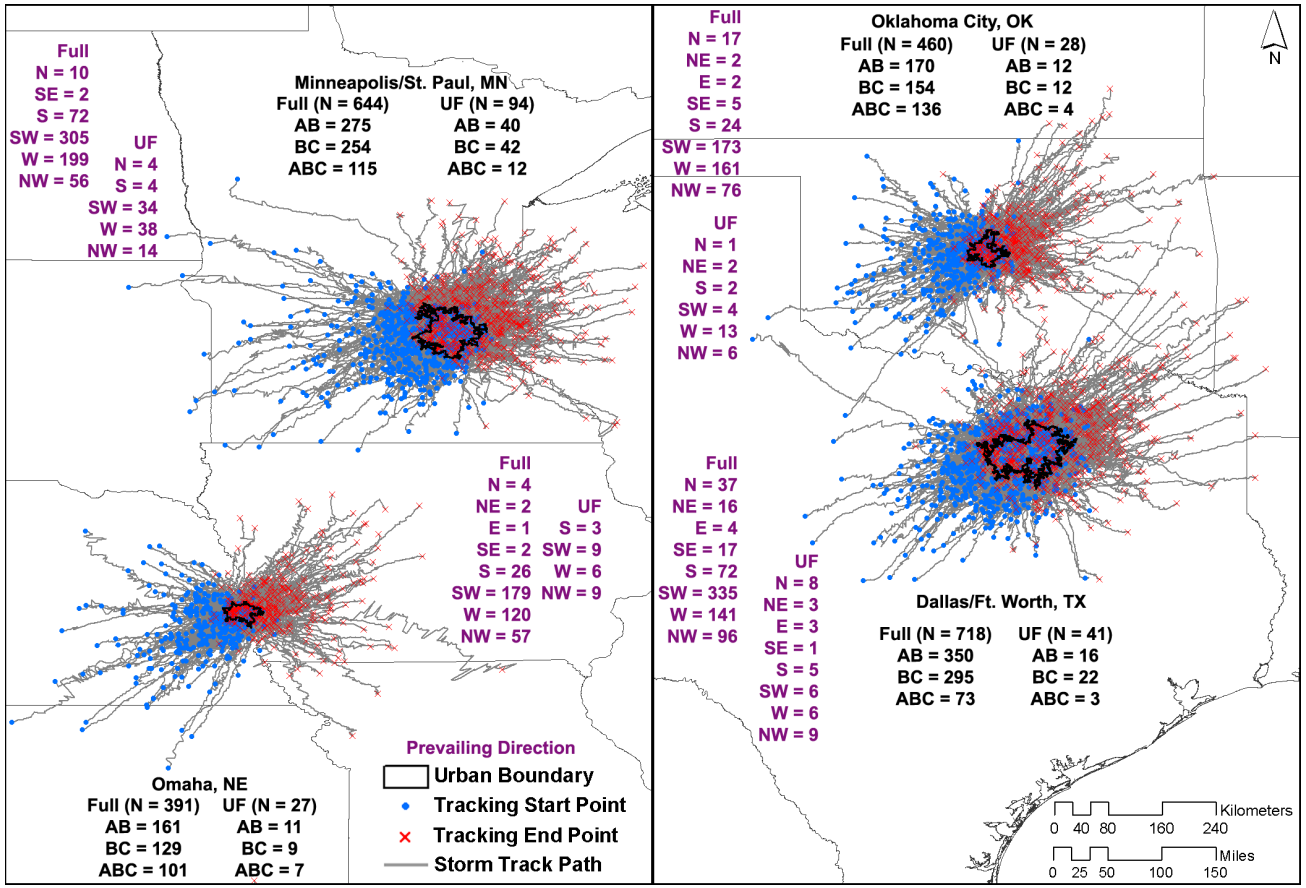


Figure 3.5: Storm tracks identified using the criteria specified in Section 3.4.2. The total number of storms occurring around each city along with the number of storms that started upwind and ended over the city (AB), started over the city and ended downwind (BC), and crossed all three regions (ABC) are annotated in black for the full climatology and UF subset. The prevailing direction of motion for thunderstorm objects in the full climatology and UF subset are annotated in purple.

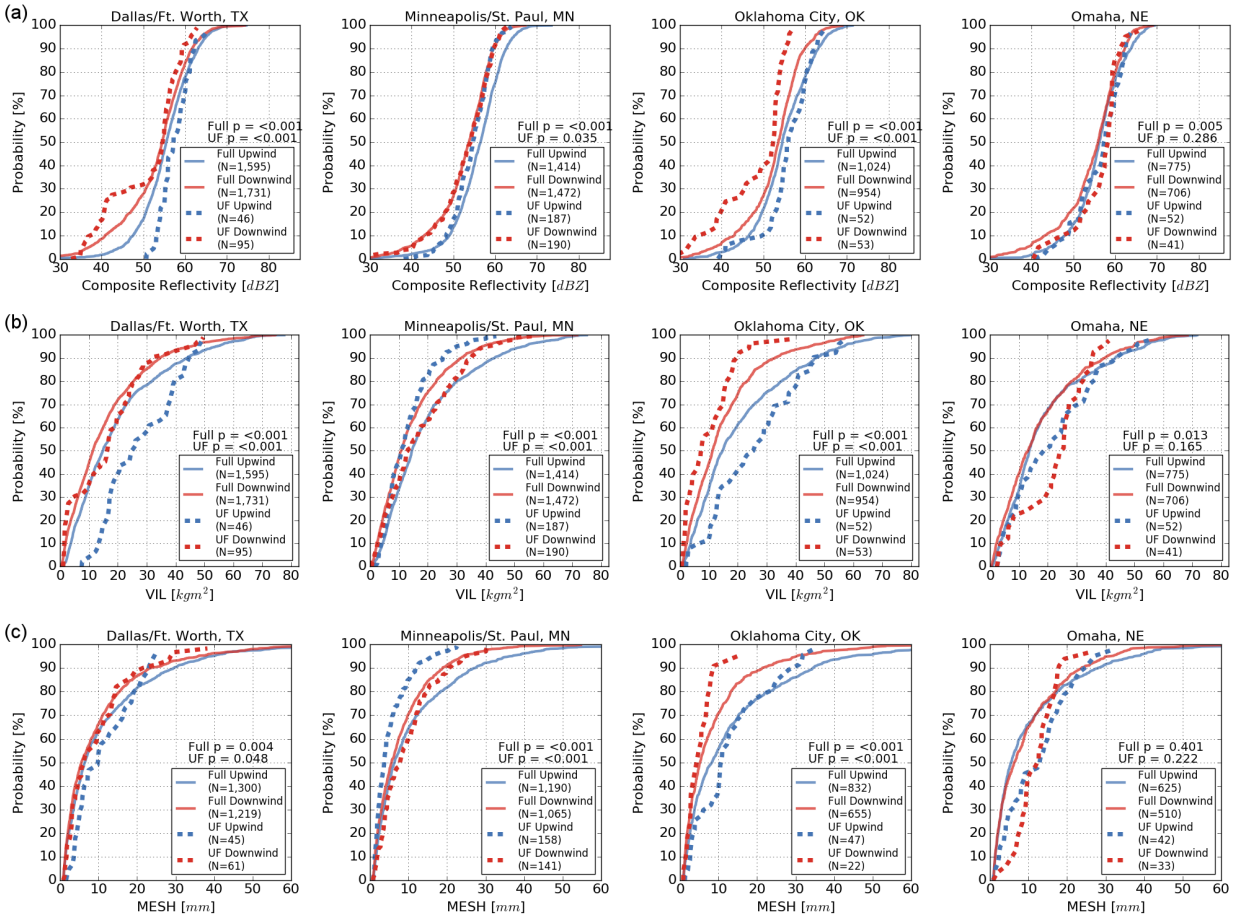


Figure 3.6: CDF plots of (a) maximum reflectivity, (b) VIL, and (c) MESH upwind (blue) and downwind (red) of each city. The solid lines are distributions from the full climatology and the dashed lines are distributions from the UF subset. The upwind and downwind distributions were compared for equality using a two-sample Kolmogorov-Simonov test.

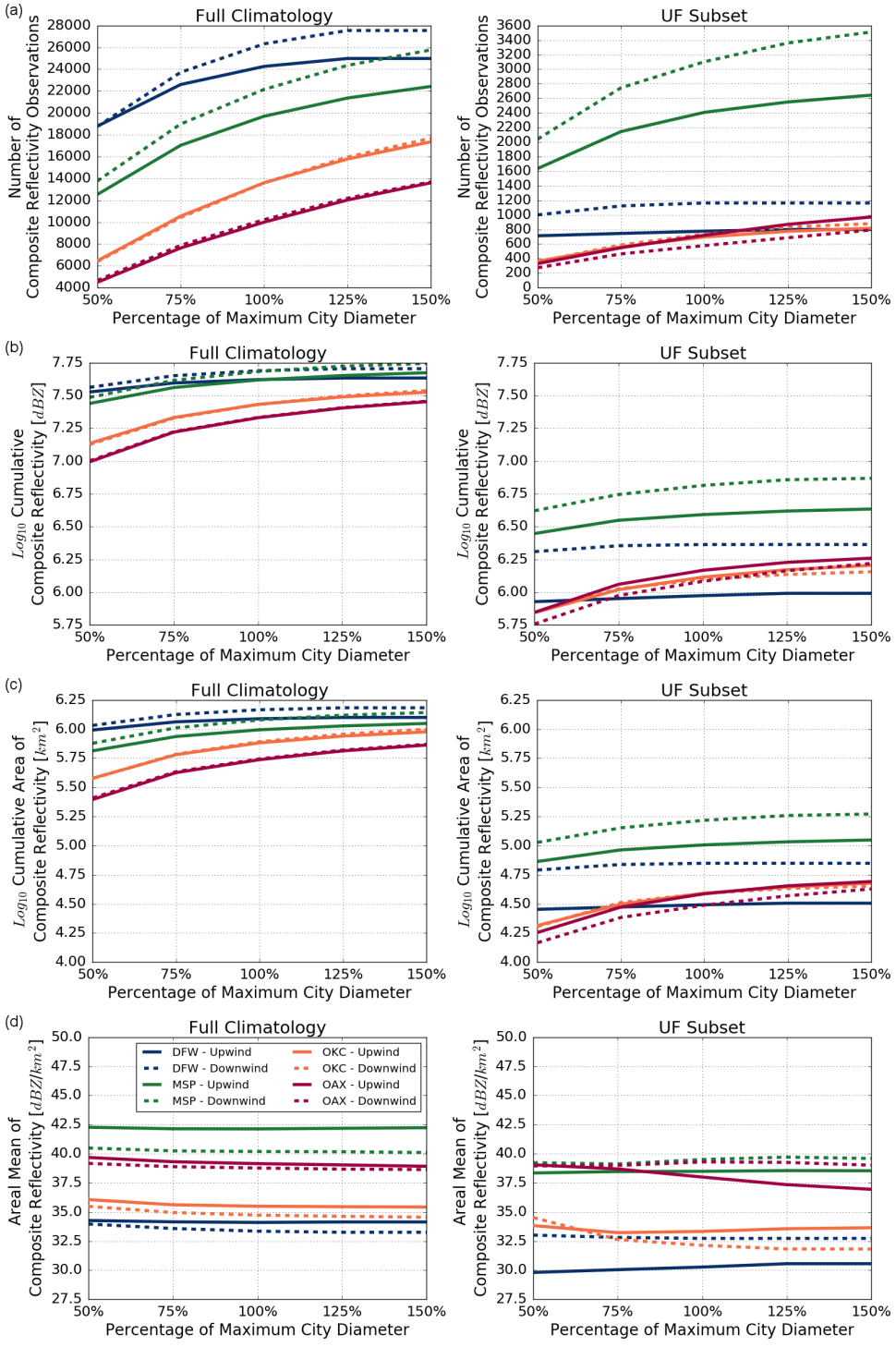


Figure 3.7: Values of composite reflectivity for the full climatology (left column) and UF subset (right column) at ranges upwind (solid line) and downwind (dashed line) 50% to 150% the maximum city diameter. These regions are summarized by (a) the number of thunderstorm objects; (b) the cumulative reflectivity; (c) the cumulative area affected; and (d) the areal mean composite reflectivity.

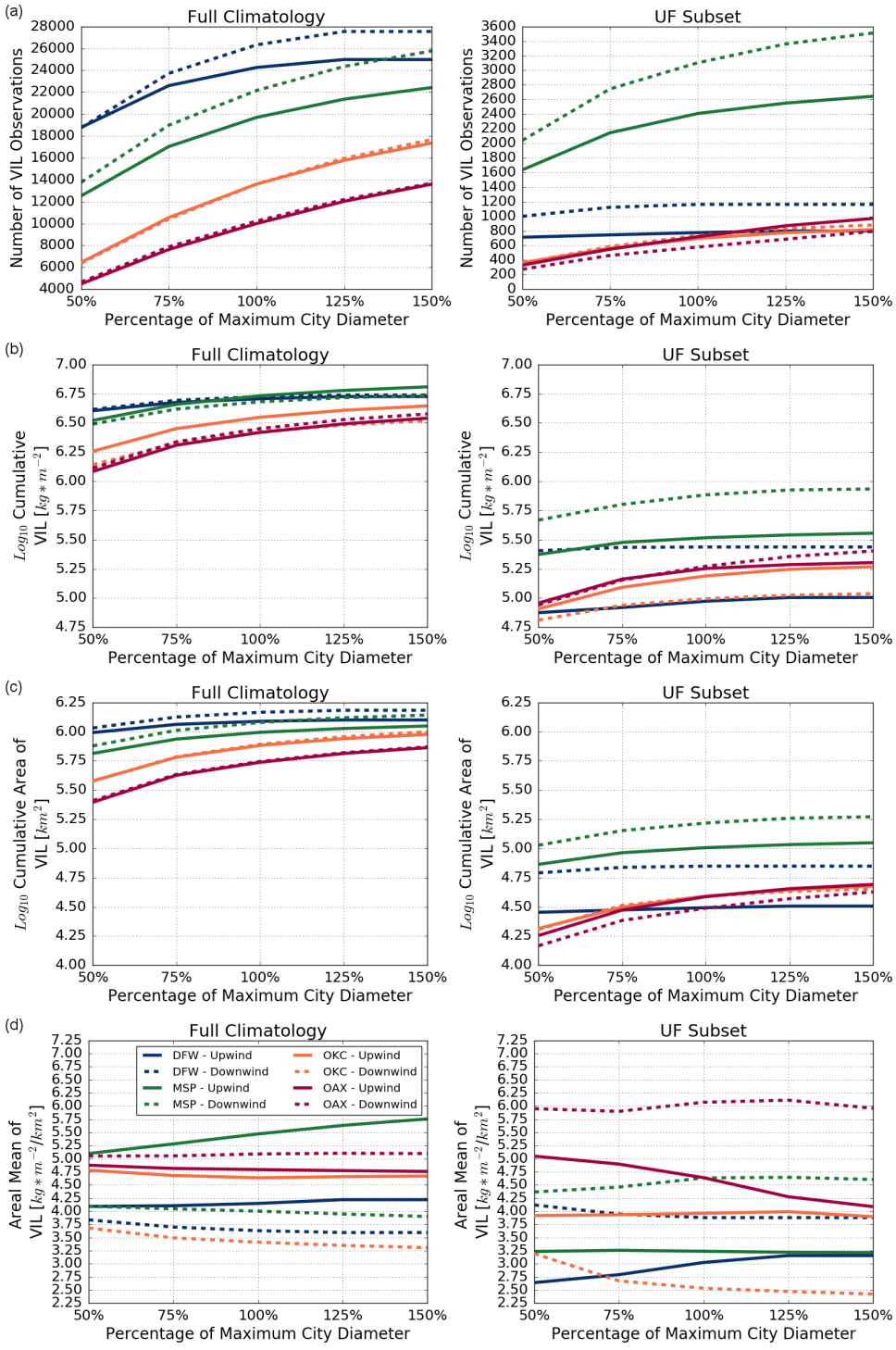


Figure 3.8: Same as Fig. 3.7 but for VIL

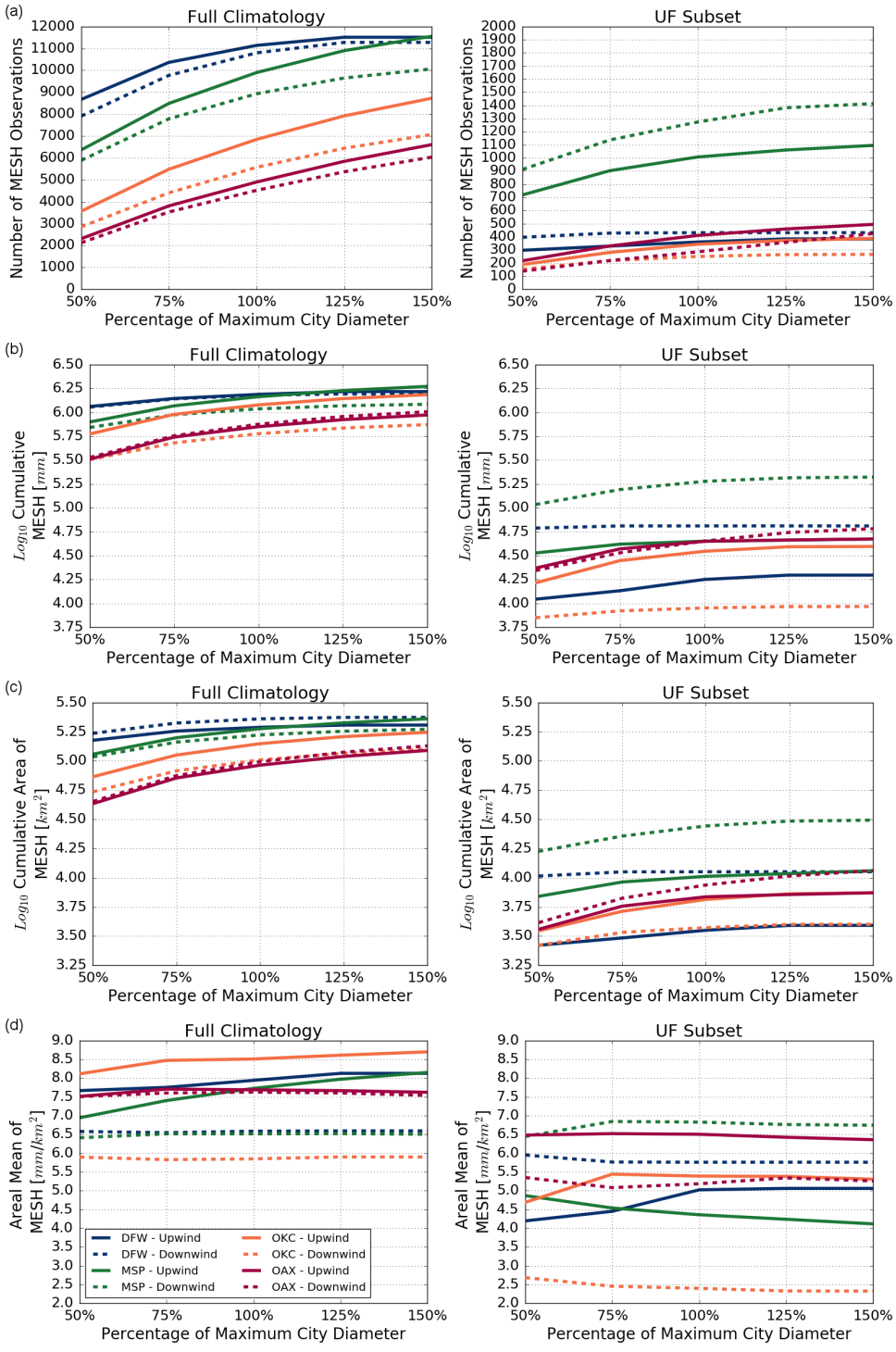


Figure 3.9: Same as Fig. 3.7 but for MESH

# Chapter 4

# Landsat Identification of Tornado Damage by Land Cover and an Evaluation of Damage Recovery in Forests

## Abstract

Multispectral satellite imagery provides a spaceborne perspective on tornado damage identification, however, few studies have explored how tornadoes alter the spectral signature of different land cover types. In part one of this study, Landsat surface reflectance is used to explore how 17 tornadoes modify the spectral signature, NDVI, and Tasseled Cap parameters inside forest (N=16), grassland (N=10), and urban (N=17) land cover. Land cover influences the magnitude of change observed, particularly in spring/summer imagery, with most tornado-damaged surfaces exhibiting a higher median reflectance in the visible and shortwave infrared, and a lower median reflectance in the near-infrared spectral ranges. These changes result in a higher median Tasseled Cap brightness, lower Tasseled Cap greenness and wetness, and lower NDVI compared to unaffected areas. Other factors affecting the magnitude of change in reflectance include season, vegetation condition, land cover heterogeneity, and tornado strength.

While vegetation indices like NDVI provide a quick way to identify damage, they have limited utility when monitoring recovery due to the cyclical seasonal vegetation

cycle. Since tornado damage provides an analogous spectral signal to forest clearing, we compare NDVI to a forest disturbance index (DI) across a five-year Landsat climatology surrounding the 27 April 2011 tornado outbreak in part two of this study. Pre-outbreak DI values remain relatively stable across seasons. In the five tornado-damaged areas evaluated, DI values peak within six months followed by a decline coincident with ongoing recovery. DI-like metrics provide a seasonally independent mechanism to fill the gap in identifying damage and monitoring recovery.

## 4.1 Introduction

### 4.1.1 Tornado Damage Surveys

In the wake of a tornado, ground and aerial surveys conducted by National Weather Service (NWS) personnel and partners provide a method to document the extent and intensity of the damage for use within studies regarding infrastructure resiliency (e.g., Marshall 2002; Federal Emergency Management Agency 2012), relationships between radar remote sensing and tornado strength (e.g., Toth et al. 2013; Kingfield and LaDue 2015; Smith et al. 2015), associations with tornado structure and dynamics (e.g., Davies-Jones et al. 1978; Fujita 1989; Karstens et al. 2013), and assessments of risk and vulnerability (e.g., Brooks et al. 2003; Ashley 2007). The enhanced Fujita (EF; Wind Science and Engineering Center 2006) scale, introduced in 2007 to mitigate deficiencies with the original Fujita (F; Fujita 1971) scale (e.g., Minor et al. 1977; Doswell III and Burgess 1988), provides guidance on estimated wind speed and destruction relationships for 28 damage categories and is the current standard for tornado surveys in the United States. While there is a demand to establish evaluation consistency for each survey (Edwards et al. 2013; Burgess et al. 2014), many surveys are incomplete or rushed due to the time-sensitive and intensive nature of surveying cou-

pled with workforce, training, and funding limitations (Doswell III and Burgess 1988; Doswell III et al. 2009). This leads surveyors to determine where the maximum damage occurred (Speheger et al. 2002), focusing on human-made structures that comprise 26 of the 28 EF-scale damage categories and often omitting non-urban or rural areas. While not a priority for storm surveys, damaged vegetation from natural hazards can influence radiative energy budgets and temperatures (Parker et al. 2005; Segele et al. 2005; McPherson 2007) and remain visible long after the initial event (Dyer 1988; Klimowski et al. 1998).

### 4.1.2 Multispectral Satellite Imagery

The use of spaceborne multispectral imagery has been encouraged (e.g., Bentley et al. 2002; Yuan et al. 2002; Jedlovec et al. 2006; Molthan et al. 2014) to supplement the information provided by damage surveys. Multispectral remote sensing provides a synoptic look at the Earth's surface by measuring radiation emitted or reflected from the Earth and captured by the satellite's multiple spectral bands. Each spectral band corresponds to a range of frequencies located along the electromagnetic spectrum and can span beyond the visible wavelength region, where human vision is constrained, into the near-infrared (NIR) and shortwave infrared (SWIR) wavelength regions.

The amount and spectral distribution of energy reflected by the Earth's surface is dependent on the surface characteristics with vegetation, soils, and human-made materials (Fig. 4.1) providing unique spectral signatures received at the sensor. In the case of healthy vegetation (Fig. 4.1a), plants will absorb more energy in the visible (0.4 – 0.7 $\mu$m) region while reflecting more energy in the NIR (0.75 $\mu$m – 1.35 $\mu$m) to aid in photosynthesis. As a plant senescences, the opposite behavior will occur in the spectral reflectance curve. Soils (Fig. 4.1b) can have a variable spectral signature that is dependent on their structure, particle size, and organic/mineral composition. Many

soils are highly reflective in the SWIR region (1.5 $\mu$m – 2.5 $\mu$m), however, wet soils tend to be less reflective in this region compared to dry soils (Gao 1996). Manmade materials (Fig. 4.1c) also provide a distinct spectral reflectance curve that is highly dependent on its construction composition.

Damaging winds and debris associated with tornadoes will alter the physical and spectral signature of the Earth's surface. The damage magnitude is dependent on several factors including the tornado strength, size, and makeup of the underlying land cover within the tornado swath (Jedlovec et al. 2006). For example, the scattering of human-made materials or scouring of the ground over areas of vegetation could disrupt the photosynthesis process, altering the difference in reflectance between the visible and NIR regions as well as enhance reflectance in the SWIR region.

### 4.1.3 Spaceborne Ratio-Based Analyses of Thunderstorm Damage

Initial observational studies of thunderstorm damage were often built around cases that were convenient due to relatively clear imagery received before and after the hazardous event. Many studies rely on change detection (Singh 1989) and use spectral vegetation indices, such as the widely adopted Normalized Difference Vegetation Index (NDVI), to identify the damage extent (Bentley et al. 2002; Yuan et al. 2002; Henebry and Ratcliffe 2003; Parker et al. 2005; Segele et al. 2005; Jedlovec et al. 2006; Wilkinson and Crosby 2010; Gallo et al. 2012; Wagner et al. 2012; Molthan et al. 2014). NDVI (Eq. 1) compares the reflectance of the visible red and NIR spectral ranges (Rouse Jr. et al. 1973; Tucker 1979).

$$NDVI = \frac{NIR - Red}{NIR + Red} \tag{4.1}$$

NDVI exploits the pattern that photosynthetically-active vegetation reflects a higher fraction of radiation from the NIR and absorbs more radiation from the red wavelength regions, resulting in a higher NDVI value. During ongoing plant senescence, the reflectance values of these two bands will be closer together, resulting in a lower NDVI. Since NDVI is an optical measurement of vegetation health, this ratio-based index can be influenced by atmospheric and viewing geometry effects (Bannari et al. 1995) and is sensitive to the background canopy (Huete and Jackson 1987; Huete 1988). Newer vegetation indices have been developed to manage these limitations (Bannari et al. 1995) but the spectral ranges required to calculate them may not be available across different sensor platforms. NDVI is subsequently viewed as a "continuity index" due to its availability through several generations of satellites and relevance to a collection of environmental monitoring studies (Huete et al. 2002). While rooted in studies of plant phenology, NDVI has been uniformly applied to both vegetated and urban/agricultural cover types in prior analyses of thunderstorm damage (e.g., Yuan et al. 2002; Jedlovec et al. 2006; Wagner et al. 2012).

For all orbiting multispectral sensors, there is an inverse relationship between spatial and temporal resolution. To assist in post-event response efforts, a few studies have sacrificed spatial resolution for update frequency by using sensors such as the Moderate Resolution Imaging Spectroradiometer (MODIS) (e.g., Jedlovec et al. 2006; Wilkinson and Crosby 2010). Jedlovec et al. (2006) compared 250 m spatial resolution MODIS imager data on-board the NASA Aqua and Terra satellites to higher spatial resolution imagery and found that MODIS-derived NDVI data may be sufficient at detecting tornado tracks rated F2 or higher, subsequently providing the ability for a timely assessment of damage extent; however, damage signatures appeared more clearly in areas of dense or homogeneous vegetation (higher pre-storm NDVI values) while damage was harder to distinguish in sparse or heterogeneous vegetation (lower pre-storm NDVI).

The MODIS red and NIR spectral bands are the only bands with 250 m spatial resolution, with the other 34 bands at 500 m or 1 km. This limits the creation of other vegetation indices beyond NDVI at an equivalent resolution. Evaluating all tornadoes within the Storm Data database from the National Centers for Environmental Information (NCEI) since the inception of the EF-scale (2007 through 2015), we found that 17.3% of the tornado records had an estimated maximum width exceeding 250 m. This is based upon the assumption that all database records are accurate, which may not be the case (e.g., Witt et al. 1998a). Regardless, a large majority of these tornadoes may not be observed using MODIS or sensors with similar spatial resolutions.

To address this limitation, other studies have used higher spatial resolution imagery ($\leq$ 30 m) to discriminate between damage and non-damage areas. Estimating the amount of agricultural loss due to thunderstorm damage on 12 August 1999, Bentley et al. (2002) compared NDVI calculated using Landsat 7 Enhanced Thematic Mapper Plus (ETM+) imagery and observed swaths of lower NDVI values where large hail occurred. Evaluating multispectral returns across a heterogeneous terrain, Yuan et al. (2002) used the Linear Imaging Self-Scanning III 23.5 m spatial resolution imagery to generate NDVI post-event and change products over a damage swath from the 3 May 1999 Oklahoma City, OK F5 tornado. They found spatial collocation between lower NDVI and F2+ tornado damage rated with some signal corresponding to F1 damage in rural areas. In another analysis of this tornado, Wagner et al. (2012) used Landsat 5/7 imagery to calculate NDVI alongside other indices and assess damage recovery over a three-year period. Recovery rates were mainly influenced by the amount and severity of the initial damage with the hardest hit regions never completely recovering.

### 4.1.4 Analyses of Disturbance

In other disciplines, disturbance identification is one of several techniques used to monitor and model ecosystem attributes (e.g., carbon emissions) within the larger Earth system (Cohen and Goward 2004). Forests damaged by natural hazards, human development, insects, and disease emit more carbon into the atmosphere while new and recovering forests pull carbon from the atmosphere (Odum 1969). Kauth and Thomas (1976) showed that all four spectral channels on the Landsat 1 Multispectral Scanner (MSS) contained relevant information to monitor vegetation health. By weighting the sums of the MSS bands, they derived Tasseled Cap indices of brightness and greenness. With the launch of the Landsat 4 Thematic Mapper (TM), the Tasseled Cap indices were redefined to use six TM spectral bands and expanded to add wetness derived from digital numbers (Crist and Cicone 1984) and surface reflectance (hereafter referred to as SR; Crist 1985). Tasseled Cap indices, particularly wetness, are a valuable predictor of forest structural attributes, and respond to the amount of green vegetation regardless of the background soil reflectance (Cohen et al. 1995). While the origin of Tasseled Cap is rooted in agricultural assessment, its utility has been explored for other land cover regimes, including urban regions (Crist and Cicone 1984; Deng and Wu 2012). From a data storage standpoint, a reduction in the number of variables stored from six Landsat spectral bands to three Tasseled Cap parameters have further promoted its usage for monitoring ecosystem disturbance across longer time scales (e.g., Cohen et al. 2002).

Capitalizing on the ability of Tasseled Cap to monitor ecosystem changes, particularly in forests, Healey et al. (2005) introduced a disturbance index (DI) technique that incorporates and reduces the three Tasseled Cap indices down to a single variable that highlights forest disturbance. Since its inception, DI has been used to describe decadal change in North American forests (Masek et al. 2008), fused with multi-resolution

satellite data (Hilker et al. 2009; Tran et al. 2016), and modified to evaluate grazing in New Zealand grasslands (de Beurs et al. 2016). Related back to thunderstorm hazards, (Baumann et al. 2014) used DI alongside a set of spectral and Tasseled Cap thresholds to discriminate, with greater than 75% accuracy, forest pixels that were disturbed by windfall. Their success with wind damage promotes the applicability of DI in identifying areas of forest damage by tornadoes which tends to be a more localized swath of defoliation and canopy damage; however, there has been little formal investigation on the application of DI in the identification of tornado damage to date.

### 4.1.5 Motivation

In this study, we expand upon the existing knowledge base of tornado damage identification in two ways. In the first part of this study, we use Landsat 5 TM and Landsat 7 ETM+ imagery to explore how tornadoes change the spectral reflectance curves of forests, grasslands, and urban environments across different geographic regions in the United States.

Tree damage by tornadoes, particularly in forested regions, account for two of the 28 damage categories in the EF-scale, yet are a low priority for damage survey teams. For the second part of this study, we compare the DI technique of Healey et al. (2005) to NDVI in the immediate and longitudinal identification of tornado damage in forests through a five-year climatology of Landsat imagery surrounding the 27 April 2011 tornado super outbreak, where over 199 tornadoes occurred across the southeastern United States in one day (Knupp et al. 2014).

## 4.2 Data & Study Region

### 4.2.1 Landsat Data

We acquired Landsat 5 TM and Landsat 7 ETM+ SR data from the United States Geological Survey (USGS) EarthExplorer platform. The USGS uses the Landsat Ecosystem Disturbance Adaptive Processing System (LEDAPS; Masek et al. 2006) to atmospherically correct, quality control, and create the SR products. This correction mitigates atmospheric effects (i.e., aerosols and other radiative scatterers) and provides a more accurate estimate of solar radiation reflected by the Earth's surface compared to uncorrected, top-of-atmosphere measurements. Furthermore, a new cloud masking algorithm (CFMask) was added to LEDAPS to identify cloudy, cloud-adjacent, and cloud shadowed pixels. This algorithm performs better at identifying these features than the legacy masking algorithm (Zhu and Woodcock 2012) and was used in this study to remove all pixels not classified as "clear".

### 4.2.2 Land Cover Data

The National Land Cover Database (NLCD; Homer et al. 2015) provides a 30 m spatial resolution grid of 20 land cover classes derived from the classification system of Anderson et al. (1976). Since 2001, this database has been updated every five years with newer versions released for 2006 and 2011. In this study, we applied the most recent NLCD database prior to each tornado date to classify the land cover. For forest identification, we selected the deciduous (class 41), evergreen (class 42), and mixed (class 43) classification categories. For grassland identification, we only used the grassland/herbaceous (class 71) category as the other three herbaceous categories are native to Alaska. For urban identification, we used all four developed classifications (classes 21-24) ranging from open space to high intensity. While NLCD provides clas-

sification for pasture/hay (class 81) and cultivated crops (class 82), we did not evaluate these agricultural land cover types due to the inter-season variability of harvest cycles.

### 4.2.3 Case Selection & Study Domain

NCEI maintains a tornado database dating back to 1950 with most tornado records containing an estimated start/end time and location of occurrence. In part one of this study, we selected tornadoes with Landsat TM/ETM+ imagery within 30 days of occurrence over a diverse range of geographic regions in the United States. Imagery with visible ground scouring and previously studied tornadoes were prioritized as they corroborate with the storm event and literature record. In total, we selected 17 tornadoes (Table 4.1) occurring within 12 Landsat image tiles (black squares; Fig. 4.2).

In part two of this study, we focus on using DI to assess damage recovery in forested regions. To standardize the image times across the five-year study period, we selected five tornadoes (purple polygons; Fig. 4.2) with visible ground scouring from Landsat path 21/row 37 imagery covering portions of west-central Alabama and eastern Mississippi. For this path/row, we downloaded all Landsat 5/7 SR imagery from 1 January 2009 to 31 December 2013. Since DI was originally created for forest damage, we used the 2011 NLCD dataset coupled with the CFMask product to determine the percentage of clear-sky forest pixels in each image. Images with $\geq 10\%$ cloud cover over forests were discarded. The Landsat 7 scan line corrector (SLC) failed after May 2003 and results in a 22% reduction in data coverage (Markham et al. 2004). Forest pixels within these missing data regions were treated like cloud-masked pixels. In total, 19 Landsat 5 and 30 Landsat 7 images were available for data analysis. Since the Landsat 5 mission ended in November 2011, all remaining images over the five-year period were from Landsat 7.

## 4.3 Methods

### 4.3.1 Background & Damaged Pixel Identification

We used the tornado record from NCEI alongside methods used in prior studies, such as the calculation of vegetation indices (Jedlovec et al. 2006; Wagner et al. 2012) and principal components analysis (Yuan et al. 2002; Molthan et al. 2014), as guidance to manually contour a damage polygon, as shown in Figure 4.3 for the Jasper County, MO tornado (tornado J). With many modern tornado records only providing a start/end location along with a maximum length and width of unknown accuracy, manual contouring standardizes the damage identification process and allows for a non-uniform 2D region to be identified.

To assemble a dataset of pixels unaffected by the tornado (hereafter referred to as background), we calculated a spatial buffer 10 km to 60 km away from the damage polygon. This buffer size ensures a sufficient number of pixels exists for re-sampling even if the tornado track was near the edge of an image. To ensure the smaller damage and larger background regions have the same sample size and land cover distribution, we randomly sampled the background region without replacement. Imagery with multiple tornadoes or other thunderstorm hazard damage (e.g., hail streaks) had these other regions masked out using a 10 km buffer during the background resampling procedure.

### 4.3.2 Calculation of NDVI and Tasseled Cap Indices

#### 4.3.2.1 Individual Bands & NDVI

The 30 m bands of Landsat TM/ETM+ SR (bands 1-5 and 7) served as six of the ten inputs evaluated in part one of this study. These six bands, each consisting of a small spectral range, together provide the spectral reflectance of targets from the

visible to SWIR wavelength regions (Table 4.2). Due to the commonalities in spectral range between the sensors, we will hereafter refer to individual Landsat bands by their center wavelength or band category independent of the sensor. NDVI was calculated by using the SR values from the red (0.66 $\mu$m) and NIR (0.83 $\mu$m) bands (Eq. (4.1)).

#### 4.3.2.2 Tasseled Cap Indices

Crist (1985) derived the transformation coefficients (Table 4.3) for the visible to SWIR reflectance bands using the Landsat 4 TM to calculate Tasseled Cap brightness, greenness, and wetness which are the foundation to calculate DI (Healey et al. 2005). These coefficients were developed with ground measurements to mitigate errors from atmospheric effects. Given the similarities in the spectral ranges between Landsat 5 and 7 (Table 4.2) coupled with the use of LEDAPS to atmospherically-correct all imagery, we use the coefficients from (Crist 1985) to calculate the Tasseled Cap indices for both satellite platforms. The interpretation of the Tasseled Cap indices is dependent on the targets being analyzed (Crist and Cicone 1984). Brightness is the weighted sum across six input bands and represents the overall reflectance. Greenness is the contrast between the NIR (0.83 $\mu$m) and the visible bands (0.49 $\mu$m – 0.66 $\mu$m) for vegetation identification and monitoring. Wetness contrasts the SWIR (1.67 $\mu$m – 2.24$\mu$m) with the visible/NIR wavelength regions to quantify soil moisture content and vegetation density. While the Tasseled Cap has origins in monitoring vegetation response, these indices have also been used to discriminate vegetation, high albedo, and low albedo regions in urban areas (Deng and Wu 2012).

#### 4.3.2.3 DI Calculation in Forests

For part two of this study, we use the Tasseled Cap indices above and follow the methods of Healey et al. (2005) to generate a DI image. The DI calculation uses a lin-

ear combination of normalized Tasseled Cap indices ($\text{Brightness}_n$, $\text{Greenness}_n$, and $\text{Wetness}_n$) to determine how far, in terms of standard deviation, each individual forest pixel is from the global mean of forests of the same species (or land cover type). In our study, we segment each image into one of the three NLCD forest classes (i.e., deciduous, evergreen, and mixed) and calculate an image-wide mean ($\mu$) and standard deviation ($\sigma$) for each Tasseled Cap parameter and forest class. At each pixel, we then standardize each local Tasseled Cap parameter by the image-wide $\mu$ and $\sigma$ associated with its forest class and parameter (e.g., as shown for $\text{Brightness}_n$ in Eq. (4.2)). Finally, these three standardized values are combined to calculate DI (Eq. (4.3)). This process is repeated for all forest pixels in an image.

$$Brightness_n = \frac{Brightness_{pixel} - \mu_{Brightness}}{\sigma_{Brightness}} \tag{4.2}$$

$$DI = Brightness_n - (Greenness_n + Wetness_n) \tag{4.3}$$

The DI equation is based upon the assumption that clear cut forests will exhibit an increase in brightness and decrease in greenness and wetness compared to surrounding undisturbed forests. The DI value is interpreted as the spectral distance from that pixel to a mature pixel of the same forest class. Interpreting the change in DI over time shows that large positive shifts correspond to disturbance while large negative shifts correspond to regrowth (Healey et al. 2005; Masek et al. 2008; Tran et al. 2016).

Evaluating disturbance in three forests, Healey et al. (2005) observed mean DI values $\geq 2$ in areas affected by disturbance events. de Beurs et al. (2016) notes that setting a DI $\geq 2$ as a threshold for disturbance can misclassify disturbed pixels 25% of the time. Setting higher DI threshold will lower the misclassification rate, but could potentially eliminate identification of lower magnitude disturbance events. Baumann

et al. (2014) found that windfall regions were best identified at a DI threshold between 2.5 and 3. Incorporating the concerns of de Beurs et al. (2016), we have chosen a more conservative DI threshold of 3 in part two of this study.

In our exploration of DI, we are only interested in disturbance caused by tornadoes. To mitigate pre-existing forms of disturbance from being misidentified as tornado damage, we identified all pre-disturbed pixels (DI $\geq$ 3) in the 2 April 2011 Landsat 7 image prior to the tornado outbreak. All forest pixels failing LEDAPS quality control in the 2 April 2011 image were re-checked in older Landsat images. After identification, all pre-disturbed pixels were removed from the calculations of DI and NDVI for the entire five-year period.

## 4.4 Results - Identifying Tornado Damage by Land Cover

Comparing the sample sizes of urban, forest, and grassland pixels affected by tornadoes (Table 4.4), we found that forests were the most affected land cover type in 13 of the 17 tornadoes followed by urban areas (three) and grasslands (one). We removed tornadoes from an individual land cover analysis with fewer than 100 pixels as the poor sample sizes skewed the distributions of SR, Tasseled Cap indices, and NDVI. After applying this threshold, we removed one forest case (tornado F), and seven grassland cases (tornadoes D, F, G, H, J, M, and Q in Table 4.4).

### 4.4.1 Urban Land Cover

All tornadoes had at least 100 damaged urban pixels ranging from 123 (tornado N) to 5530 (tornado J) corresponding to the EF5 tornado that devastated Joplin, MO on 22 May 2011. Compared to the control background region, all tornado-damaged urban areas had a higher reflectance in the visible (0.49 – 0.66 $\mu$m) and SWIR (1.67 – 2.24 $\mu$m) and most areas exhibited a lower reflectance in the NIR region (0.83 $\mu$m) (Fig.

4.4a). In the blue (0.49 $\mu$m) and green (0.56 $\mu$m) regions, the SR was around 15% higher while red (0.66 $\mu$m) and SWIR (1.67 $\mu$m – 2.24 $\mu$m) values were around 25% higher in the damaged region. Changes in NIR (0.83 $\mu$m) SR were much smaller with many tornado-damaged areas having around a 5% lower reflectance compared to the background region. The general increase in SR measured across most Landsat bands corresponded to a 25% higher median Tasseled Cap brightness in the damage polygon. With NIR reflectance holding the largest and only positive weighting coefficient in the greenness calculation (Table 4.3) coupled with many pixels registering a lower NIR reflectance, median greenness values were around 25% to 60% lower in the damaged areas. The negative weights in the wetness calculation paired with higher SWIR SR inside the damage polygon results in median wetness being 25% to 75% below the median wetness values in the background region. The altered spectral signature in tornado-damaged urban pixels also yields a decline in median NDVI due to higher reflectance at 0.66 $\mu$m and lower reflectance at 0.83 $\mu$m. For example, the tornado-damaged areas associated with tornado P were around 64% more reflective at 0.66 $\mu$m but around 1% less reflective at 0.83 $\mu$m. This contraction in the red edge between the 0.66 $\mu$m and 0.83 $\mu$m bands yields a median NDVI of 0.26 in the damage region compared to 0.48 in the background region. This corroborates well with other observations of decreases in NDVI due to tornadoes (e.g., Yuan et al. 2002; Jedlovec et al. 2006; Molthan et al. 2014).

The spectral reflectance of urban environments is dependent on the infrastructure density and is a contributing factor in evaluating the magnitude of tornado damage. In the case of the Jasper, MO tornado (tornado J), pixels classified as open space urban (Fig. 4.5a) saw a larger decline in median NDVI (-0.18) compared to high density urban pixels (-0.06, Fig. 4.5b). Open space urban areas are more likely to consist of a mixture of constructed materials and vegetation while high density regions are predominantly composed of impervious surfaces (Homer et al. 2015). As expected,

Landsat TM/ETM+ measures a lower reflectance in the visible wavelengths and higher reflectance at 0.83 $\mu$m in the open space region compared to the high intensity regions likely corresponding to photosynthetic activity in these vegetated areas. After the tornado occurs, the likely addition of debris covering/shadowing the open space vegetation coupled with an inconsistent defoliation of the vegetation area and displacement of dirt/soil increases reflectance in the visible and SWIR and decreases reflectance in the NIR spectral ranges. In high density urban areas, the increased amount of human-made material and impervious surfaces (Fig. 4.1c) results in a higher initial reflectance in the visible and SWIR wavelength regions. After the tornado, only the 0.66 $\mu$m and 2.27 $\mu$m regions showed increased reflectance between 3% to 5% above the background field while up to an 8% decline in median reflectance was measured in the other Landsat spectral ranges. In the Tasseled Cap space, background high density urban areas are brighter and have lower greenness and wetness values than open space urban areas. Tornado-damaged open space urban areas have a higher median brightness (0.07), and lower median greenness (-0.08) and wetness (-0.11) values whereas high density pixels do not deviate as far from the background in measures of central tendency. However, tornado-damaged pixels in both urban land cover types have a smaller interquartile range (IQR) across the spectral reflectance curve and this corresponds to a lower point spread in the Tasseled Cap space.

One other observation of note is related to the potential seasonal effects on the spectral signature of cities. The Scott-Newton, MS (tornado N) and Marshall, MS (tornado Q) events occurred in the fall and winter months. In both events, NIR reflectance in tornado-affected urban land cover was 15% and 13% higher than the background region; however, red reflectance also was 38% and 24% higher respectively. While both cases still resulted in a decline in NDVI, the density distribution of urban environments and background signal coupled with season can hinder tornado damage identification using automated techniques trained based on trends observed only in the spring and

summer.

### 4.4.2 Forest Land Cover

Forest land cover showed the most consistent change across all parameters evaluated for the 16 valid tornado events. Comparable to urban area trends, tornado-damaged forests have a higher visible (0.49 $\mu$m – 0.66 $\mu$m) and SWIR (1.67 $\mu$m – 2.24 $\mu$m) reflectance and a lower NIR (0.83 $\mu$m) reflectance (Fig. 4.4b). Comparing damaged and background SR in tornadoes D (Fig. 4.6a), E (Fig. 4.6b), and G (Fig. 4.6c) shows these trends are geographically independent with documented occurrences in Wisconsin, Missouri, and Mississippi respectively. In these three cases, the SR of tornado-damaged forests was around 25% to 69% higher in the blue/green (0.49 – 0.56 $\mu$m), 70% to 134% higher in the red (0.66 $\mu$m), 17% to 34% lower in the NIR (0.83 $\mu$m), 40% to 65% higher in the SWIR (1.67 $\mu$m), and 79% to 144% higher in the SWIR (2.24 $\mu$m) spectral regions. Defoliation, broken limbs, and downed trees will reduce the amount of photosynthetic vegetation and subsequently result in higher reflectance values in the visible and lower reflectance in the NIR spectral regions; the opposite spectral behavior of a region with healthy vegetation. Reflectance in the SWIR wavelength region is inversely related to the amount of moisture in vegetation (Schroeder et al. 2011) and directly related to the soil background (Cohen and Goward 2004). The limited amount of healthy vegetation to retain moisture and higher probability of soil exposure due to canopy defoliation are two of the potential drivers for the increase in SR observed here.

In the Tasseled Cap space for these three tornadoes we observe an increase in brightness, and decrease in greenness and wetness in the region damaged by the tornado; this corroborates with other studies of forest damage (e.g., Cohen and Goward 2004; Healey et al. 2005; Baumann et al. 2014). However, these changes can be

variable depending on the damage extent as downed/stripped trees can leave shadows across the affected area that lowers brightness and increases wetness when compared to regions where trees are completely removed (Baumann et al. 2014). A comparison of the IQRs between the two pixel areas reveals a larger spread in the SWIR wavelength region. This is likely due to contributions of increased visibility of the soil background coupled with vegetation damage compared to healthy forests in the same geographic area and also results in a wider range of wetness values measured in the Tasseled Cap space. The IQRs in the visible and NIR wavelengths between the damaged and background domains are volatile and ultimately dependent on both the species of vegetation affected, position in the natural vegetation growth/decay cycle, and magnitude of damage that can fluctuate across the tornado lifecycle (Holland et al. 2006).

Alongside the disruption of the photosynthesis process and exposure of the soil background in forests, another factor that can influence SR returns in tornadoes is the displacement of debris from one land cover region onto another. In both the Cleveland, OK (tornado P; Fig. 4.7a) and Jasper, MO (tornado J; Fig. 4.7b) tornadoes, forest pixels are dispersed around expansive urban areas that comprise 94.6% and 76.9% of the damage polygon area respectively. Median SR values of forests were between 110% to 242% higher in the visible, 88% to 186% higher in the SWIR, and around 6% lower in the NIR spectral ranges compared to the background. While the reflectance departures follow the same pattern as other forest analyses (e.g., Fig. 4.6a-c), the collocation with the urban environment allows for the scattering of human-made debris and could be an additional factor driving reflectance upwards in the visible and SWIR wavelengths.

### 4.4.3 Grassland Land Cover

Comparable to urban and forested regions in terms of the directional change in reflectance, most tornado-damaged grasslands registered median reflectance values around 15% to 25% higher in the visible and SWIR and 5% lower in the NIR (Fig. 4.4c). The Canadian-Kingfisher-Logan, OK (tornado L) event produced damage in a rural portion of northwest Oklahoma and contained the highest number of damaged grassland pixels (N=11,158). Five days after the tornado, median SR values of tornado-damaged grasslands are around 24% to 44% higher in the visible (0.49 $\mu$m – 0.66 $\mu$m) and SWIR regions (1.67 $\mu$m – 2.64 $\mu$m) and slightly lower with a 2% decrease in the NIR region (0.83 $\mu$m) compared to the background region (Fig. 4.8a). The decline in NDVI tends to be more dependent on the red (0.66 $\mu$m) SR as this departs further from the background over the NIR reflectance. Comparable to other land cover types, these spectral signatures from the background resulted in an increase in median brightness and decrease in greenness and wetness.

Similar to observations of damaged forests collocated within urban areas, grasslands around the EF5 tornado affecting Cleveland, OK (tornado P; Fig. 4.8b) had greater differences in SR between the damaged and background regions. SR values were 37% to 90% higher in the visible and SWIR and around 1% lower in the NIR spectral ranges. The increase in red reflectance translates to a lower median NDVI (0.38) compared to the background (0.62). These larger departures in median reflectance between the damaged and background regions also translates to the greatest differences in the Tasseled Cap indices with an increase in median brightness (0.11) and a decrease in greenness (-0.07) and wetness (-0.10). Tornado N was the only grassland tornado sampled in the fall region and showed a 3% increase in the visible blue (0.49 $\mu$m) and a decline in all remaining bands ranging from 2% to 17% compared to the background region (Fig. 4.8c). In this case, the Tasseled Cap indices show the

opposite of most other tornado damage tracks with a decrease in median brightness (-0.02) and increase in median greenness (0.01) and wetness (0.04). While the median NIR reflectance is lower than the background region, the distribution of values is negatively skewed and results in a higher median NDVI measured in the damaged region. Similar to forests, the IQR of each spectral region does not follow a common trend across different tornadoes. In the case of tornado L (Fig. 4.8a), the IQR of each Landsat band is smaller in the damage region while the opposite is true in tornado N (Fig. 4.8c). The amount/extent of damage produced by the tornado, vegetation strength, soil type, season, and debris lofting from surrounding land cover are several factors that can change the spectral behavior of vegetated areas. Furthermore, unlike forests and urban land cover, spectral signatures of grasslands are more susceptible to external influences (e.g., drought, grazing, land management practices; Turner et al. 1992; de Beurs et al. 2016) and can hinder the identification of damage. Jedlovec et al. (2006) observed that manual and automated identification of damage signatures was easier when evaluating areas of dense vegetation (e.g., standing trees) while regions of open grassland provided a lower detection efficiency.

## 4.5 Results - Tracking Damage Over Time: DI vs. NDVI

In part one of this study, forests comprised a majority of the contoured damaged pixels in 47% of the tornadoes evaluated with most forests exhibiting an increase in median Tasseled Cap brightness, and a decrease in greenness and wetness. This is analogous to a disturbance signal that would be visible using DI. The five tornadoes selected for part two occurred within the April 27, 2011 tornado outbreak with damage lengths ranging from 20.3 km to 258.6 km, maximum widths from 307.3 m to 2306.6 m, and forests constituting 41% to 81% of the damaged area (Table 4.5; Fig. 4.2). In a Landsat 7 image acquired on 4 May 2011, seven days after the tornado outbreak, a compari-

son between the damage and background regions for all tornadoes shows a spectral signature similar to observations in forests across other locations. The extent of the damage as related to differences in reflectance between the damage and background regions is correlated to the intensity of the tornado. In the case of the Wateroak tornado (Fig. 4.9a), SR values were around 18% to 50% higher in the visible, 11% lower in the NIR, and 17% to 38% higher in the SWIR region. For the Tuscaloosa-Birmingham tornado (Fig. 4.9b), the widest tornado in our DI dataset, SR values were between 28% to 115% higher in the visible, 18% lower in the NIR, and between 39% to 78% higher in the SWIR spectral regions. Accordingly, these SR departures permeate into the calculations of NDVI and DI. For the Wateroak tornado, the damage region had a lower median NDVI of 0.81 and a higher median DI of 0.95 compared to the background region at 0.89 and -0.99 respectively. In the stronger Tuscaloosa-Birmingham tornado, the median NDVI (DI) inside the damage region was 0.72 (3.40) compared to the background region at 0.88 (-0.97).

A comparison of DI to NDVI across the entire five-year period for the smallest (Fig. 4.10a) and largest (Fig. 4.10b) tornadoes reveals two distinct patterns before and after the tornado outbreak. Before the outbreak, DI remains stable in both the damage and background regions with the median DI remaining at or below zero and the total percentage of disturbed pixels remaining below 10% for a majority of images. As expected, NDVI over the same period varies with the seasons with median NDVI values peaking around 0.89 in the mid-summer months and reaching a minimum around 0.53 in the winter months. Due to this known variability of NDVI across seasons, employing change detection techniques can provide very different results depending on the amount of time between the images. For example, over the period between March and May 2010, median NDVI across the background region increases from 0.56 to 0.79. Over this same period, we also observe increases in Tasseled Cap brightness (0.08), greenness (0.14), and wetness (0.05) in conjunction with more widespread growth and

coverage of foliage within these forests. However, since a global mean and standard deviation are calculated within each image, the resulting summary statistics of DI are seasonally independent. This process of standardizing based on the current global spectral reflectance is the biggest strength of DI and mitigates several sources of cross-temporal signal contamination (i.e., vegetation growth cycles, droughts) that would be observed in standard ratio-based indices such as NDVI.

A comparison of both indices after the tornado outbreak provides additional evidence supporting the usage of DI or the calculation of a DI-like index. For the Wateroak and Tuscaloosa-Birmingham tornadoes, the percentage of disturbed pixels escalates rapidly with 25% and 60% of the respective swaths classified as disturbed within 6 months following the tornado outbreak. Over time, both the percentage of disturbed pixels and median DI converge towards the background signal. Alternatively, there is a decline in median NDVI after the tornado outbreak that continues to fluctuate with the seasons. Similar to DI, NDVI will converge with the background signal, as is observed with the Wateroak tornado in the latter part of 2013 (Fig. 4.10a).

To bypass the dependence on season with indices like NDVI, prior multi-year studies of tornado damage have solely used data from within the same season (e.g., Wagner et al. 2012). DI has utility in allowing for imagery to be pulled from any season and assembled into a time-series, providing a way to track and monitor damage year-round. For four of the five events (excluding Wateroak), over 45% of the pixels were classified as disturbed within six months after the tornado outbreak and never returned to pre-tornado disturbance levels at the end of December 2013 (Fig. 4.11a) whereas NDVI is unable to provide as clear of a recovery trend. However, the quality of DI is heavily dependent on the sample size coupled with the accuracy of the land cover classification of the input imagery. Cloud cover can obscure forest pixels and portions of the damage swath, affecting both the global mean and standard deviation of the Tasseled Cap indices and summary statistics related to the disturbed pixels. This can be observed

when relaxing the cloud-free threshold from 90% (Fig. 4.11a) to 50% (Fig. 4.11b). For example, the percentage of disturbed pixels (median DI) from the Sawyerville-Eoline tornado varies from 49% (2.89) on 15 January 2012, to 16% (0.81) on 22 May 2012, and back up to 35% (1.79) on 2012 June 23. On 22 May 2012, roughly 31% of the damage swath was covered in clouds/cloud shadows, removing areas with higher DI values. Furthermore, our reliance on Landsat 7 ETM+ data with the SLC-failure reveals/removes certain parts of the tornado swath and background forest pixels within each successive image and contributes to some of the inter-image variability in DI. Applying a stricter cloud-free threshold and using an alternate satellite sensor without the SLC-failure (e.g., Landsat 8) would mitigate these artifacts.

## 4.6 Discussion & Operational Relevance

Comparing the spectral reflectance across grassland, urban, and forest land cover reveals several commonalities in how the spectral behavior changes within tornado-damaged areas. Most affected areas had a higher SR in the visible and SWIR and a lower SR in the NIR Landsat spectral bands. In most tornado and land cover combinations evaluated, the smaller difference between the NIR and visible red reflectance resulted in a decline in the median NDVI in tornado-impacted areas. These land cover independent observations coupled with the ability to calculate NDVI with relative ease supports the use of vegetation indices such as NDVI to visualize the extent of tornado damage.

In this study, we were selective in which tornado swaths were included in our case dataset. In many instances, the manual contours were smaller than the spatial extent of tornado damage due to a lack of confidence in discriminating whether or not damage had occurred due to the spatial constraints of the tornado. In an analysis of satellite-estimated lengths versus surveyed lengths of tornadoes from the 27 April 2011

outbreak, Molthan et al. (2014) measured that satellite-based lengths underestimated survey lengths by around 20 km with Landsat 7 ETM+ data and 23 km with higher-resolution ASTER data. Regardless, satellite data can aid in identifying regions of damage potentially missed or unreachable by ground-based damage surveys.

It is worth repeating that attempts to detect tornado damage are dependent on a multitude of variables. First, the ability to identify a damage signature is subject to the spatial constraints of the phenomenon observed, be it a tornado, damaging wind, or hail event. The events in this study and many prior studies (Yuan et al. 2002; Jedlovec et al. 2006; Wilkinson and Crosby 2010; Molthan et al. 2014) showed the clearest damage signal had visible scouring observed in the SR imagery and were associated with very intense tornadic circulations. But, tornadoes go through varying levels of organization throughout their lifecycle, producing inconsistent and oftentimes asymmetric damage in their wake. Holland et al. (2006) simulated how tornadoes damaged forests and found variable responses to tree-fall that were dependent on both the radial and tangential components of the vortex and subsequent forward speed. These translational variables coupled with the geographical location, health, and composition of forests will affect the extent remotely sensed imagery can detect damage. A comparable argument could be made on the dependence of building construction quality and quantity in determining the extent of tornado damage in urban areas. A second factor affecting damage identification is the scale and contribution of different land cover types in a geographic domain. Comparing urban densities, we found that high density urban areas showed a much smaller change in NDVI compared to open space urban areas. Additionally, vegetated areas collocated or downwind of an urban environment showed a different pre-tornado spectral reflectance curve and experienced amplified departures in reflectance compared to analyses of damage further away from urban environments. The displacement of debris, exposure of soil, and defoliation of trees fundamentally alters the spectral behavior of the Earth's surface; however, the exact contributions of

each factor may not be readily known with spaceborne data in the absence of ancillary data. Finally, seasonal effects in identifying tornado damage is an underexplored topic. Many prior studies and this current study have focused on the identification of spring and summer tornadoes (e.g., Yuan et al. 2002; Jedlovec et al. 2006; Molthan et al. 2014) where the frequency of tornado occurrence is higher (Brooks et al. 2003). In the case of forest damage associated with tornado Q in Marshall, MS, the only winter tornado in our study, NIR reflectance was 15% higher and red reflectance was 46% higher in the tornado damage polygon, resulting in a decline in NDVI by 0.07. The increase in the NIR spectral range was more prevalent in fall/winter events and coupled with the factors above may limit detection outside of the spring and summer.

In the immediate aftermath of a tornado, vegetation indices like NDVI can provide a cursory look at where tornado damage has occurred; however, the vegetation cycle associated with the seasons severely limits the application of comparing NDVI on a pixel-by-pixel basis across multiple images. The application of DI to identify tornado damage in forests in Section 4.4.2 highlights its resiliency to the shortfalls of NDVI by providing a seasonally independent technique to initially identify as well as track damage areas over time. With a relatively stable DI observed in the 28 months prior to the tornado outbreak, change detection studies using DI or a DI-like analog may not need a pre-event image in the same season or year to compare to a post-event image. However, a longer comparison interval opens up the potential for other sources of disturbance (e.g. wildfire, harvest, land cover change) to enter the image and be confused with tornado damage. In a similar vein to NDVI, examination of the shape and extent of the damage will assist in determining the source of the damage.

While DI is beneficial at standardizing images across time, it is similar to NDVI in terms of missing detections due to either weaker tornadoes or tornado occurrence in certain geographic areas. (Masek et al. 2008) observed diminished skill in the DI parameter from samples taken within the Rockies and Intermountain West. An optimal

initial operating condition for this iteration of DI is a dark, closed-canopy forest that minimizes the contributions from the low-level vegetation and soils from dominating the reflectance signal. This issue can be mitigated by incorporating higher-resolution maps of vegetation type and density, if available. Furthermore, DI was originally developed to identify stand-replacing clearance (i.e., complete removal of trees). In the case of tornado damage, the remnants of downed trees and their associated shadows could cover up a higher fraction of the soil background and subsequently provide a lower magnitude increase (decrease) in the Tasseled Cap brightness (wetness) values compared to clear-cut forests (Baumann et al. 2014). As such, adjustments to the forest coefficients based on the indigenous vegetation of a local geographic region along with the derivation of DI-like coefficients could provide a greater operational applicability to this index.

## 4.7 Conclusions

In the first part of this study, we explored how the spectral behavior of tornado damage varies within 17 urban, 16 forest, and ten grassland environments across the central and eastern United States using Landsat 5 TM and Landsat 7 ETM+ imagery. Overall, we found that most tornadoes exhibited higher reflectance in the visible and SWIR TM/ETM+ spectral ranges and a lower reflectance in the NIR spectral range, particularly for tornadoes evaluated during the spring and summer months. During these seasons, these spectral signatures correspond to many tornado-damaged regions having higher Tasseled Cap brightness values due to a general increase in reflectance across most Landsat bands, lower Tasseled Cap greenness values driven by the decline in NIR reflectance, and lower Tasseled Cap wetness values due to the larger increases in SWIR reflectance compared to visible reflectance. Additionally, median NDVI values were lower in tornado-damaged areas for the three land cover types except for one grassland

case. While these trends in spectral signatures, Tasseled Cap indices, and NDVI may provide some initial guidance at developing a damage identification algorithm, the extent and magnitude of tornado damage is dependent on factors related to the strength of the tornado, the type and density of land cover it passes over, and time of year.

While NDVI is beneficial at providing a cursory look at localized change caused by natural hazards, analyses of recovery using NDVI is limited to the acquisition of cloud-free, intra-season imagery. Even with these constraints, pixel-based NDVI values can vary within season due to the normal vegetation lifecycle and other external influences (e.g., drought). Part two of this study explored the applicability of using DI from Healey et al. (2005) to identify and track tornado damage in forested areas within a five-year window surrounding the 27 April 2011 tornado outbreak. Before the tornado outbreak, the median value of DI remained relatively stable compared to NDVI which increases in the spring and summer months and decreases in the fall and winter months. After the tornado outbreak, values of DI initially increased dramatically with four of the five tornadoes registering over 45% of the contoured track as disturbed (DI $\geq$ 3) within six months. The percentage of disturbed pixels declined over time as ongoing recovery occurred in the region. During recovery, NDVI values began to converge with NDVI values in the background region but continued to vary with the seasons. While the quality of the DI output is influenced by the accuracy of the land cover classification and the amount of cloud-free imagery, this seasonal resiliency should promote the usage of DI and the re-development of new DI-like indices focused on tornado damage in different land cover regions in future studies of natural hazards.

## Acknowledgements

The authors would like to thank Braden Owsley, Brandon Smith, and Sean Waugh for their assistance in a pilot study on this topic. Discussions with Kevin Man-

ross and Christopher Karstens were helpful in refining the methods used in this paper. Manuscript reviews by Andrew Molthan and one anonymous reviewer significantly improved the content and organization of this manuscript. Funding was provided by the NOAA/Office of Oceanic and Atmospheric Research under NOAA-University of Oklahoma Cooperative Agreement #NA11OAR4320072, U.S. Department of Commerce and through the NASA Interdisciplinary Science Program project NNX12AM89G as part of the grant "Storms, Forms, and Complexity of the Urban Canopy: How Land Use, Settlement Patterns, and the Shapes of Cities Influence Severe Weather." The views expressed in this paper are those of the authors and do not necessarily represent those of the NOAA, NSSL, or CIMMS.

Table 4.1: The list of tornadoes used in this study and associated information regarding time and location of occurrence, strength, length, maximum width, and Landsat image acquisition date and location.

| Tornado ID | Counties Affected | Max Damage Rating | Length (km) | Max Width (m) | Event Date | Image Date | Landsat | Path/Row |
|---|---|---|---|---|---|---|---|---|
| A | Bollinger-Madison, MO | F2 | 14.5 | 732 | 24 April 2002 | 9 May 2002 | 7 | 23/34 |
| B | Butler-Carter, MO | F4 | 66.2 | 594 | 24 April 2002 | 9 May 2002 | 7 | 23/34 |
| C | Calvert-Charles-St. Mary's, MD | F4 | 103.2 | 594 | 28 April 2002 | 1 May 2002 | 7 | 15/33 |
| D | Langlade-Menominee-Shawano-Oconto, WI | EF3 | 11.9 | 914 | 7 June 2007 | 15 June 2007 | 7 | 24/29 |
| E | Ottawa, OK & Newton, MO | EF4 | 113.5 | 1,609 | 10 May 200 | 30 May 2008 | 7 | 26/34 |
| F | Logan-Sangamon, IL | EF3 | 39.0 | 805 | 19 August 2009 | 1 September 2009 | 7 | 23/32 |
| G | Holmes-Yazoo, MS | EF4 | 90.3 | 2,816 | 24 April 2010 | 7 May 2010 | 5 | 23/37 |
| H | McNairy, TN | EF2 | 41.4 | 805 | 2 May 2010 | 8 May 2010 | 7 | 22/36 |
| I | Faulkner-Pulaski, AR | EF2 | 46.8 | 2,651 | 25 April 2011 | 17 May 2011 | 5 | 24/36 |
| J | Jasper, MO | EF5 | 32.7 | 1,463 | 22 May 2011 | 8 June 2011 | 7 | 26/34 |
| K | Franklin-Johnson-Logan, AR | EF4 | 73.6 | 2,011 | 24 May 2011 | 1 June 2011 | 7 | 25/35 |
| L | Canadian-Kingfisher-Logan, OK | EF5 | 37.8 | 1,097 | 24 May 2011 | 29 May 2011 | 5 | 28/35 |
| M | Hampden-Worcester, MA | EF3 | 60.5 | 805 | 1 June 2011 | 5 June 2011 | 5 | 13/31 |
| N | Scott-Newton, MS | EF3 | 23.1 | 805 | 18 October 2012 | 20 October 2012 | 7 | 22/38 |
| O | Cleveland-Pottawatomie, OK | EF4 | 37.0 | 1,372 | 19 May 2013 | 11 June 2013 | 7 | 28/35 |
| P | Cleveland, OK | EF5 | 22.3 | 1,737 | 20 May 2013 | 11 June 2013 | 7 | 28/35 |
| Q | Marshall, MS | EF4 | 97.8 | 1,189 | 23 December 2015 | 17 January 2016 | 7 | 22/36 |

Table 4.2: Spectral ranges of the Landsat 5 TM and Landsat 7 ETM+ visible to SWIR reflectance bands (USGS 2016).

| Band | Landsat 5 TM Spectral Range [$\mu$m] | Landsat 7 ETM+ Spectral Range [$\mu$m] | Center Wavelength [$\mu$m] |
|---|---|---|---|
| Band 1 – Visible Blue | 0.45-0.52 | 0.45-0.52 | 0.49 |
| Band 2 – Visible Green | 0.52-0.60 | 0.52-0.60 | 0.56 |
| Band 3 – Visible Red | 0.63-0.69 | 0.63-0.69 | 0.66 |
| Band 4 – NIR | 0.76-0.90 | 0.77-0.90 | 0.83 |
| Band 5 – SWIR | 1.55-1.75 | 1.55-1.75 | 1.67 |
| Band 7 – SWIR | 2.08-2.35 | 2.09-2.35 | 2.24 |

Table 4.3: Coefficients derived from Crist (1985) and applied to each Landsat 5 TM and Landsat 7 ETM+ band to generate the three Tasseled Cap parameters.

| Band/Tasseled Cap Parameter | 0.49 $\mu$m | 0.56 $\mu$m | 0.66 $\mu$m | 0.83 $\mu$m | 1.67 $\mu$m | 2.24 $\mu$m |
|---|---|---|---|---|---|---|
| Brightness | 0.2043 | 0.4158 | 0.5524 | 0.5741 | 0.3124 | 0.2303 |
| Greenness | -0.1603 | -0.2819 | -0.4934 | 0.7940 | -0.0002 | -0.1446 |
| Wetness | 0.0315 | 0.2021 | 0.310 | 0.1594 | -0.6806 | -0.6109 |

Table 4.4: The number (and percentage of track area) of urban, forest, and grassland pixels identified within each tornado damage region as defined from NLCD. Tornadoes with a low sample size for a specific land cover (N $<$ 100) were excluded from that individual land cover analysis and are marked with a (*).

| Tornado ID | Counties Affected | Urban Pixels (NLCD 21 - 24) | Forest Pixels (NLCD 41 - 43) | Grassland Pixels (NLCD 71) |
|---|---|---|---|---|
| A | Bollinger-Madison, MO | 456 (3.2%) | 11,053 (78.2%) | 874 (6.2%) |
| B | Butler-Carter, MO | 1,720 (6.7%) | 18,635 (83.8%) | 275 (1.3%) |
| C | Calvert-Charles-St. Mary's, MD | 2,855 (17.7%) | 7,657 (46.7%) | 105 (0.6%) |
| D | Langlade-Menominee-Shawano-Oconto, WI | 822 (3.3%) | 15,282 (63.4%) | 32* (0.1%) |
| E | Ottawa, OK & Newton, MO | 1,113 (7.6%) | 5,933 (42.1%) | 192 (1.1%) |
| F | Logan-Sangamon, IL | 381 (10.1%) | 44* (1.9%) | 0* (0.0%) |
| G | Holmes-Yazoo, MS | 2,728 (6.6%) | 24,101 (58.5%) | 31* (0.1%) |
| H | McNairy, TN | 572 (13.8%) | 2,068 (51.5%) | 88* (2.0%) |
| I | Faulkner-Pulaski, AR | 1,938 (7.9%) | 13,380 (54.4%) | 1,542 (6.3%) |
| J | Jasper, MO | 5,530 (94.6%) | 104 (1.8%) | 80* (1.4%) |
| K | Franklin-Johnson-Logan, AR | 903 (5.6%) | 6,198 (34.5%) | 1,992 (10.2%) |
| L | Canadian-Kingfisher-Logan, OK | 1,659 (6.5%) | 860 (3.4%) | 11,158 (43.5%) |
| M | Hampden-Worcester, MA | 2,527 (22.1%) | 15,302 (60.1%) | 35* (0.1%) |
| N | Scott-Newton, MS | 123 (4.2%) | 424 (14.7%) | 242 (8.2%) |
| O | Cleveland-Pottawatomie, OK | 1,306 (9.6%) | 6,106 (45.9%) | 3,610 (28.2%) |
| P | Cleveland, OK | 2,106 (76.9%) | 105 (3.3%) | 467 (19.0%) |
| Q | Marshall, MS | 133 (3.5%) | 2,352 (57.0%) | 16* (0.5%) |

Table 4.5: Spatial extent and percentage of forest coverage within the manually contoured damage regions inside the path 21/row 37 Landsat image. Tornado track information was assembled from information provided by the NWS Birmingham, AL office and the NWS Service Assessment from this tornado outbreak (NOAA 2011).

| Populated Area(s) Near Scour Location | Scour Area [$km^2$] | Scour Length [km] | Scour Maximum Width [m] | Forest pixels (% of total) |
|---|---|---|---|---|
| Wateroak, AL | 3.4 | 34.1 | 307 | 2,892 (77.4%) |
| Reform, AL | 3.2 | 20.3 | 650 | 2,902 (81.2%) |
| Panola-Geiger, AL | 6.1 | 21.0 | 995 | 2,763 (41.0%) |
| Sawyerville-Eoline, AL | 86.2 | 232.2 | 1,324 | 51,887 (54.2%) |
| Tuscaloosa-Birmingham, AL | 125.8 | 258.6 | 2,307 | 77,079 (55.2%) |

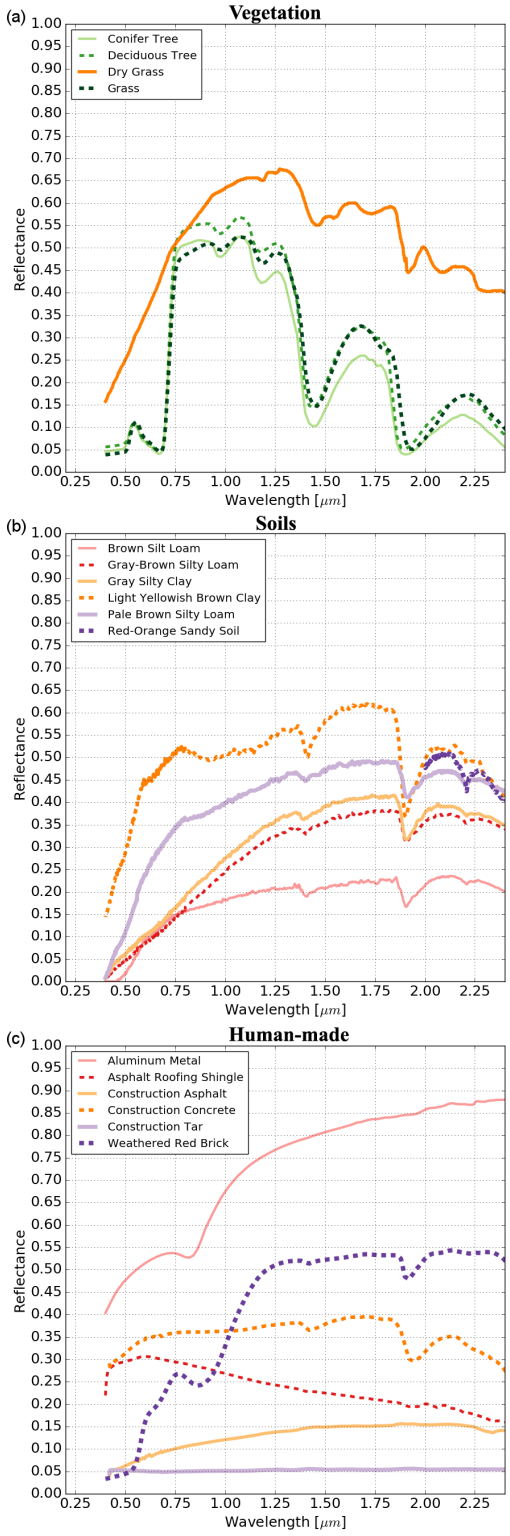


Figure 4.1: Spectral reflectance curves of different (a) vegetation, (b) soils, and (c) human-made materials from the Advanced Spaceborne Thermal Emission and Reflection Radiometer (ASTER) Spectral Library (Baldridge et al. 2009).

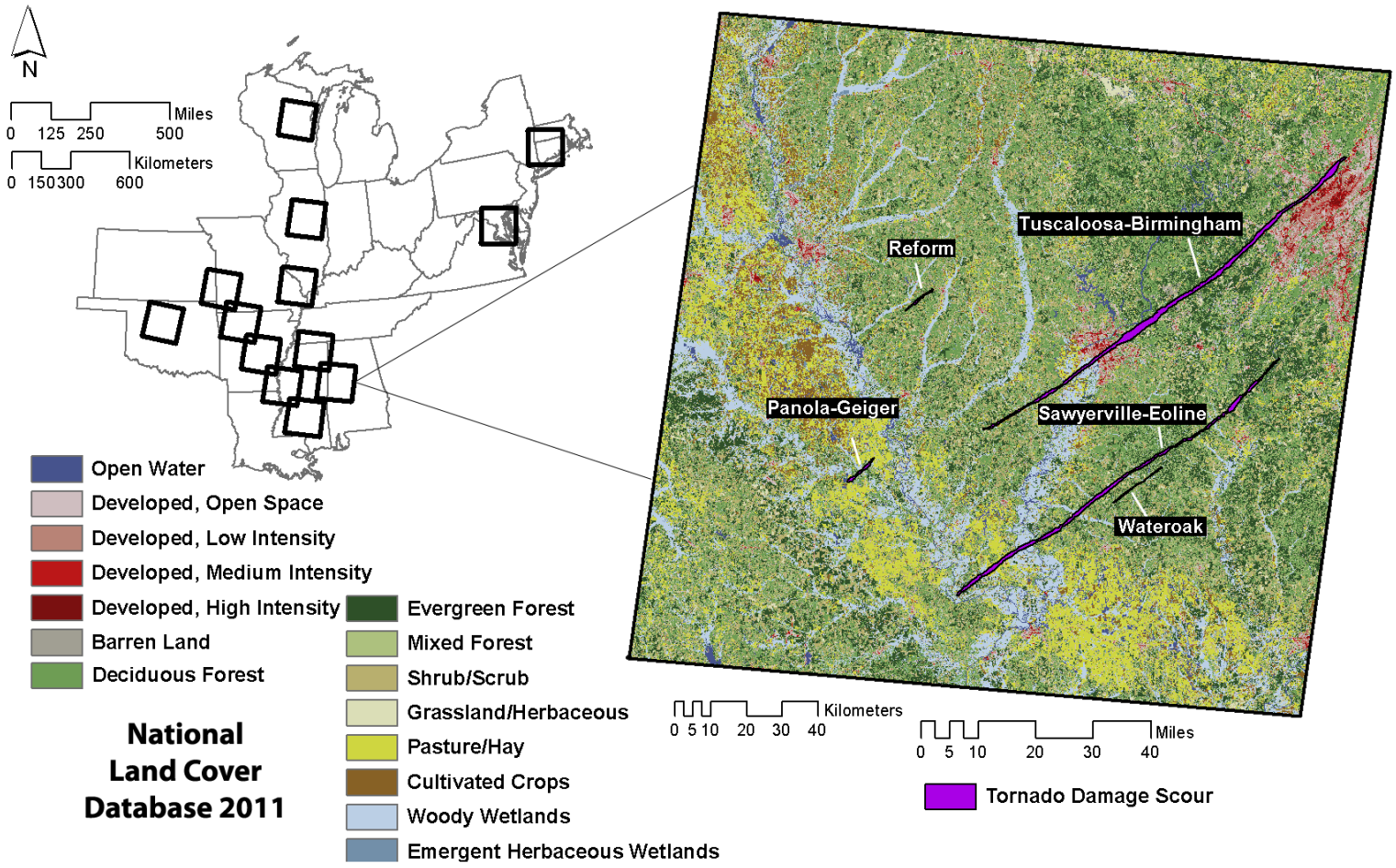


Figure 4.2: Landsat imagery locations used in part one of this study are shown on the map in the upper-left corner of this figure. Extending from the domain map is a land cover map with contoured locations of tornado damage (purple polygons) within the Landsat domain (path 21/row 37) used for part two of this study.

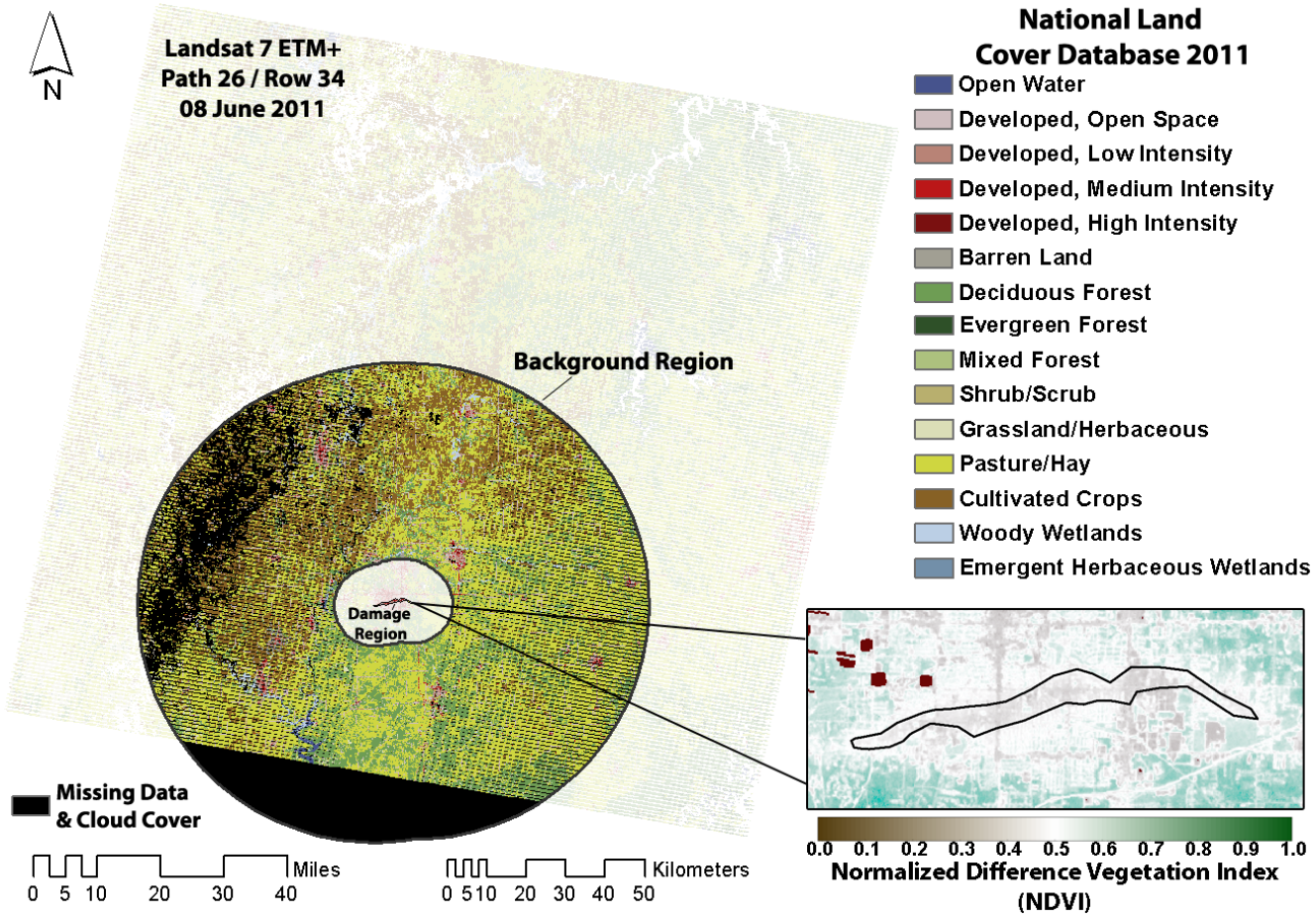


Figure 4.3: An example of the damage and background domains identified for the Jasper County, MO tornado occurring on 22 May 2011. The calculation of NDVI (bottom-right) was one of several image enhancement techniques used to define the spatial extent of damage beyond what is provided within the Storm Data record.

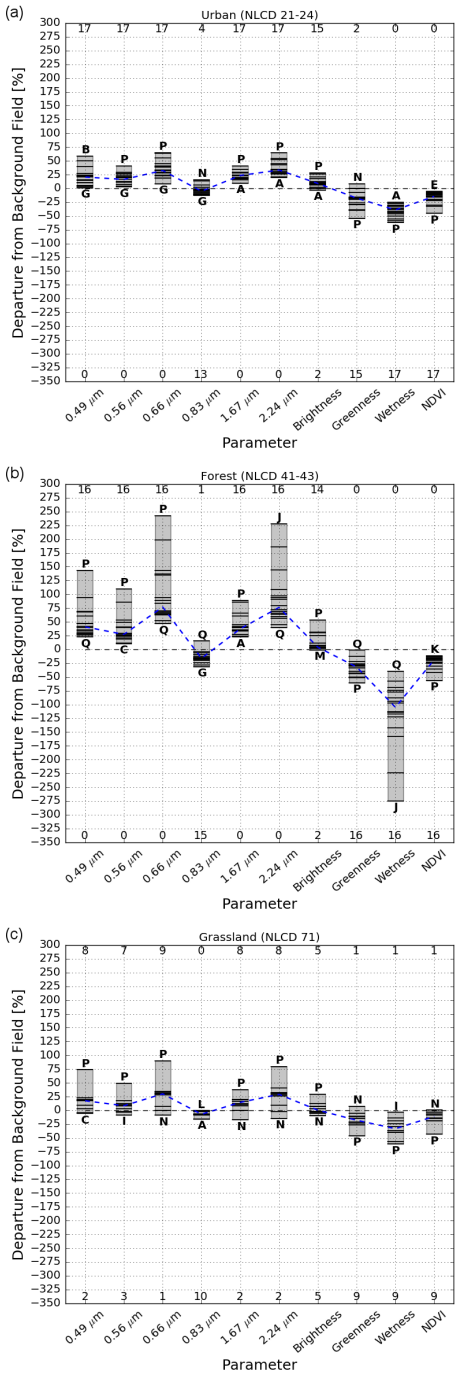


Figure 4.4: Percent departure in median reflectance, Tasseled Cap indices, and NDVI from the background region for (a) urban, (b) forest, and (c) grassland land cover. Each horizontal black line indicates an individual tornado track with the gray bar corresponding to the data range. The highest and lowest departures have their respective tornado letter listed. The number of cases with positive (top) and negative (bottom) differences are listed in black. The median difference observed across all tornado tracks is highlighted by the dashed blue line.

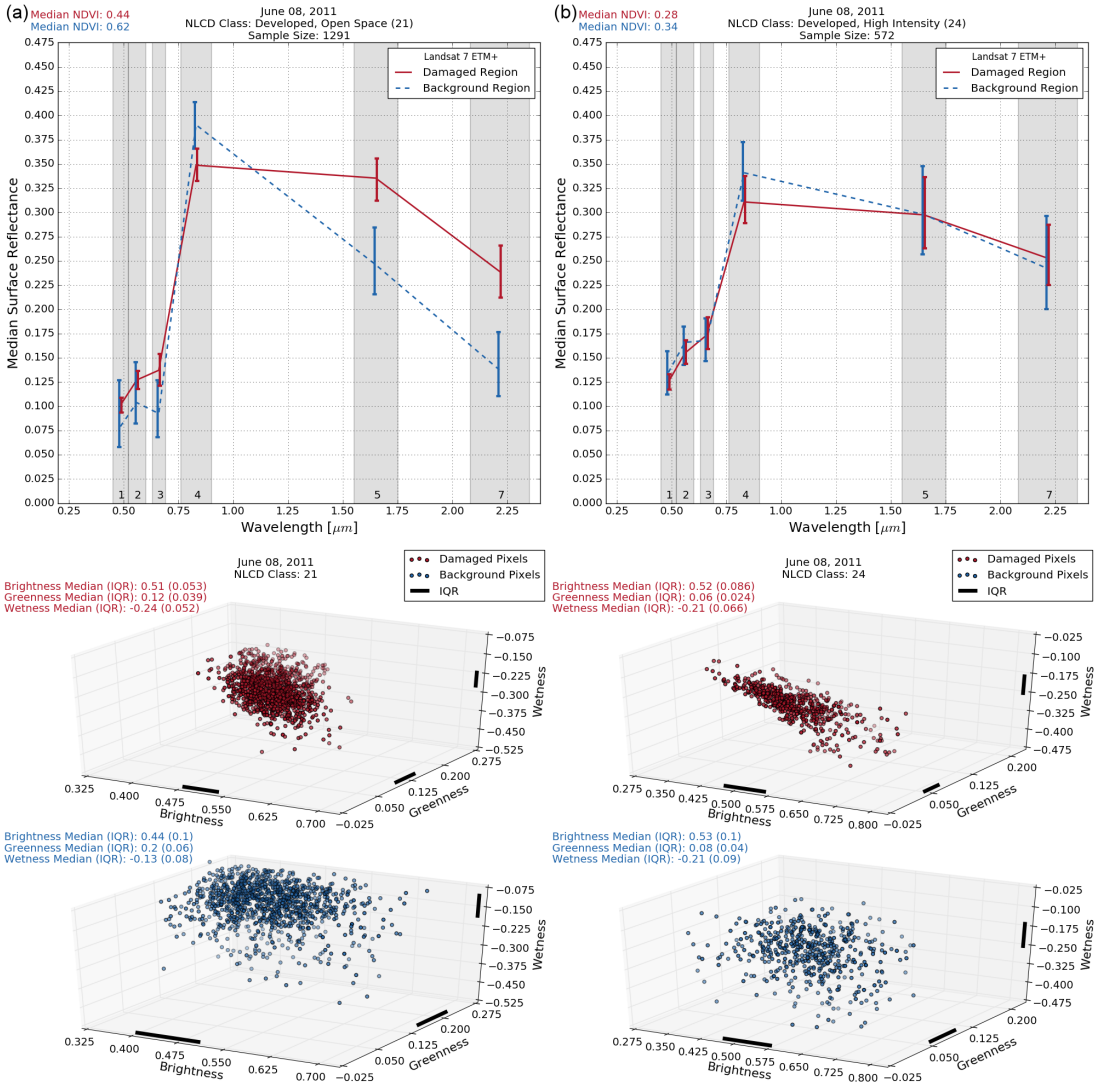


Figure 4.5: Median spectral reflectance and Tasseled Cap parameters for (a) open space and (b) high intensity urban land cover pixels classified as damaged (red) or background (blue) for the Jasper, MO tornado (tornado J). The vertical lines in the spectral reflectance plots correspond to the interquartile range.

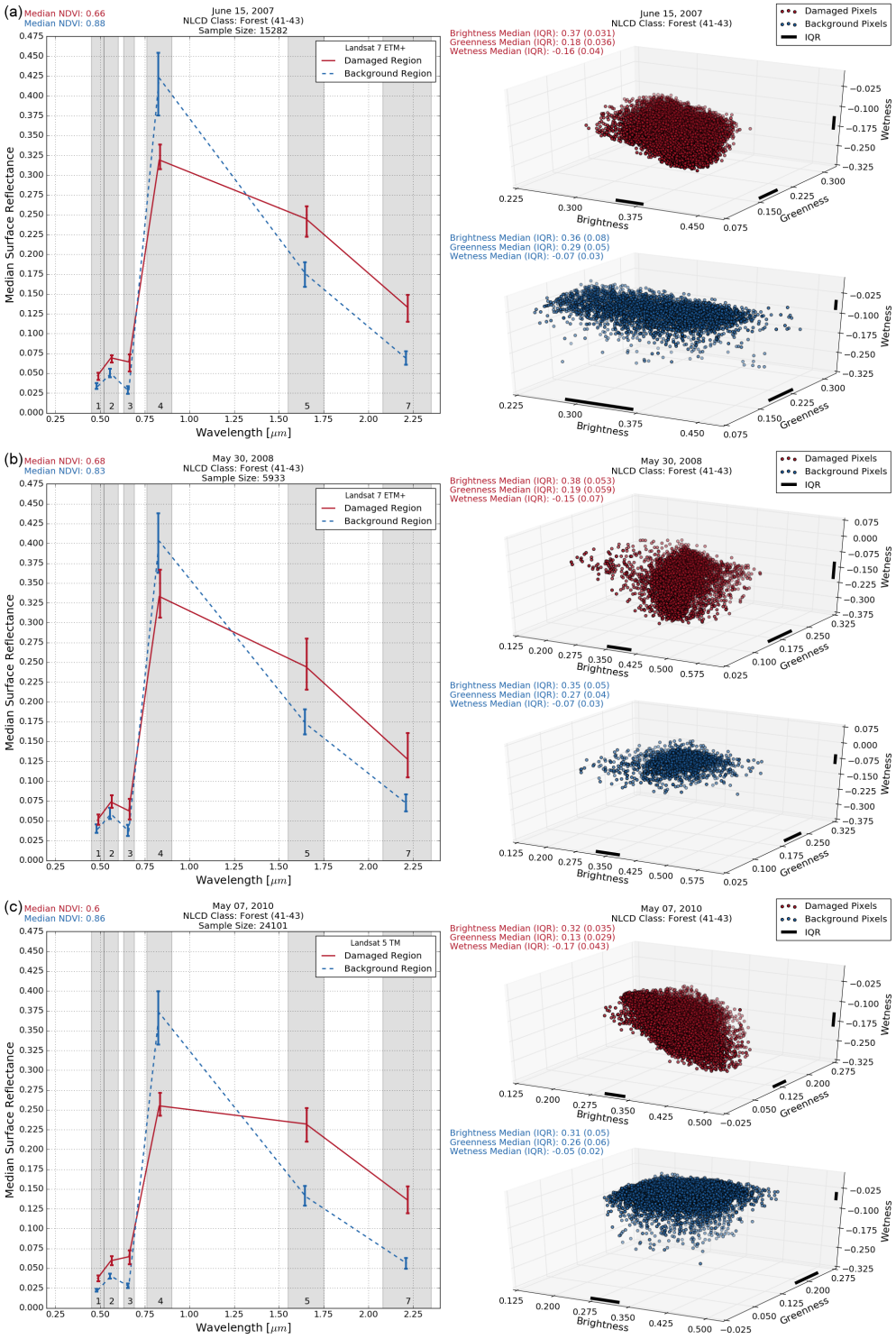


Figure 4.6: Median spectral reflectance and Tasseled Cap parameters for (a) tornado D in Langlade-Menominee-Shawano-Oconto, WI, (b) tornado E in Ottawa, OK and Newton, MO, and (c) tornado G in Holmes-Yazoo, MS. The vertical lines in the spectral reflectance plots correspond to the interquartile range.

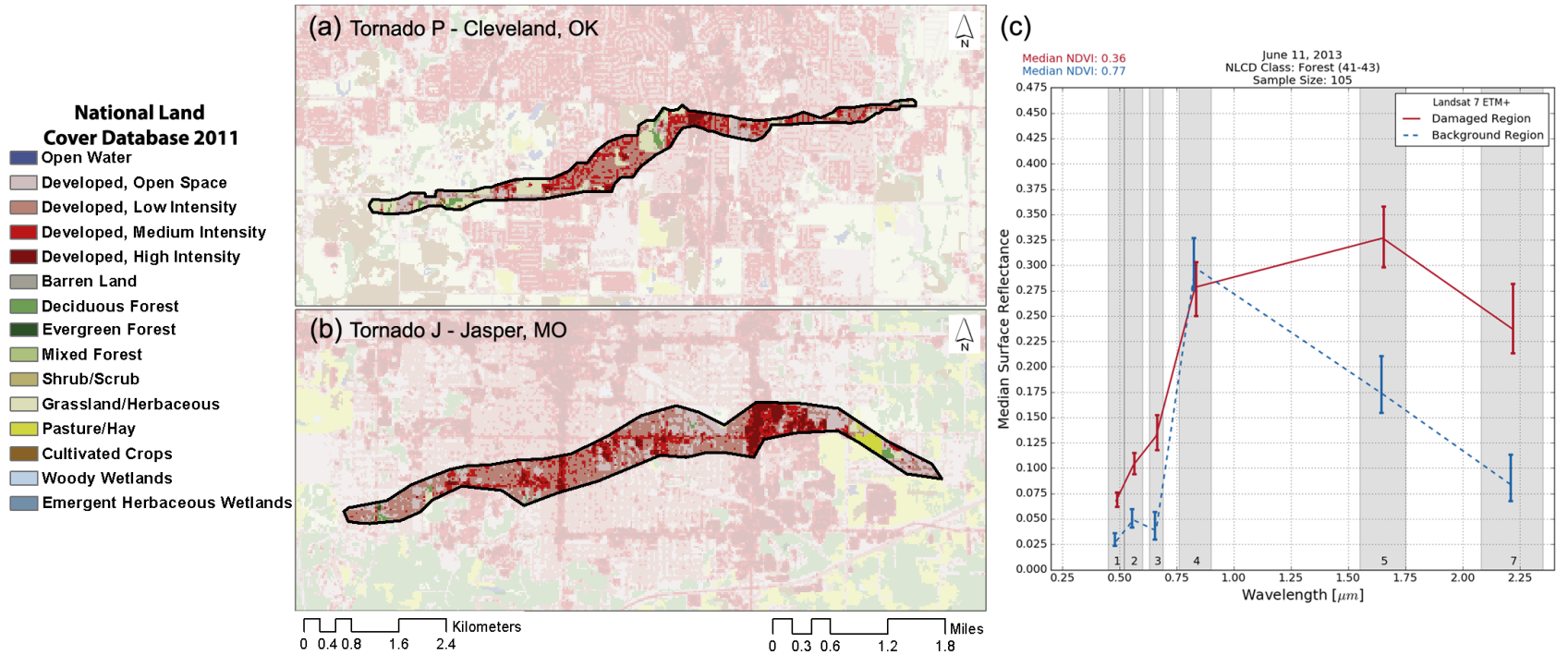


Figure 4.7: Maps of land cover type within the damage contour (black polygon) for (a) tornado P affecting Cleveland, OK on 20 May 2013 and (b) tornado J affecting Jasper, MO on 22 May 2011. (c) The spectral reflectance curve associated with tornado P from Landsat 7 ETM+ SR imagery acquired on 11 June 2013.

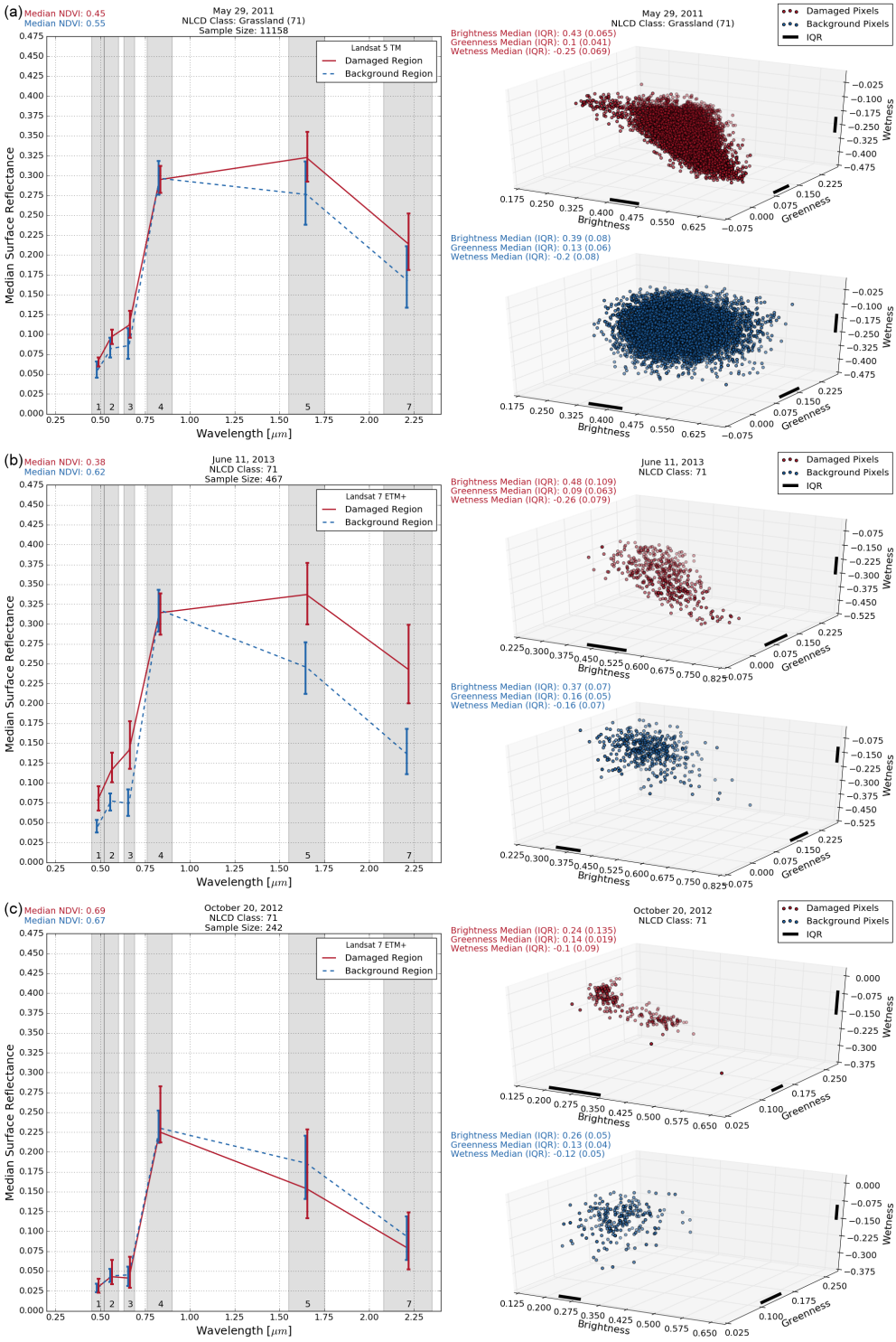


Figure 4.8: Median spectral reflectance and Tasseled Cap parameters for (a) tornado L in Canadian-Kingfisher-Logan, OK (b) tornado P in Cleveland, OK, and (c) tornado N in Scott-Newton, MS. The vertical lines in the spectral reflectance plots correspond to the interquartile range.

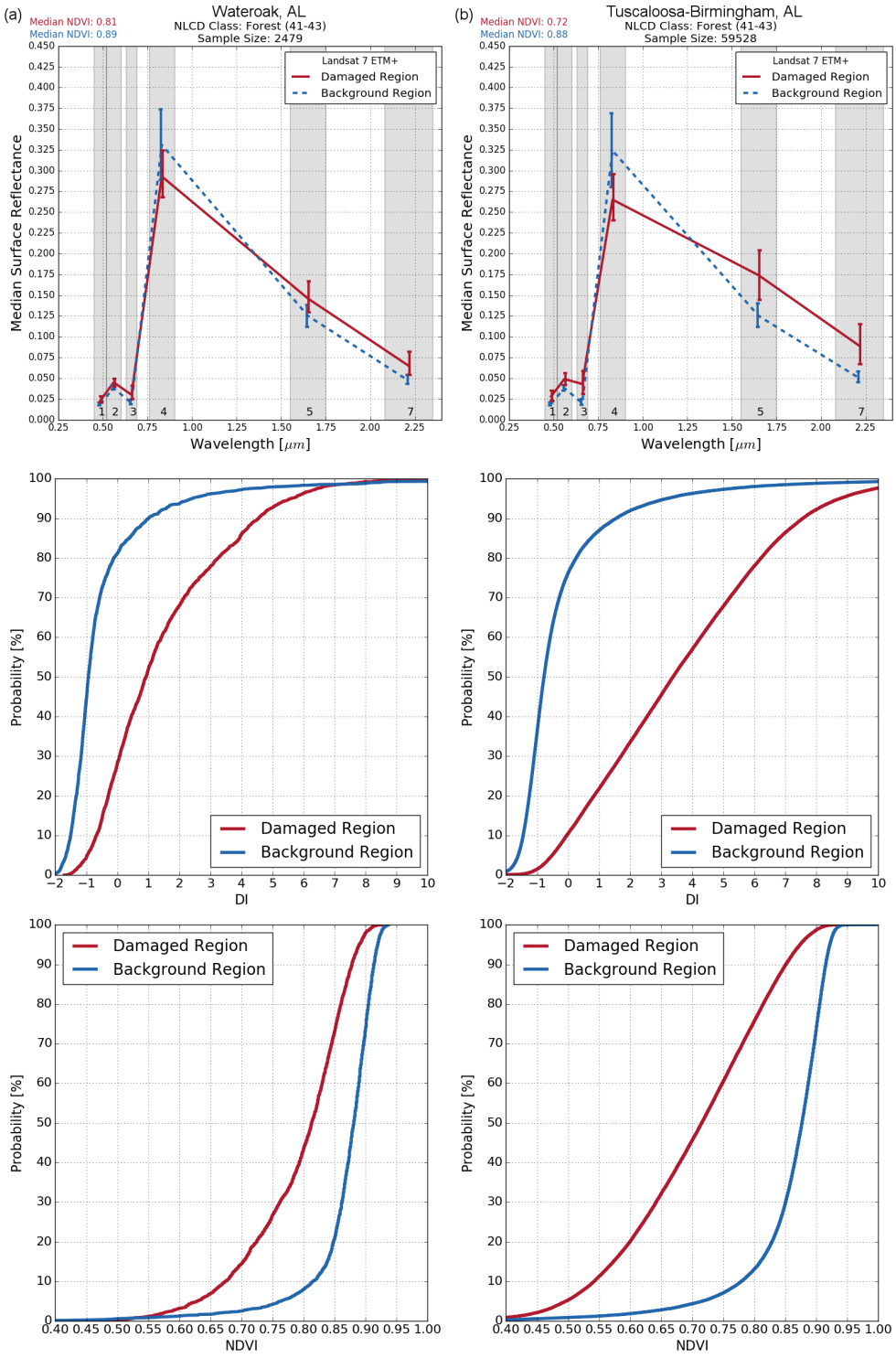


Figure 4.9: Damaged (red lines) and background (blue lines) spectral reflectance curves (top row) and CDF plots of DI (middle row) and NDVI (bottom row) for the (a) Wateroak, AL and (b) Tuscaloosa-Birmingham, AL tornadoes on 27 April 2011.

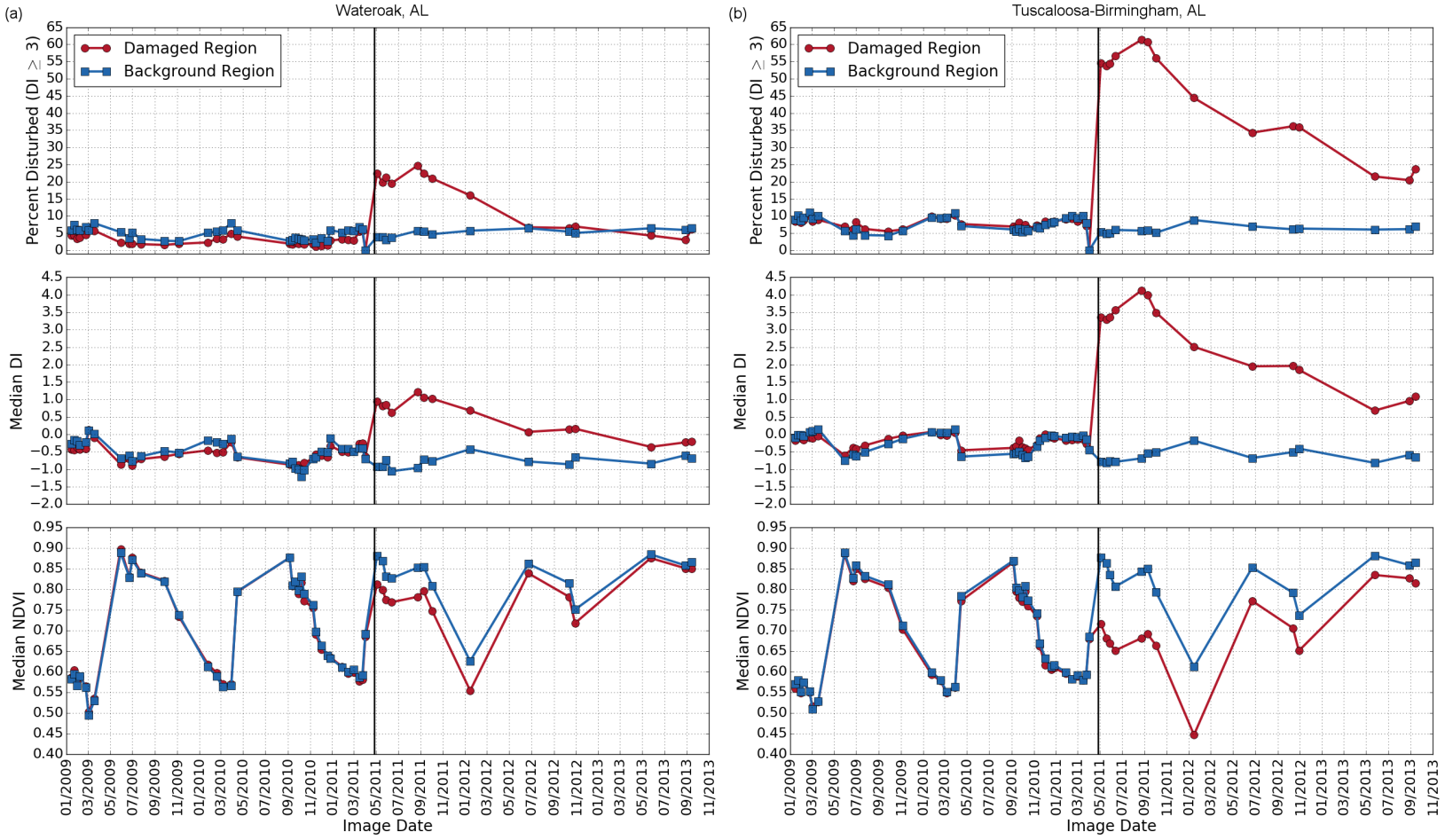


Figure 4.10: Damaged (red lines) and background (blue lines) spectral reflectance curves (top row) and CDF plots of DI (middle row) and NDVI (bottom row) for the (a) Wateroak, AL and (b) Tuscaloosa-Birmingham, AL tornadoes on 27 April 2011.

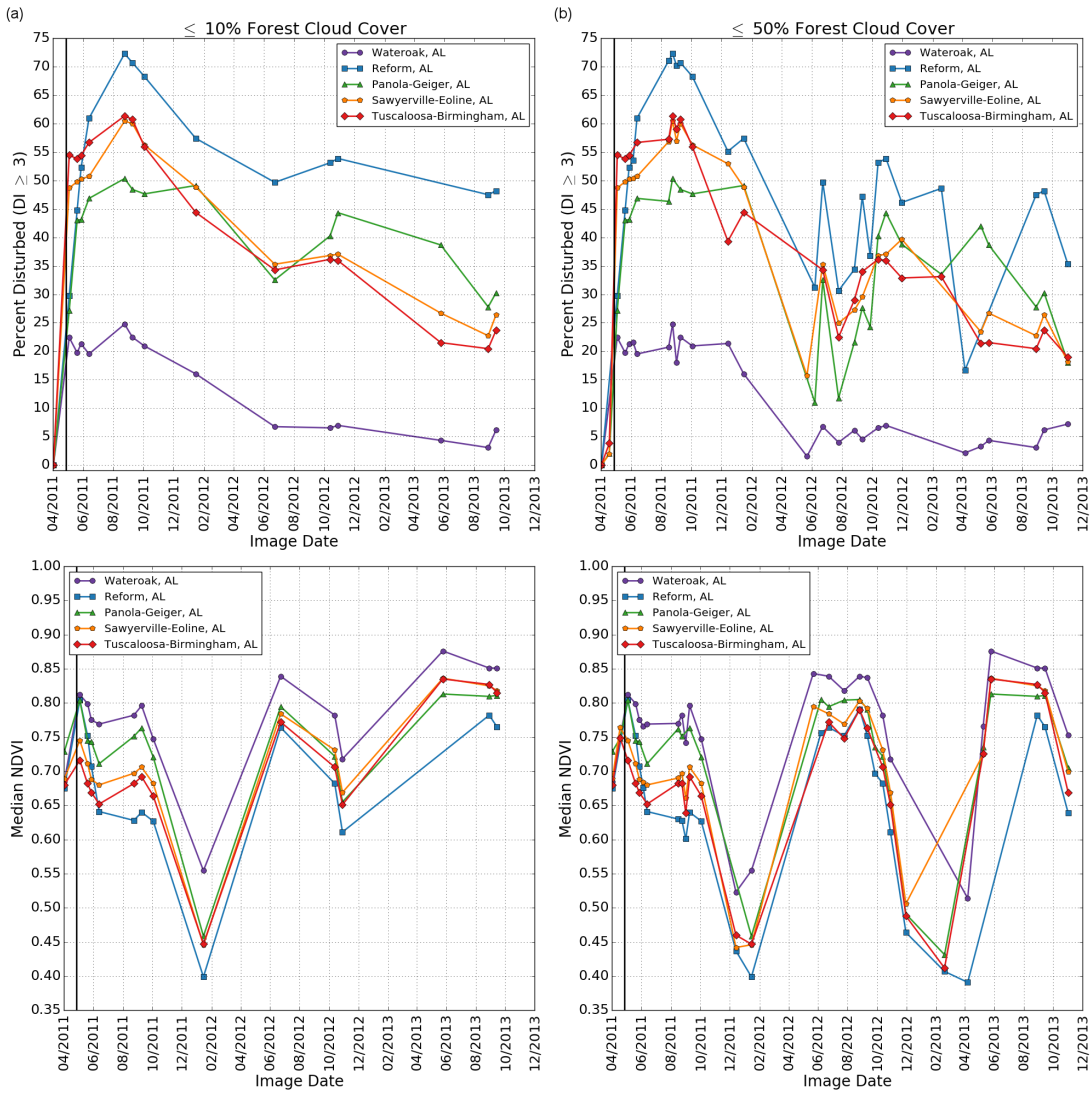


Figure 4.11: Time-series of the percentage of disturbed pixels (top row) and median NDVI (bottom row) within each of the five damage scour regions using two cloud-cover thresholds, (a) $\leq 10\%$ and (b) $\leq 50\%$.

# Chapter 5

# Summary & Future Research Endeavors

By continuing to alter Earth's landscape to accommodate the needs of our civilization, we will also endure the resulting feedbacks on the earth-environment system that manifests in a multitude of ways. Many of these feedbacks are meteorological in nature with shifts in temperature and rainfall being two commonly researched variables. Measurements of our land and atmosphere with remote sensing instruments will continue to report in an absolute space, blind to these complex relationships. As shown in these three chapters with a research emphasis on thunderstorms and their attendant hazards, prerequisite knowledge of land use and land cover information can aid in the identification and interpretation of these phenomena within climatological retrospectives of remotely sensed data.

Chapter 2 is the first known contiguous United States (CONUS) retrospective using 20-years of National Lightning Detection Network (NLDN) cloud-to-ground (CG) lightning data at 500 m spatial resolution. This analysis revealed geographical and seasonal differences in lightning characteristics such as peak current and polarity closer and further away from antenna towers. At 500 m spatial resolution, all grid cells with $>$ 105 CGs had a tower registered with the Federal Communications Commissions (FCC) located within 1 km of each cell centroid. 96% of towers isolated by 10 km from another tower had a higher CG lightning density within 1 km of a tower location compared to 2 – 5 km away. Lightning occurrence was correlated to tower height, with taller towers experiencing a higher frequency of strikes compared to their surround-

ings. Furthermore, CGs near towers were more likely to transfer negative charges at a higher peak current than locations further away, validating prior research on how the NLDN registers certain tower-induced lightning strikes. Towers in the northern Great Plains were more visible in CG lightning maps due to a generally lower thunderstorm occurrence within this region compared to parts of the southeastern United States. As the northern United States is prone to experiencing convective regimes in both the cool and warm seasons, an interesting result is that a higher percentage of total towers experienced a four-fold increase in CG lightning density in the cold season months (September – February) compared to the warm season months (March – August). The shortest tower experiencing an increase of this magnitude was roughly 343 m in the cold season compared to 457 m in the warm season. This is expected, but never formally quantified on the scale employed in this study, as charging mechanisms in winter storms tend to be closer to the ground due to shallower convective structures and colder vertical temperature profiles compared to warm season events. Finally, a majority of new tower construction projects have immediate effects on the frequency of CG lightning in the following year. These new lightning hot spots can artificially inflate gridded frequencies in coarser CG retrospectives, overestimating lightning risk maps used in the development of new infrastructure or insurance estimation (e.g., Correa-Henao et al. 2013).

This study lays the groundwork for future research endeavors by quantifying the scale of these tower-induced phenomena. Elevated CG frequencies were observed near towers in 42 of the 48 states evaluated, providing opportunities for local research groups to add supplemental instrumentation and study additional lightning characteristics, such as the direction of initiation, that are not as discernible via NLDN. Another avenue of exploration is the integration of Lightning Mapping Array (LMA; Rison et al. 1999) information. While the NLDN provides an estimated location of a CG strike on the ground, LMAs provide a three-dimensional map of lightning chan-

nel segments within 100 km of the network center. One lightning flash can contain thousands of individual segments and these segments can be stitched together to determine the direction of movement and altitude of both CG and intracloud (IC) lightning. Currently, there are LMA networks in northern Colorado, New Mexico, central Oklahoma extending into west Texas, southeast Texas around Houston, northern Alabama, north-central Georgia around Atlanta, and around the Washington D.C. area. Future small-scale analyses of tower-triggered lightning with LMAs can address the following questions. First, what is the ratio of upward to downward strikes on towers and does tower height change this ratio? Second, for upward lightning on towers, what is the ratio of self-initiated upward strikes compared to strikes caused by a preceding flash? Finally, if a tower is prematurely inducing lightning and temporarily stabilizing the electric field within a thunderstorm, are there shielding effects from CG lightning downwind of the tower? This final question could also integrate Doppler radar using the techniques explained in Chapter 3 to determine the thunderstorm motion vector as well as delineate certain horizontal and vertical attributes of each lightning-producing thunderstorm to examine if there are morphological differences in storms producing tower-triggered lightning compared to storms that do not produce such lightning.

Chapter 3 examined the effects of city size on augmenting thunderstorms through a five-year, all season climatology covering four cities of variable size in the United States Great Plains: Dallas/Fort-Worth, TX (DFW), Oklahoma City, OK (OKC), Omaha, NE (OAX), and Minneapolis/St. Paul, MN (MSP). The study undertaken in this chapter is unique from the wealth of past literature in three main aspects. First, it is the inaugural study using the multiple-radar multiple-sensor (MRMS) framework, blending over 7.1 million volumes of data from 19 Weather Service Radar – 1988 Doppler (WSR-88D) sites, 39.6 million CG lightning detections from the NLDN, and over 46,000 hours of Rapid Update Cycle/Rapid Refresh hourly analysis data into a 3D cube comprised of 33 vertical levels from 0.5 to 20 km above ground level (AGL)

at 0.01° spatial resolution and 1-min. temporal resolution. Whereas previous studies using radar focused on the maximum reflectivity at its standard update time (~5 min.) and resolution (e.g., 2 – 4 km) (e.g, Ashley et al. 2012; Haberlie et al. 2015), this study allowed for the co-examination of vertically-derived radar parameters every minute at around 1 km spatial resolution. The techniques outlined in this chapter can be replicated as research versions of the algorithms are available, allowing future endeavors to extend upon this work using other radar fields (i.e., isothermal reflectivity, echo tops) and investigating other cities. Second, this study used an automated tracking system that focused on storms moving over the urban environment and defines upwind/downwind regions on a case-by-case basis. Other notable retrospectives report results within a fixed upwind/downwind sector (e.g., 25 – 75 km west/east of a city) which is highly dependent on the prevailing flow of a majority of thunderstorms overlapping a specific geographical area (e.g., Burian and Shepherd 2005; Diem and Mote 2005). Furthermore, many studies use remote sensing systems that do not have the temporal resolution to do event-specific analyses (i.e., satellite, rain gauges), introducing uncertainty as to the extent storms on a specific day interacted with the urban environment (e.g., Kishtawal et al. 2010; Zhang et al. 2014). Third and finally, this study reports on both the entire retrospective of data in addition to a seasonal and synoptic subset of days historically shown to be most conducive for urban modification of thunderstorms. This allows for the quantification of how many thunderstorms are available for potential modification using temporal and synoptic thresholds historically used in the literature.

The results of this chapter indicate that the size of a city can influence the rate of thunderstorm initiation as well as thunderstorm strength downwind of that city given the appropriate ingredients are available. In an examination of all thunderstorm events across all seasons, the area upwind of all cities tended to have a higher thunderstorm occurrence, resulting in a higher areal mean composite reflectivity, maxi-

mum expected size of hail (MESH), and vertically integrated liquid (VIL). Segmenting the retrospective to only examine summertime thunderstorms that initiate in the afternoon/early evening hours on synoptically-benign days and produce non-supercell convective modes reveals that both DFW and MSP, the two larger cities evaluated ($> 1100$ km$^2$ in area), saw increased thunderstorm occurrence and higher magnitude radar signatures at several downwind range intervals. These patterns were not observed around OKC and OAX, roughly 40% and 26% the area of MSP. This is indicative of the potential for cities of some minimum size and their associated environmental influences (i.e., surface roughness, aerosol loading, increased urban-rural temperature gradient) to increase thunderstorm potential and severity. However, the conditions chosen to replicate conducive environments for urban modification reduced the number of thunderstorm events by 84% to 94%, shining a light on the limited occurrence of such conditions in the bigger perspective of thunderstorm occurrence.

Given the flexibility the MRMS framework provides in terms of spatiotemporal resolution and product generation, I am hopeful that future studies will leverage this powerful framework in urban meteorology endeavors. One avenue ripe for exploration is the integration of polarimetric radar fields (e.g., Kumjian 2013), available across the WSR-88D network in May 2013, to diagnose the size and type of precipitation occurring over and downwind of urban areas. In addition, the role of urban-induced aerosols on the production of precipitation and lighting has received considerable attention in the last decade (van den Heever and Cotton 2007; Rose et al. 2008; Fan et al. 2016). Many studies have previously assessed these impacts using numerical models or polar-orbiting satellites like the Tropical Rainfall Measuring Mission or the Moderate Resolution Imaging Spectroradiometer. The recent launch of the Geostationary Operational Environmental Satellite – R series in November 2016 puts the 16-channel Advanced Baseline Imager (ABI; Schmit et al. 2005) into orbit. The ABI has three times the number of spectral bands and provides data at four times the spatial resolution and five

times the temporal resolution. This sensor system could be used to estimate aerosol optical depths on an event-by-event basis as a precursor to MRMS-derived fields of precipitation and lightning.

Chapter 4 represented the largest, most geographically diverse analysis of tornado damage using multispectral satellite imagery to date. Furthermore, it is the first study to report and describe changes in the spectral response of urban, grassland, and forest land cover at various spectral ranges in the visible, near-infrared (NIR), and shortwave infrared (SWIR) portions of the electromagnetic spectrum in addition to vegetation indices and tasseled cap indices commonly reported in the past literature. Finally, it is the first reported application of a tasseled-cap based disturbance index (DI) to identify initial tornado damage and quantify recovery in forests.

Independent of geographic region and land cover type, most tornado damaged surfaces had a higher reflectance in both the visible and SWIR and a lower reflectance in the NIR spectral ranges defined within the Landsat-5 Thematic Mapper (TM) and Landsat-7 Enhanced Thematic Mapper Plus (ETM+). The changes in these individual Landsat bands corresponded to an increase in tasseled cap brightness and decreases in tasseled cap greenness and wetness as well as a decrease in the normalized difference vegetation index (NDVI). These changes were most apparent in regions with wide areas of homogeneous forest cover. Low-density urban areas tend to have more vegetated land cover collocated with it, providing an analogous signature to forest damage after a tornado. Higher-density urban areas naturally have an elevated surface reflectance in both the visible and SWIR regions, resulting in negligible shifts in these spectral regions after a tornado and lower amplitude shifts in tasseled cap and NDVI indices. Grasslands, unlike urban and forest land cover, are more susceptible to external influences (i.e., drought, land management practices) which can hinder the identification of damage. In the tornadoes selected for this study, ground scouring resulted in the complete removal of vegetation, revealing the soil background and providing a similar

spectral behavior to forest clearing.

Tasseled cap analyses of tornado-damaged forests revealed swaths of increased brightness and decreased greenness and wetness, a similar signal observed to clear-cut forests and a foundational assumption of the DI equation. The damage, however, has to be significant as the remnants of downed trees could cast shadows and continue to mask the soil background, resulting in a lower-magnitude shift in both brightness and wetness. When applied to five-years of Landsat imagery surrounding the 27 April 2011 tornado outbreak, DI-values of forests remained relatively stable around zero before the outbreak, sharply rose after the tornado outbreak, and declined gradually coincident with vegetation recovery. While NDVI, a commonly-used tornado damage identification metric, can provide a cursory look at where damage occurred, unaffected NDVI values fluctuate across the year coincident with the seasonal vegetation cycle. This limits a pixel-based, intra-season longitudinal assessment of damage recovery.

Since the initial submission of this work, both the Landsat-8 Operational Land Imager (OLI; Irons et al. 2012) and the Sentinel-2 Multispectral Imager (MSI; Drusch et al. 2012) are in orbit. Both of these sensors provide a wider spectral range of observations compared to the TM/ETM+ systems and equal or higher spatial resolution (down to 10 m using some bands of the MSI). Future research endeavors can use these improved sensor systems to examine changes in surface reflectance in identifying tornadoes of variable size as well as other thunderstorm hazards such as hail streaks. Given that cloud-cover can be detrimental for data collection using passive remote sensors, active remote sensors, such as the C-band Synthetic Aperture Radar (CSAR; Torres et al. 2012) on-board Sentinel-1 provides an all-weather, day-and-night look at land surfaces. This is a lacuna for new research to determine its utility in providing supplemental information in support of damage identification and cleanup efforts.

The identified remote sensing systems available to extend upon any of the three chapters above highlights an impetus to continue to view the world through an in-

creasingly magnified lens. By embracing technological advancements, geographers have been able to identify more complex and non-linear spatial patterns than even the brightest minds could fathom half a century ago (Sui and Morrill 2004). As a result, it is imperative for future geographers to leverage these systems in conjunction with other methods and academic disciplines to decode the fingerprint of humanity on Earth. Only through recognition of a potential problem can we begin to mitigate its negative effects, from city planning to disaster resiliency.

# References


Adler, R. F., and D. D. Fenn, 1979: Thunderstorm Intensity as Determined from Satellite Data. *Journal of Applied Meteorology*, **18**, 502–517, doi:10.1175/1520-0450(1979)018<0502:TIADFS>2.0.CO;2.

American Meteorological Society, 2017: Thunderstorm. *Glossary of Meteorology*, URL http://glossary.ametsoc.org/wiki/Thunderstorm.

Anderson, J. R., E. E. Hardy, J. T. Roach, and R. E. Witmer, 1976: A land use and land cover classification system for use with remote sensor data. U.S. Geological Survey Professional Paper 964, United States Geological Survey, 41 pp. URL http://pubs.er.usgs.gov/publication/pp964.

Angel, S., J. Parent, D. L. Civco, A. Blei, and D. Potere, 2011: The dimensions of global urban expansion: Estimates and projections for all countries, 2000–2050. *Progress in Planning*, **75**, 53–107, doi:10.1016/j.progress.2011.04.001.

Antrop, M., 2000: Geography and landscape science. *Belgeo*, **1-2-3-4**, 9–36, doi:10.4000/belgeo.13975.

Arnfield, A. J., 2003: Two decades of urban climate research: a review of turbulence, exchanges of energy and water, and the urban heat island. *International Journal of Climatology*, **23**, 1–26, doi:10.1002/joc.859.

Ashley, W. A., 2007: Spatial and Temporal Analysis of Tornado Fatalities in the United States: 1880–2005. *Weather and Forecasting*, **22**, 1214–1228, doi:10.1175/2007WAF2007004.1.

Ashley, W. A., M. L. Bentley, and J. A. Stallins, 2012: Urban-induced thunderstorm modification in the Southeast United States. *Climatic Change*, **113**, 481–498, doi:10.1007/s10584-011-0324-1.

Atkinson, B. W., 1971: The Effect of an Urban Area on the Precipitation from a Moving Thunderstorm. *Journal of Applied Meteorology*, **10**, 47–55, doi:10.1175/1520-0450(1971)010<0047:TEOAUA>2.0.CO;2.

Atlas, D., 1963: *Radar Analysis of Severe Storms*, 177–223. American Meteorological Society, Boston, MA, doi:10.1007/978-1-940033-56-3_10.

Azadifar, M., and Coauthors, 2016: Evaluation of the performance characteristics of the European Lightning Detection Network EUCLID in the Alps region

for upward negative flashes using direct measurements at the instrumented Säntis Tower. *Journal of Geophysical Research: Atmospheres*, **121**, 595–606, doi: 10.1002/2015JD024259.

Baldridge, A. M., S. J. Hook, C. I. Grove, and G. Rivera, 2009: The ASTER spectral library version 2.0. *Remote Sensing of Environment*, **113**, 711–715, doi:10.1016/j.rse.2008.11.007.

Bannari, A., D. Morin, F. Bonn, and A. R. Huete, 1995: A Review of Vegetation Indices. *Remote Sensing Reviews*, **13**, 95–120, doi:10.1080/02757259509532298.

Baumann, M., M. Ozdogan, P. T. Wolter, A. Krylov, N. Vladimirova, and V. C. Radeloff, 2014: Landsat remote sensing of forest windfall disturbance. *Remote Sensing of Environment*, **143**, 171–179, doi:10.1016/j.rse.2013.12.020.

Benjamin, S. G., and Coauthors, 2004: An Hourly Assimilation–Forecast Cycle: The RUC. *Monthly Weather Review*, **132**, 495–518, doi:10.1175/1520-0493(2004)132<0495:AHACTR>2.0.CO;2.

Benjamin, S. G., and Coauthors, 2016: A North American Hourly Assimilation and Model Forecast Cycle: The Rapid Refresh. *Monthly Weather Review*, **144**, 1669–1694, doi:10.1175/MWR-D-15-0242.1.

Bent, A. E., 1946: Radar Detection of Precipitation. *Journal of Meteorology*, **3**, 78–84, doi:10.1175/1520-0469(1946)003<0078:RDOP>2.0.CO;2.

Bentley, M. L., W. S. Ashley, and J. A. Stallins, 2010: Climatological radar delineation of urban convection for Atlanta, Georgia. *International Journal of Climatology*, **30**, 1589–1594, doi:10.1002/joc.2020.

Bentley, M. L., T. L. Mote, and P. Thebpanya, 2002: Using Landsat to Identify Thunderstorm Damage in Agricultural Regions. *Bulletin of the American Meteorological Society*, **83**, 363–376, doi:10.1175/1520-0477(2002)083<0283:ULTITD>2.3.CO;2.

Berger, K., and E. Vogelsanger, 1969: New results of lightning observations. *Planetary Electrodynamics*, S. C. Coroniti, and J. Hughes, Eds., Vol. 1, Gordon and Breach, 489–510.

Biagi, C. J., K. L. Cummins, K. E. Kehoe, and E. P. Krider, 2007: National Lightning Detection Network (NLDN) performance in southern Arizona, Texas, and Oklahoma in 2003–2004. *Journal of Geophysical Research: Atmospheres*, **112**, D05 208, doi:10.1029/2006JD007341.

Bishop, C. M., 2006: *Pattern Recognition and Machine Learning*. Springer Science, 738 pp.

Boccippio, D. J., K. L. Cummins, H. J. Christian, and S. J. Goodman, 2001: Combined Satellite- and Surface-Based Estimation of the Intracloud–Cloud-to-Ground Lightning Ratio over the Continental United States. *Monthly Weather Review*, **129**, 108–122, doi:10.1175/1520-0493(2001)129<0108:CSASBE>2.0.CO;2.

Bonan, G. B., 2001: Observational Evidence for Reduction of Daily Maximum Temperature by Croplands in the Midwest United States. *Journal of Climate*, **14**, 2430–2442, doi:10.1175/1520-0442(2001)014<2430:OEFROD>2.0.CO;2.

Bornstein, R., and Q. Lin, 2000: Urban heat islands and summertime convective thunderstorms in Atlanta: three case studies. *Atmospheric Environment*, **34**, 507–516, doi:10.1016/S1352-2310(99)00374-X.

Bornstein, R. D., and M. LeRoy, 1990: Urban barrier effects on convective and frontal thunderstorms. *Fourth Conf. on Mesoscale Processes*, American Meteorological Society, Boulder, Colorado, USA, 120–121.

Boucher, R. J., 1967: Relationships Between the Size of Satellite-Observed Cirrus Shields and the Severity of Thunderstorm Complexes. *Journal of Applied Meteorology*, **6**, 564–572, doi:10.1175/1520-0450(1967)006<0564:RBTSOS>2.0.CO;2.

Boussaton, M., S. Soula, and S. Coquillat, 2007: Total lightning activity in thunderstorms over Paris. *Atmospheric Research*, **84**, 221–232, doi:10.1016/j.atmosres.2006.07.003.

Brooks, H. E., C. A. Doswell III, and M. P. Kay, 2003: Climatological Estimates of Local Daily Tornado Probability for the United States. *Weather and Forecasting*, **18**, 626–640, doi:10.1175/1520-0434(2003)018<0626:CEOLDT>2.0.CO;2.

Brown, R. A., W. C. Bumgarner, K. C. Crawford, and D. Sirmans, 1971: Preliminary Doppler Velocity Measurements in a Developing Radar Hook Echo. *Bulletin of the American Meteorological Society*, **52**, 1186–1188, doi:10.1175/1520-0477(1971)052<1186:PDVMIA>2.0.CO;2.

Brown, R. A., B. A. Flickinger, E. Forren, D. M. Schultz, D. Sirmans, P. L. Spencer, V. T. Wood, and C. L. Ziegler, 2005: Improved Detection of Severe Storms Using Experimental Fine-Resolution WSR-88D Measurements. *Weather and Forecasting*, **20**, 3–14, doi:10.1175/WAF-832.1.

Brown, R. A., V. T. Wood, and D. Sirmans, 2002: Improved Tornado Detection Using Simulated and Actual WSR-88D Data with Enhanced Resolution. *Journal of Atmospheric and Oceanic Technology*, **19**, 1759–1771, doi:10.1175/1520-0426(2002)019<1759:ITDUSA>2.0.CO;2.

Browning, K. A., 1962: Cellular structure of convective storms. *The Meteorological Magazine*, **91**, 341–350.

Burgess, D., and Coauthors, 2014: 20 May 2013 Moore, Oklahoma, Tornado: Damage Survey and Analysis. *Weather and Forecasting*, **29**, 1229–1237, doi:10.1175/WAF-D-14-00039.1.

Burian, S. J., and J. M. Shepherd, 2005: Effect of urbanization on the diurnal rainfall pattern in Houston. *Hydrological Processes*, **19**, 1089–1103, doi:10.1002/hyp.5647.

Campbell, J. B., and R. H. Wynne, 2011: *History and Scope of Remote Sensing*, 3–28. Guilford Press, New York.

Carey, L. D., and K. M. Buffalo, 2007: Environmental Control of Cloud-to-Ground Lightning Polarity in Severe Storms . *Monthly Weather Review*, **135**, 1327–1353, doi:10.1175/MWR3361.1.

Changnon Jr., S. A., 1968: The La Porte weather anomaly – fact of fiction? *Bulletin of the American Meteorological Society*, **49**, 4–11.

Changnon Jr., S. A., 1979: Rainfall Changes in Summer Caused by St. Louis. *Science*, **205**, 402–404, doi:10.1126/science.205.4404.402.

Changnon Jr., S. A., 1980: More on the La Porte Anomaly: A Review. *Bulletin of the American Meteorological Society*, **61**, 702–711, doi:10.1175/1520-0477(1980)061<0702:MOTLPA>2.0.CO;2.

Changnon Jr., S. A., and F. A. Huff, 1961: Studies of radar-depicted precipitation lines. Scientific Report 2, Illinois State Water Survey, 63 pp.

Changnon Jr., S. A., F. A. Huff, and R. G. Semonin, 1971: METROMEX: an Investigation of Inadvertent Weather Modification. *Bulletin of the American Meteorological Society*, **52**, 958–968, doi:10.1175/1520-0477(1971)052<0958:MAIOIW>2.0.CO;2.

Changnon Jr., S. A., R. T. Shealy, and R. W. Scott, 1991: Precipitation Changes in Fall, Winter, and Spring Caused by St. Louis. *Journal of Applied Meteorology*, **30**, 126–134, doi:10.1175/1520-0450(1991)030<0126:PCIFWA>2.0.CO;2.

Chen, F., and Coauthors, 2011: The integrated wrf/urban modelling system: development, evaluation, and applications to urban environmental problems. *International Journal of Climatology*, **31**, 273–288, doi:10.1002/joc.2158.

Chen, L., Y. Zhang, W. Lu, D. Zheng, Y. Zhang, S. Chen, and Z. Huang, 2012: Performance Evaluation for a Lightning Location System Based on Observations of Artificially Triggered Lightning and Natural Lightning Flashes. *Journal of Atmospheric and Oceanic Technology*, **29**, 1835–1844.

Christian, H. J., and Coauthors, 2003: Global frequency and distribution of lightning as observed from space by the optical transient detector. *Journal of Geophysical Research: Atmospheres*, **108**, ACL 4–1–ACL 4–15, doi:10.1029/2002JD002347.

Cintineo, J. L., T. M. Smith, V. Lakshmanan, H. E. Brooks, and K. L. Ortega, 2012: An Objective High-Resolution Hail Climatology of the Contiguous United States. *Weather and Forecasting*, **27**, 1235–1248, doi:10.1175/WAF-D-11-00151.1.

Clark, C. A., and P. W. Arritt, 1995: Numerical Simulations of the Effect of Soil Moisture and Vegetation Cover on the Development of Deep Convection. *Journal of Applied Meteorology*, **34**, 2029–2045, doi:10.1175/1520-0450(1995)034<2029:NSOTEO>2.0.CO;2.

Cohen, W. B., and S. N. Goward, 2004: Landsat's role in ecological applications of remote sensing. *Bioscience*, **54**, 535–545, doi:10.1641/0006-3568(2004)054[0535:LRIEAO]2.0.CO;2.

Cohen, W. B., T. A. Spies, R. J. Alig, D. R. Oetter, T. K. Maiersperger, and M. Fiorella, 2002: Characterizing 23 Years (1972–95) of Stand Replacement Disturbance in Western Oregon Forests with Landsat Imagery. *Ecosystems*, **5**, 122–137, doi:10.1007/s10021-001-0060-X.

Cohen, W. B., T. A. Spies, and M. Fiorella, 1995: Estimating the age and structure of forests in a multi-ownership landscape of western Oregon, U.S.A. *International Journal of Remote Sensing*, **16**, 721–746, doi:10.1080/01431169508954436.

Correa-Henao, G. J., J. M. Yusta, and R. Lacal-Arántegui, 2013: Using interconnected risk maps to assess the threats faced by electricity infrastructures. *International Journal of Critical Infrastructure Protection*, **6**, 197–216, doi:10.1016/j.ijcip.2013.10.002.

Crist, E. P., 1985: A TM Tasseled Cap equivalent transformation for reflectance factor data. *Remote Sensing of Environment*, **17**, 301–306, doi:10.1016/0034-4257(85)90102-6.

Crist, E. P., and R. C. Cicone, 1984: Application of the Tasseled Cap concept to simulated thematic mapper data. *Photogrammetric Engineering and Remote Sensing*, **50**, 343–352.

Crum, T. D., and R. L. Alberty, 1993: The WSR-88D and the WSR-88D Operational Support Facility. *Bulletin of the American Meteorological Society*, **74**, 1669–1687, doi:10.1175/1520-0477(1993)074<1669:TWATWO>2.0.CO;2.

Crum, T. D., R. L. Alberty, and D. W. Burgess, 1993: Recording, Archiving, and Using WSR-88D Data. *Bulletin of the American Meteorological Society*, **74**, 645–653, doi:10.1175/1520-0477(1993)074<0645:RAAUWD>2.0.CO;2.

Crum, T. D., R. E. Saffle, and J. W. Wilson, 1998: An Update on the NEXRAD Program and Future WSR-88D Support to Operations. *Weather and Forecasting*, **13**, 253–262, doi:10.1175/1520-0434(1998)013<0253:AUOTNP>2.0.CO;2.

Cummins, K. L., E. P. Krider, and M. D. Malone, 1998a: The US National Lightning Detection Network and applications of cloud-to-ground lightning data by electric power utilities. *IEEE Transactions on Electromagnetic Compatibility*, **40**, 465–480, doi:10.1109/15.736207.

Cummins, K. L., and M. J. Murphy, 2009: An Overview of Lightning Locating Systems: History, Techniques, and Data Uses, With an In–Depth Look at the U.S. NLDN. *IEEE Transactions on Electromagnetic Compatibility*, **51**, 499–518, doi:10.1109/TEMC.2009.2023450.

Cummins, K. L., M. J. Murphy, E. A. Bardo, W. L. Hiscox, R. B. Pyle, and A. E. Pifer, 1998b: A Combined TOA/MDF Technology Upgrade of the U.S. National Lightning Detection Network. *Journal of Geophysical Research: Atmospheres*, **103**, 9035–9044, doi:10.1029/98JD00153.

Curran, E. B., R. L. Holle, and R. E. López, 2000: Lightning Casualties and Damages in the United States from 1959 to 1994. *Journal of Climate*, **13**, 3448–3464, doi:10.1175/1520-0442(2000)013<3448:LCADIT>2.0.CO;2.

Davies-Jones, R. P., D. W. Burgess, L. R. Lemon, and D. Purcell, 1978: Interpretation of Surface Marks and Debris Patterns from the 24 May 1973 Union City, Oklahoma Tornado. *Monthly Weather Review*, **106**, 12–21, doi:10.1175/1520-0493(1978)106<0012:IOSMAD>2.0.CO;2.

Davis, W. M., 1886: Thunderstorms in New England in the Summer of 1885. *Proceedings of the American Academy of Arts and Sciences*, **22**, 14–58, doi:10.1016/j.jag.2015.10.009.

de Beurs, K. M., B. C. Owsley, and J. P. Julian, 2016: Disturbance analyses of forests and grasslands with MODIS and Landsat in New Zealand. *International Journal of Applied Earth Observation and Geoinformation*, **45**, 42–54, doi:10.1016/j.jag.2015.10.009.

Deierling, W., and W. A. Petersen, 2008: Total lightning activity as an indicator of updraft characteristics. *Journal of Geophysical Research: Atmospheres*, **113**, 2156–2202, doi:10.1029/2007JD009598.

Deng, C., and C. Wu, 2012: BCI: A biophysical composition index for remote sensing of urban environments. *Remote Sensing of Environment*, **127**, 247–259, doi:10.1016/j.rse.2012.09.009.

Devadoss, S. L., and J. O'Rourke, 2011: *Discrete and Computational Geometry*. Princeton University Press, 280 pp.

Diem, J. E., and T. L. Mote, 2005: Interepochal Changes in Summer Precipitation in the Southeastern United States: Evidence of Possible Urban Effects near Atlanta, Georgia. *Journal of Applied Meteorology*, **44**, 717–730, doi:10.1175/JAM2221.1.

Diendorfer, G., H. Pichler, and M. Mair, 2009: Some Parameters of Negative Upward-Initiated Lightning to the Gaisberg Tower (2000–2007). *IEEE Transactions on Electromagnetic Compatibility*, **51**, 443–452, doi:10.1109/TEMC.2009.2021616.

Dixon, P. G., and T. L. Mote, 2003: Patterns and Causes of Atlanta's Urban Heat Island–Initiated Precipitation. *Journal of Applied Meteorology*, **42**, 1273–1284, doi:10.1175/1520-0450(2003)042<1273:PACOAU>2.0.CO;.

Doswell III, C. A., H. E. Brooks, and N. Dotzek, 2009: On the implementation of the enhanced Fujita scale in the USA. *Atmospheric Research*, **93**, 554–563, doi:10.1016/j.atmosres.2008.11.003.

Doswell III, C. A., H. E. Brooks, and M. P. Kay, 2005: Climatological Estimates of Daily Local Nontornadic Severe Thunderstorm Probability for the United States. *Weather and Forecasting*, **20**, 577–595, doi:10.1175/WAF866.1.

Doswell III, C. A., and D. W. Burgess, 1988: On Some Issues of United States Tornado Climatology. *Monthly Weather Review*, **116**, 495–501, doi:10.1175/1520-0493(1988)116<0495:OSIOUS>2.0.CO;2.

Dou, J., Y. Wang, R. Bornstein, and S. Miao, 2015: Observed Spatial Characteristics of Beijing Urban Climate Impacts on Summer Thunderstorms. *Journal of Applied Meteorology and Climatology*, **54**, 94–105, doi:10.1175/JAMC-D-13-0355.1.

Drusch, M., and Coauthors, 2012: Sentinel-2: ESA's Optical High-Resolution Mission for GMES Operational Services. *Remote Sensing of Environment*, **120**, 25 – 36, doi:10.1016/j.rse.2011.11.026.

Dworak, R., K. Bedka, J. Brunner, and W. Feltz, 2012: Comparison between GOES-12 Overshooting-Top Detections, WSR-88D Radar Reflectivity, and Severe Storm Reports. *Weather and Forecasting*, **27**, 684–699, doi:10.1175/WAF-D-11-00070.1.

Dyer, R. C., 1988: Remote sensing identification of tornado tracks in Argentina, Brazil, and Paraguay. *Photogrammetric Engineering and Remote Sensing*, **54**, 1429–1435.

Edwards, R., J. G. LaDue, J. T. Feree, K. Scharfenberg, C. Maier, and W. L. Coulbourne, 2013: Tornado Intensity Estimation: Past, Present, and Future. *Bulletin of the American Meteorological Society*, **94**, 641–653, doi:10.1175/BAMS-D-11-00006.1.

Emersic, C., P. L. Heinselman, D. R. MacGorman, and E. C. Bruning, 2011: Lightning Activity in a Hail-Producing Storm Observed with Phased-Array Radar. *Monthly Weather Review*, **139**, 1809–1825, doi:10.1175/2010MWR3574.1.

Fan, J., Y. Wang, D. Rosenfeld, and X. Liu, 2016: Review of Aerosol–Cloud Interactions: Mechanisms, Significance, and Challenges. *Journal of the Atmospheric Sciences*, **73**, 4221–4252, doi:10.1175/JAS-D-16-0037.1.

Federal Emergency Management Agency, 2012: Spring 2011 Tornadoes: April 25-28 and May 22, Building Performance Observations, Recommendations, and Technical Guidance. FEMA Report P-908, Federal Emergency Management Agency, 512 pp. URL https://www.fema.gov/media-library-data/20130726-1827-25045-2783/tornado_mat_frontmatter_508.pdf.

Fleenor, S. A., C. J. Biagi, K. L. Cummins, E. P. Krider, and X.-M. Shao, 2009: Characteristics of cloud-to-ground lightning in warm-season thunderstorms in the Central Great Plains. *Atmospheric Research*, **91**, 333–352, doi:10.1016/j.atmosres.2008.08.011.

Foley, J. A., and Coauthors, 2005: Global consequences of land use. *Science*, **309 (5734)**, 570–574, doi:10.1126/science.1111772.

Friess, D. A., and T. Jazeel, 2017: Unlearning âĂIJLandscapeâĂİ. *Annals of the American Association of Geographers*, **107**, 14–21, doi:10.1080/24694452.2016.1230414.

Fujita, T. T., 1971: Proposed characterization of tornadoes and hurricanes by area and intensity. SMRP Technical Report 91, University of Chicago, 42 pp.

Fujita, T. T., 1989: The Teton-Yellowstone Tornado of 21 July 1987. *Monthly Weather Review*, **117**, 1913–1940, doi:10.1175/1520-0493(1989)117<1913:TTYTOJ>2.0.CO;2.

Gallo, K., T. Smith, K. Jungbluth, and P. Schumacher, 2012: Hail Swaths Observed from Satellite Data and Their Relation to Radar and Surface-Based Observations: A Case Study from Iowa in 2009. *Weather and Forecasting*, **27**, 796–802, doi:10.1175/WAF-D-11-00118.1.

Gallo, K. P., and T. W. Owen, 1999: Satellite-Based Adjustments for the Urban Heat Island Temperature Bias. *Journal of Applied Meteorology*, **38**, 806–813, doi:10.1175/1520-0450(1999)038<0806:SBAFTU>2.0.CO;2.

Galway, J. O., 1992: Early Severe Thunderstorm Forecasting and Research by the United States weather Bureau. *Weather and Forecasting*, **7**, 564–587, doi:10.1175/1520-0434(1992)007<0564:ESTFAR>2.0.CO;2.

Gao, B., 1996: NDWI–A normalized difference water index for remote sensing of vegetation liquid water from space. *Remote Sensing of Environment*, **58**, 257–266, doi:10.1016/S0034-4257(96)00067-3.

Garolera, A. C., K. L. Cummins, S. F. Madsen, J. Holboell, and J. D. Myers, 2015: Multiple Lightning Discharges in Wind Turbines Associated With Nearby Cloud-to-Ground Lightning. *IEEE Transactions on Sustainable Energy*, **6**, 526–533, doi:10.1109/TSTE.2015.2391013.

Gary, C., 1994: *La Foundre. Des Mythologies Antiques á la Recherche Moderne*. Masson, 208 pp.

Gero, A. F., and A. J. Pitman, 2006: The Impact of Land Cover Change on a Simulated Storm Event in the Sydney Basin. *Journal of Applied Meteorology and Climatology*, **45**, 283–300, doi:10.1175/JAM2337.1.

Gray, M., 2009: Landscape: The Physical Layer. *Key Concepts in Geography*, N. J. Clifford, S. L. Holloway, S. P. Rice, and G. Valentine, Eds., SAGE, 265–299.

Greene, D. R., and R. A. Clark, 1972: Vertically Integrated Liquid Water–A New Analysis Tool. *Monthly Weather Review*, **100**, 548–552, doi:10.1175/1520-0493(1972)100<0548:VILWNA>2.3.CO;2.

Groisman, P. Y., and D. R. Easterling, 1994: Variability and Trends of Total Precipitation and Snowfall over the United States and Canada. *Journal of Climate*, **7**, 184–205, doi:10.1175/1520-0442(1994)007<0184:VATOTP>2.0.CO;2.

Haberlie, A. M., W. S. Ashley, and T. J. Pingel, 2015: The effect of urbanisation on the climatology of thunderstorm initiation. *Quarterly Journal of the Royal Meteorological Society*, **141**, 663–675, doi:10.1002/qj.2499.

Hand, L. M., and J. M. Shepherd, 2009: An Investigation of Warm-Season Spatial Rainfall Variability in Oklahoma City: Possible Linkages to Urbanization and Prevailing Wind. *Journal of Applied Meteorology and Climatology*, **48**, 251–269, doi:10.1175/2008JAMC2036.1.

Harland, W. B., and J. L. F. Hacker, 1966: Fossil lightning strikes 250 million years ago. *Advancement of Science*, **22**, 663–671.

Healey, S. P., W. B. Cohen, Y. Zhiqiang, and O. N. Krankina, 2005: Comparison of Tasseled Cap-based Landsat data structures for use in forest disturbance detection. *Remote Sensing of Environment*, **97**, 301–310, doi:10.1016/j.rse.2005.05.009.

Henebry, G. M., and I. C. Ratcliffe, 2003: Occurrence and persistence of hailstreaks in the vegetated land surface. *Preprints, 17th Conf. on Hydrology*, American Meteorological Society, Long Beach, California, USA, JP5.3.

Herzog, B. S., K. M. Calhoun, and D. R. MacGorman, 2014: Total lightning information in a 5-Year Thunderstorm Climatology. *Preprints, XV International Conference on Atmospheric Electricity*, American Meteorological Society, Norman, Oklahoma, USA, 22pp.

Heymsfield, G. M., R. Fulton, and J. D. Spinhirne, 1991: Aircraft Overflight Measurements of Midwest Severe Storms: Implications an Geosynchronous Satellite Interpretations. *Monthly Weather Review*, **119**, 436–456, doi:10.1175/1520-0493(1991)119<0436:AOMOMS>2.0.CO;2.

Hilbert, M., and P. López, 2011: The World's Technological Capacity to Store, Communicate, and Compute Information. *Science*, **332**, 60–65, doi:10.1126/science.1200970.

Hilker, T., M. A. Wulder, N. C. Coops, J. Linke, G. McDermid, J. G. Masek, F. Gao, and J. C. White, 2009: A new data fusion model for high spatial- and temporal-resolution mapping of forest disturbance based on Landsat and MODIS. *Remote Sensing of Environment*, **113**, 1613–1627, doi:10.1016/j.rse.2009.03.007.

Hill, C. M., P. J. Fitzpatrick, J. H. Corbin, Y. H. Lau, and S. K. Bhate, 2010: Summertime Precipitation Regimes Associated with the Sea Breeze and Land Breeze in Southern Mississippi and Eastern Louisiana. *Weather and Forecasting*, **25**, 1755–1779, doi:10.1175/2010WAF2222340.1.

Hitaj, C., 2013: Wind power development in the United States. *Journal of Environmental Economics and Management*, **65**, 394–410, doi:10.1016/j.jeem.2012.10.003.

Hobson, A. G. K., V. Lakshmanan, T. M. Smith, and M. Richman, 2012: An automated technique to categorize storm type from radar and near-storm environment data. *Atmospheric Research*, **111**, 104–113, doi:10.1016/j.atmosres.2012.03.004.

Holland, A. P., A. J. Riordan, and E. C. Franklin, 2006: A Simple Model for Simulating Tornado Damage in Forests. *Journal of Applied Meteorology and Climatology*, **45**, 1597–1611, doi:10.1175/JAM2413.1.

Holle, R. L., K. L. Cummins, and W. A. Brooks, 2016: Seasonal, Monthly, and Weekly Distributions of NLDN and GLD360 Cloud-to-Ground Lightning. *Monthly Weather Review*, **144**, 2855–2870, doi:10.1175/MWR-D-16-0051.1.

Homer, C., and Coauthors, 2015: Completion of the 2011 National Land Cover Database for the conterminous United States-Representing a decade of land cover change information. *Photogrammetric Engineering and Remote Sensing*, **81**, 345–354.

House, F. B., A. Gruber, G. E. Hunt, and A. T. Mecherikunnel, 1986: History of satellite missions and measurements of the Earth Radiation Budget (1957–1984). *Reviews of Geophysics*, **24**, 357–377, doi:10.1029/RG024i002p00357.

Huete, A., K. Didan, T. Miura, E. P. Rodriguez, X. Gao, and L. G. Ferreira, 2002: Overview of the radiometric and biophysical performance of the MODIS vegetation indices. *Remote Sensing of Environment*, **83**, 195–213, doi:10.1016/S0034-4257(02)00096-2.

Huete, A. R., 1988: A soil-adjusted vegetation index (SAVI). *Remote Sensing of Environment*, **25**, 295–309, doi:10.1016/0034-4257(88)90106-X.

Huete, A. R., and R. D. Jackson, 1987: Suitability of spectral indices for evaluating vegetation characteristics on arid rangelands. *Remote Sensing of Environment*, **23**, 213–232, doi:10.1016/0034-4257(87)90038-1.

Huff, F. A., and S. A. Changnon Jr., 1972: Climatological assessment of urban effects on precipitation at st. louis. *Journal of Applied Meteorology*, **11**, 823–842, doi:10.1175/1520-0450(1972)011<0823:CAOUEO>2.0.CO;2.

Huff, F. A., and S. A. Changnon Jr., 1973: Precipitation modification by major urban areas. *Bulletin of the American Meteorological Society*, **54**, 1220–1232, doi:10.1175/1520-0477(1973)054<1220:PMBMUA>2.0.CO;2.

Irons, J. R., J. L. Dwyer, and J. A. Barsi, 2012: The next Landsat satellite: The Landsat Data Continuity Mission. *Remote Sensing of Environment*, **122**, 11–21, doi:10.1016/j.rse.2011.08.026.

Jauregui, E., and E. Romales, 1996: Urban effects on convective precipitation in Mexico city. *Atmospheric Environment*, **30**, 3383–3389, doi:10.1016/1352-2310(96)00041-6.

Jedlovec, G. J., U. Nair, and S. L. Hainer, 2006: Detection of Storm Damage Tracks with EOS Data. *Weather and Forecasting*, **21**, 249–267, doi:10.1175/WAF923.1.

Jing, Z., and G. Wiener, 1993: Two-Dimensional Dealiasing of Doppler Velocities. *Journal of Atmospheric and Oceanic Technology*, **10**, 798–808, doi:10.1175/1520-0426(1993)010<0798:TDDODV>2.0.CO;2.

Karstens, C. D., W. A. Gallus Jr., B. D. Lee, and C. A. Finley, 2013: Analysis of Tornado-Induced Tree Fall Using Aerial Photography from the Joplin, Missouri, and Tuscaloosa–Birmingham, Alabama, Tornadoes of 2011. *Journal of Applied Meteorology and Climatology*, **52**, 1049–1068, doi:10.1175/JAMC-D-12-0206.1.

Kauth, R. J., and G. S. Thomas, 1976: The tasselled cap - A graphic description of the spectral-temporal development of agricultural crops as seen by Landsat. *Conference Proceedings, Symposium on Machine Processing of Remotely Sensed Data*, Environmental Research Institute of Michigan, West Lafayette, Indiana, USA, 1–11.

Kawecki, S., G. M. Henebry, and A. L. Steiner, 2016: Effects of Urban Plume Aerosols on a Mesoscale Convective System. *Journal of the Atmospheric Sciences*, **73**, 4641–4660, doi:10.1175/JAS-D-16-0084.1.

King, P., 1997: On the Absence of Population Bias in the Tornado Climatology of Southwestern Ontario. *Weather and Forecasting*, **12**, 939–946, doi:10.1175/1520-0434(1997)012<0939:OTAOPB>2.0.CO;2.

Kingfield, D. M., and J. G. LaDue, 2015: The Relationship between Automated Low-Level Velocity Calculations from the WSR-88D and Maximum Tornado Intensity

Determined from Damage Surveys. *Weather and Forecasting*, **30**, 1125–1139, doi: 10.1175/WAF-D-14-00096.1.

Kishtawal, C. M., D. Niyogi, M. Tewari, R. A. Pielke, and J. M. Shepherd, 2010: Urbanization signature in the observed heavy rainfall climatology over India. *International Journal of Climatology*, **30**, 1908–1916, doi:10.1002/joc.2044.

Kitterman, C. G., 1981: Concurrent lightning flashes on two television transmission towers. *Journal of Geophysical Research: Oceans*, **86**, 5378–5380, doi:10.1029/JC086iC06p05378.

Klimowski, B. A., M. R. Hjelmfelt, M. J. Bunkers, D. Sedlacek, and L. R. Johnson, 1998: Hailstorm Damage Observed from the GOES-8 Satellite: The 5–6 July 1996 Butte–Meade Storm. *Monthly Weather Review*, **126**, 831–834, doi: 10.1175/1520-0493(1998)126<0831:HDOFTG>2.0.CO;2.

Knupp, K. R., and Coauthors, 2014: Meteorological Overview of the Devastating 27 April 2011 Tornado Outbreak. *Bulletin of the American Meteorological Society*, **95**, 1041–1062, doi:10.1175/BAMS-D-11-00229.1.

Krider, E. P., R. C. Noggle, A. E. Pifer, and D. L. Vance, 1980: Lightning Direction-Finding Systems for Forest Fire Detection. *Bulletin of the American Meteorological Society*, **61**, 980–986, doi:10.1175/1520-0477(1980)061<0980:LDFSFF>2.0.CO;2.

Krider, E. P., R. C. Noggle, and M. A. Uman, 1976: A Gated, Wideband Magnetic Direction Finder for Lightning Return Strokes. *Journal of Applied Meteorology*, **15**, 301–306, doi:10.1175/1520-0450(1976)015<0301:AGWMDF>2.0.CO;2.

Kumjian, M. R., 2013: Principles and applications of dual-polarization weather radar. Part I: Description of the polarimetric radar variables. *Journal of Operational Meteorology*, **1**, 226–242, doi:10.15191/nwajom.2013.0119.

Lafkovici, A., A. M. Hussein, W. Janischewskyj, and K. L. Cummins, 2008: Evaluation of the Performance Characteristics of the North American Lightning Detection Network Based on Tall-Structure Lightnings. *IEEE Transactions on Electromagnetic Compatibility*, **50**, 630–641, doi:10.1109/TEMC.2008.927922.

Lakshmanan, V., A. Fritz, T. Smith, K. Hondl, and G. Stumpf, 2007a: An Automated Technique to Quality Control Radar Reflectivity Data. *Journal of Applied Meteorology and Climatology*, **46**, 288–305, doi:10.1175/JAM2460.1.

Lakshmanan, V., B. Herzog, and D. Kingfield, 2015: A Method for Extracting Postevent Storm Tracks. *Journal of Applied Meteorology and Climatology*, **54**, 451–462, doi:10.1175/JAMC-D-14-0132.1.

Lakshmanan, V., K. Hondl, and R. Rabin, 2009: An Efficient, General-Purpose Technique for Identifying Storm Cells in Geospatial Images. *Journal of Atmospheric and Oceanic Technology*, **26**, 523–537, doi:10.1175/2008JTECHA1153.1.

Lakshmanan, V., T. Smith, K. Hondl, G. J. Stumpf, and A. Witt, 2006: A Real-Time, Three-Dimensional, Rapidly Updating, Heterogeneous Radar Merger Technique for Reflectivity, Velocity, and Derived Products. *Weather and Forecasting*, **21**, 802–823, doi:10.1175/WAF942.1.

Lakshmanan, V., T. Smith, G. Stumpf, and K. Hondl, 2007b: The Warning Decision Support System–Integrated Information. *Weather and Forecasting*, **22**, 596–612, doi:10.1175/WAF1009.1.

Lauer, D. T., S. A. Morain, and V. V. Salomonson, 1997: The landsat program: Its origins, evolution, and impacts. *Photogrammetric Engineering and Remote Sensing*, **63**, 831–838.

Lebo, Z. J., 2014: The Sensitivity of a Numerically Simulated Idealized Squall Line to the Vertical Distribution of Aerosols. *Journal of the Atmospheric Sciences*, **71**, 4581–4596, doi:10.1175/JAS-D-14-0068.1.

Lemon, L. R., and C. A. D. III, 1979: Severe Thunderstorm Evolution and Mesocyclone Structure as Related to Tornadogenesis. *Monthly Weather Review*, **107**, 1184–1197, doi:10.1175/1520-0493(1979)107<1184:STEAMS>2.0.CO;2.

Lemons, H., 1942: Hail in American Agriculture. *Economic Geography*, **18**, 363–378, doi:10.2307/141444.

Lewis, E. A., R. B. Harvey, and J. E. Rasmussen, 1960: Hyperbolic direction finding with sferics of transatlantic origin. *Journal of Geophysical Research*, **65**, 1879–1905, doi:10.1029/JZ065i007p01879.

Lowry, W. P., 1998: Urban effects on precipitation amount. *Progress in Physical Geography*, **22**, 477–520, doi:10.1177/030913339802200403.

Lu, W., D. Wang, Y. Zhang, and N. Takagi, 2009: Two associated upward lightning flashes that produced opposite polarity electric field changes. *Geophysical Research Letters*, **36**, L05 801, doi:10.1029/2008GL036598.

Mach, D. M., D. R. MacGorman, W. D. Rust, and R. T. Arnold, 1986: Site Errors and Detection Efficiency in a Magnetic Direction-Finder Network for Locating Lightning Strikes to Ground. *Journal of Atmospheric and Oceanic Technology*, **3**, 67–74, doi:10.1175/1520-0426(1986)003<0067:SEADEI>2.0.CO;2.

Mark, H., 1988: A forward looking space policy for the USA. *Space Policy*, **4**, 19–23, doi:10.1016/0265-9646(88)90093-8.

Markham, B. L., J. C. Storey, D. L. Williams, and J. R. Irons, 2004: Landsat sensor performance: history and current status. *IEEE Transactions on Geoscience and Remote Sensing*, **42**, 2691–2694, doi:10.1109/TGRS.2004.840720.

Markowski, P. M., 2002: Hook Echoes and Rear-Flank Downdrafts: A Review. *Monthly Weather Review*, **130**, 852–876, doi:10.1175/1520-0493(2002)130<0852:HEARFD>2.0.CO;2.

Marshall, T. P., 2002: Tornado Damage Survey at Moore, Oklahoma. *Weather and Forecasting*, **17**, 582–598, doi:10.1175/1520-0434(2002)017<0582:TDSAMO>2.0.CO;2.

Masek, J. G., C. Huang, R. Wolfe, W. Cohen, F. Hall, J. Kutler, and P. Nelson, 2008: North American forest disturbance mapped from a decadal Landsat record. *Remote Sensing of Environment*, **112**, 2914–2926, doi:10.1016/j.rse.2008.02.010.

Masek, J. G., and Coauthors, 2006: A Landsat surface reflectance dataset for North America, 1990-2000. *IEEE Geoscience and Remote Sensing Letters*, **3**, 68–72, doi:10.1109/LGRS.2005.857030.

Matyas, C. J., 2010: Use of Ground-based Radar for Climate-Scale Studies of Weather and Rainfall. *Geography Compass*, **4**, 1218–1237, doi:10.1111/j.1749-8198.2010.00370.x.

Maynard, R. H., 1945: Radar and weather. *Journal of Meteorology*, **2**, 214–226.

Mazur, V., and L. H. Ruhnke, 2011: Physical processes during development of upward leaders from tall structures. *Journal of Electrostatics*, **69**, 97–110, doi:10.1016/j.elstat.2011.01.003.

McCann, D. W., 1983: The Enhanced-V: A Satellite Observable Severe Storm Signature. *Monthly Weather Review*, **111**, 887–894, doi:10.1175/1520-0493(1983)111<0887:TEVASO>2.0.CO;2.

McEachron, K. B., 1939: Lightning to the empire state building. *Journal of the Franklin Institute*, **227**, 149–217, doi:10.1016/S0016-0032(39)90397-2.

McPherson, R. A., 2007: A review of vegetation–atmosphere interactions and their influences on mesoscale phenomena. *Progress in Physical Geography*, **31**, 261–285, doi:10.1177/0309133307079055.

McPherson, R. A., and D. J. Stensrud, 2005: Influences of a Winter Wheat Belt on the Evolution of the Boundary Layer. *Monthly Weather Review*, **133**, 2178–2199, doi:10.1175/MWR2968.1.

Melillo, J. M., T. Richmond, and G. W. Yohe, 2014: Climate Change Impacts in the United States: The Third National Climate Assessment. Tech. rep., U.S. Global Change Research Program, 841 pp. doi:10.7930/J0Z31WJ2.

Miller, M. L., V. Lakshmanan, and T. M. Smith, 2013: An Automated Method for Depicting Mesocyclone Paths and Intensities. *Weather and Forecasting*, **28**, 570–585, doi:10.1175/WAF-D-12-00065.1.

Minor, J. E., J. R. McDonald, and K. C. Mehta, 1977: The Tornado: An Engineering Oriented Perspective. NOAA Technical Memorandum ERL NSSL-82, National Oceanic and Atmospheric Administration, 220 pp.

Mitra, C., and J. M. Shepherd, 2016: Urban Precipitation: A global perspective. *The Routledge Handbook of Urbanization and Global Environmental Change*, K. C. Seto, W. Solecki, and C. A. Griffith, Eds., Routledge, 152–168.

Mitra, C., J. M. Shepherd, and T. Jordan, 2012: On the relationship between the premonsoonal rainfall climatology and urban land cover dynamics in Kolkata city, India. *International Journal of Climatology*, **32**, 1443–1454, doi:10.1002/joc.2366.

Molthan, A. L., J. R. Bell, T. A. Cole, and J. E. Burks, 2014: Satellite-based identification of tornado damage tracks from the 27 April 2011 severe weather outbreak. *Journal of Operational Meteorology*, **2**, 191–208, doi:10.15191/nwajom.2014.0216.

Montz, B. E., and G. A. Tobin, 2011: Natural hazards: An evolving tradition in applied geography. *Applied Geography*, **31**, 1–4, doi:10.1016/j.apgeog.2010.06.005.

Mote, T. L., M. C. Lacke, and J. M. Shepherd, 2007: Radar signatures of the urban effect on precipitation distribution: A case study for Atlanta, Georgia. *Geophysical Research Letters*, **34**, L20 710, doi:10.1029/2007GL031903.

National Academies of Sciences, Engineering, and Medicine, 2015: Fostering Transformative Research in the Geographical Sciences. Tech. rep., National Academies of Sciences, Engineering, and Medicine, 90 pp.

Nemunaitis-Berry, K. L., P. M. Klein, J. B. Basara, and E. Fedorovich, 2017: Sensitivity of Predictions of the Urban Surface Energy Balance and Heat Island to Variations of Urban Canopy Parameters in Simulations with the WRF Model. *Journal of Applied Meteorology and Climatology*, **56**, 573–595, doi:10.1175/JAMC-D-16-0157.1.

Niyogi, D., T. Holt, S. Zhong, P. C. Pyle, and J. Basara, 2006: Urban and land surface effects on the 30 July 2003 mesoscale convective system event observed in the southern Great Plains. *Journal of Geophysical Research: Atmospheres*, **111**, D19 107, doi:10.1029/2005JD006746.

Niyogi, D., P. Pyle, M. Lei, S. P. Arya, C. M. Kishtawal, M. Shepherd, F. Chen, and B. Wolfe, 2011: Urban Modification of Thunderstorms: An Observational Storm Climatology and Model Case Study for the Indianapolis Urban Region. *Journal of Applied Meteorology and Climatology*, **50**, 1129–1144, doi:10.1175/2010JAMC1836.1.

NOAA, 2011: The historic tornadoes of April 2011. NWS service assessment, National Oceanic and Atmospheric Administration, 76 pp.

NOAA NCEI, 2014: Climatological Rankings. NOAA, URL http://www.ncdc.noaa.gov/temp-and-precip/ranks.php.

Ntelekos, A. A., J. A. Smith, L. Donner, J. D. Fast, W. I. Gustafson, E. G. Chapman, and W. F. Krajewski, 2009: The effects of aerosols on intense convective precipitation in the northeastern United States. *Quarterly Journal of the Royal Meteorological Society*, **135**, 1367–1391, doi:10.1002/qj.476.

Ntelekos, A. A., J. A. Smith, and W. F. Krajewski, 2007: Climatological Analyses of Thunderstorms and Flash Floods in the Baltimore Metropolitan Region. *Journal of Hydrometeorology*, **8**, 88–101, doi:10.1175/JHM558.1.

Odum, E. P., 1969: The Strategy of Ecosystem Development. *Science*, **164**, 262–270, doi:10.1126/science.164.3877.262.

Oke, T., 1973: City size and the urban heat island. *Atmospheric Environment*, **7**, 769–779, doi:10.1016/0004-6981(73)90140-6.

Oke, T., 1987: *Boundary Layer Climates: 2nd Edition*. Routledge, 435 pp.

Orville, R. E., 2008: Development of the National Lightning Detection Network. *Bulletin of the American Meteorological Society*, **89**, 180–190, doi:10.1175/BAMS-89-2-180.

Orville, R. E., R. W. Henderson, and L. F. Bosart, 1983: An East Coast Lightning Detection Network. *Bulletin of the American Meteorological Society*, **64**, 1029–1037, doi:10.1175/1520-0477(1983)064<1029:AECLDN>2.0.CO;2.

Parker, M. D., I. C. Ratcliffe, and G. M. Henebry, 2005: The July 2003 Dakota Hailswaths: Creation, Characteristics, and Possible Impacts. *Monthly Weather Review*, **133**, 1241–1260, doi:10.1175/MWR2914.1.

Pielke, R. A., J. Adegoke, A. BeltraÃąN-Przekurat, C. A. Hiemstra, J. Lin, U. S. Nair, D. Niyogi, and T. E. Nobis, 2007: An overview of regional land-use and land-cover impacts on rainfall. *Tellus B: Chemical and Physical Meteorology*, **59**, 587–601, doi:10.1111/j.1600-0889.2007.00251.x.

Pielke, R. A., G. A. Dalu, J. S. Snook, T. J. Lee, and T. G. F. Kittel, 1991: Nonlinear Influence of Mesoscale Land Use on Weather and Climate. *Journal of Climate*, **4**, 1053–1069, doi:10.1175/1520-0442(1991)004<1053:NIOMLU>2.0.CO;2.

Polger, P. D., B. S. Goldsmith, R. C. Przywarty, and J. R. Bocchieri, 1994: National Weather Service Warning Performance Based on the WSR-88D. *Bulletin of the American Meteorological Society*, **75**, 203–214, doi:10.1175/1520-0477(1994)075<0203:NWSWPB>2.0.CO;2.

Prinz, H., 1977: Lightning in history. *Lightning in history*, R. H. Golde, Ed., Academic Press, 1–21.

Probert-Jones, J. R., 1990: A history of radar meteorology in the United Kingdom. *Radar in Meteorology – Battan Memorial and 40th Anniversary Radar Meteorology Conference*, D. Atlas, Ed., American Meteorological Society, 54–60.

Rabin, R. M., D. J. Stensrud, S. Stadler, P. J. Wetzel, and M. Gregory, 1990: Observed Effects of Landscape Variability on Convective Clouds. *Bulletin of the American Meteorological Society*, **71**, 272–280, doi:10.1175/1520-0477(1990)071<0272:OEOLVO>2.0.CO;2.

Rakov, V. A., and M. A. Uman, 2003: *Lightning: Physics and Effects*. Cambridge Univ. Press, 700 pp.

RAND Corporation, 1946: Preliminary Design of an Experimental World-Circling Spaceship. Sm-11827, RAND Corportation, 328 pp.

Ray, P. S., R. J. Doviak, G. B. Walker, D. Sirmans, J. Carter, and B. Bumgarner, 1975: Dual-Doppler Observation of a Tornadic Storm. *Journal of Applied Meteorology*, **14**, 1521–1530, doi:10.1175/1520-0450(1975)014<1521:DDOOAT>2.0.CO;2.

Reames, L. J., and D. J. Stensrud, 2017: Sensitivity of simulated urban-atmosphere interactions in Oklahoma City to urban parameterization. *Journal of Applied Meteorology and Climatology*, In Press, doi:10.1175/JAMC-D-16-0223.1.

Richards, K., 2011: The Weather Station and the Meteorological Office. *The SAGE Handbook of Geographical Knowledge*, J. Agnew, and D. N. Livingstone, Eds., SAGE, 149–157.

Rison, W., J. Thomas, P. R. Krehbiel, T. Hamlin, and J. Harlin, 1999: A GPS-based three-dimensional lightning mapping system: Initial observations from New Mexico. *Geophysical Research Letters*, **26**, 3573–3576, doi:10.1029/1999GL010856.

Robaa, S. M., 2003: Urban-suburban/rural differences over Greater Cairo, Egypt. *Atmósfera*, **16**, 157–171.

Roberts, R. D., and S. Rutledge, 2003: Nowcasting Storm Initiation and Growth Using GOES-8 and WSR-88D Data. *Weather and Forecasting*, **18**, 562–584, doi:10.1175/1520-0434(2003)018<0562:NSIAGU>2.0.CO;2.

Rose, L. S., J. A. Stallins, and M. L. Bentley, 2008: Concurrent Cloud-to-Ground Lightning and Precipitation Enhancement in the Atlanta, Georgia (United States), Urban Region. *Earth Interactions*, **12**, 1–30, doi:10.1175/2008EI265.1.

Rosenfeld, D., U. Lohmann, G. B. Raga, C. D. O'Dowd, M. Kulmala, S. Fuzzi, A. Reissell, and M. O. Andreae, 2008: Flood or Drought: How Do Aerosols Affect Precipitation? *Science*, **321**, 1309–1313, doi:10.1126/science.1160606.

Rossum, S., and S. Lavin, 2000: Where Are the Great Plains? A Cartographic Analysis. *The Professional Geographer*, **52**, 543–552, doi:10.1111/0033-0124.00245.

Roth, M., 2007: Review of urban climate research in (sub)tropical regions. *International Journal of Climatology*, **27**, 1859–1873, doi:10.1002/joc.1591.

Rouse Jr., J. W., R. H. Haas, J. A. Schell, and D. W. Deering, 1973: Monitoring vegetation systems in the Great Plains with ERTS. *Preprints, Third ERTS Symposium*, National Aeronautics and Space Administration, Washington, D.C. USA, 309–317.

Ryde, J. W., 1946: The attenuation and radar echoes produced at centimeter wavelengths by various meteorological phenomena. *Preprints, Meteorological Factors in Radio-Wave Propagation*, Royal Institution, London, England, 169–188.

Schaefer, J. T., and R. Edwards, 1999: The SPC tornado/severe thunderstorm database. *Preprints, 11th Conf. Applied Climatology*, American Meteorological Society, Dallas, Texas, USA, 309–317.

Schmid, P. E., and D. Niyogi, 2013: Impact of city size on precipitation-modifying potential. *Geophysical Research Letters*, **40**, 5263–5267, doi:10.1002/grl.50656.

Schmid, P. E., and D. Niyogi, 2017: Modeling Urban Precipitation Modification by Spatially Heterogeneous Aerosols. *Journal of Applied Meteorology and Climatology*, In Press, doi:10.1175/JAMC-D-16-0320.1.

Schmit, T. J., M. M. Gunshor, W. P. Menzel, J. J. Gurka, J. Li, and A. S. Bachmeier, 2005: Introducing the Next-Generation Advanced Baseline Imager on GOES-R. *Bulletin of the American Meteorological Society*, **86**, 1079–1096, doi:10.1175/BAMS-86-8-1079.

Schroeder, T. A., M. A. Wulder, S. P. Healey, and G. G. Moisen, 2011: Mapping wildfire and clearcut harvest disturbances in boreal forests with Landsat time series data. *Remote Sensing of Environment*, **115**, 1421–1433, doi:10.1016/j.rse.2011.01.022.

Schultz, C. J., W. A. Petersen, and L. D. Carey, 2011: Lightning and Severe Weather: A Comparison between Total and Cloud-to-Ground Lightning Trends. *Weather and Forecasting*, **26**, 744–755, doi:10.1175/WAF-D-10-05026.1.

Schultz, D. M., and R. J. Vavrek, 2009: An overview of thundersnow. *Weather*, **64**, 274–277, doi:10.1002/wea.376.

Segele, Z. T., D. J. Stensrud, I. C. Ratcliffe, and G. M. Henebry, 2005: Influence of a Hailstreak on Boundary Layer Evolution. *Monthly Weather Review*, **133**, 942–960, doi:10.1175/MWR2897.1.

Seto, K. C., B. Güneralp, and L. R. Hutyra, 2012: Global forecasts of urban expansion to 2030 and direct impacts on biodiversity and carbon pools. *Proceedings of the National Academy of Sciences*, **109**, 16 083–16 088, doi:10.1073/pnas.1211658109.

Sheng, Y., 2011: Remote Sensing. *The SAGE Handbook of Geographical Knowledge*, J. Agnew, and D. N. Livingstone, Eds., SAGE, 171–184.

Shepherd, J. M., 2005: A Review of Current Investigations of Urban-Induced Rainfall and Recommendations for the Future. *Earth Interactions*, **9**, 1–27, doi:10.1175/EI156.1.

Shepherd, J. M., 2013: Impacts of urbanization on precipitation and storms: Physical insights and vulnerabilities. *Climate Vulnerability: Understanding and Addressing Threats to Essential Resources*, R. A. Pielke, Ed., Elsevier, 109–125.

Shepherd, J. M., and S. J. Burian, 2003: Detection of Urban-Induced Rainfall Anomalies in a Major Coastal City. *Earth Interactions*, **7**, 1–17, doi:10.1175/1087-3562(2003)007<0001:DOUIRA>2.0.CO;2.

Shepherd, J. M., H. Pierce, and A. J. Negri, 2002: Rainfall Modification by Major Urban Areas: Observations from Spaceborne Rain Radar on the TRMM Satellite. *Journal of Applied Meteorology*, **41**, 689–701, doi:10.1175/1520-0450(2002)041<0689:RMBMUA>2.0.CO;2.

Sheridan, S. C., 2002: The redevelopment of a weather-type classification scheme for North America. *International Journal of Climatology*, **22**, 51–68, doi:10.1002/joc.709.

Singh, A., 1989: Digital change detection techniques using remotely-sensed data. *International Journal of Remote Sensing*, **10**, 989–1003, doi:10.1080/01431168908903939.

Smith, B. T., R. L. Thompson, A. R. Dean, and P. T. Marsh, 2015: Diagnosing the Conditional Probability of Tornado Damage Rating Using Environmental and Radar Attributes. *Weather and Forecasting*, **30**, 914–932, doi:10.1175/WAF-D-14-00122.1.

Smith, B. T., R. L. Thompson, J. S. Grams, C. Broyles, and H. E. Brooks, 2012a: Convective Modes for Significant Severe Thunderstorms in the Contiguous United States. Part I: Storm Classification and Climatology. *Weather and Forecasting*, **27**, 1114–1135, doi:10.1175/WAF-D-11-00115.1.

Smith, J. A., M. L. Baeck, G. Villarini, C. Welty, A. J. Miller, and W. F. Krajewski, 2012b: Analyses of a long-term, high-resolution radar rainfall data set for the Baltimore metropolitan region. *Water Resources Research*, **48**, W04 504, doi:10.1029/2011WR010641.

Smith, J. A., A. A. Bradley, and M. L. Baeck, 1994: The Space–Time Structure of Extreme Storm Rainfall in the Southern Plains. *Journal of Applied Meteorology*, **33**, 1402–1417, doi:10.1175/1520-0450(1994)033<1402:TSSOES>2.0.CO;2.

Smith, T. M., and K. L. Elmore, 1994: The use of radial velocity derivatives to diagnose rotation and divergence. *Preprints, 11th Conf. on Aviation, Range, and Aerospace*, American Meteorological Society, Hyannis, Massachusetts, USA, P5.6.

Smith, T. M., and Coauthors, 2016: Multi-Radar Multi-Sensor (MRMS) Severe Weather and Aviation Products: Initial Operating Capabilities. *Bulletin of the American Meteorological Society*, **97**, 1617–1630, doi:10.1175/BAMS-D-14-00173.1.

Souch, C., and S. Grimmond, 2006: Applied climatology: urban climate. *Progress in Physical Geography*, **30**, 270–279, doi:10.1191/0309133306pp484pr.

Speheger, D. A., C. A. Doswell III, and G. J. Stumpf, 2002: The Tornadoes of 3 May 1999: Event Verification in Central Oklahoma and Related Issues. *Weather and Forecasting*, **17**, 362–381, doi:10.1175/1520-0434(2002)017<0362:TTOMEV>2.0.CO;2.

Stallins, J. A., M. L. Bentley, and L. S. Rose, 2006: Cloud-to-ground flash patterns for Atlanta, Georgia (USA) from 1992 to 2003. *Climate Research*, **30**, 99–112, doi:10.3354/cr030099.

Stallins, J. A., and L. S. Rose, 2008: Urban Lightning: Current Research, Methods, and the Geographical Perspective. *Geography Compass*, **2**, 620–639, doi:10.1111/j.1749-8198.2008.00110.x.

Stanley, M. A., and M. J. Heavner, 2003: Tall structure lightning induced by sprite-producing discharges. *Preprints, 12th International Conference on Atmospheric Electricity*, International Commission on Atmospheric Electricity, Versailles, France, 1–3.

Steiger, S. M., R. E. Orville, and G. Huffines, 2002: Cloud-to-ground lightning characteristics over Houston, Texas: 1989–2000. *Journal of Geophysical Research: Atmospheres*, **107**, ACL 2–1–ACL 2–12, doi:10.1029/2001JD001142.

Stout, G. E., and F. A. Huff, 1953: Radar records Illinois tornadogenesis. *Bulletin of the American Meteorological Society*, **34**, 281–284.

Sui, D., and R. Morrill, 2004: Computers and Geography: From Automated Geography to Digital Earth. *Geography and Technology*, S. L. Brunn, Stanley D.and Cutter, and J. W. Harrington, Eds., Springer Netherlands, 81–108, doi:10.1007/978-1-4020-2353-8_5.

Taub, L., 2003: *Ancient Meteorology in Greece and Rome: An Introduction*, 1–14. Routledge.

Tayanc, M., and H. Toros, 1997: Urbanization Effects on Regional Climate Change in the Case of Four Large Cities of Turkey. *Climatic Change*, **35**, 501–524, doi:10.1023/A:1005357915441.

Thielen, J., W. Wobrock, A. Gadian, P. Mestayer, and J.-D. Creutin, 2000: The possible influence of urban surfaces on rainfall development: a sensitivity study in 2D in the meso-$\gamma$-scale. *Atmospheric Research*, **54**, 15–39, doi:10.1016/S0169-8095(00)00041-7.

Tobin, G. A., and B. E. Montz, 2004: *Natural hazards and technology: vulnerability, risk, and community response in hazardous environments*, 547–570. Kluwer Academic Publishers.

Torres, R., and Coauthors, 2012: GMES Sentinel-1 mission. *Remote Sensing of Environment*, **120**, 9–24, doi:10.1016/j.rse.2011.05.028.

Torres, S. M., and C. D. Curtis, 2007: Initial implementation of super-resolution data on the NEXRAD network. *Preprints, 23rd Conf. on Information Processing Systems*, American Meteorological Society, San Antonio, Texas, USA, 5B.10.

Toth, M., R. J. Trapp, J. Wurman, and K. A. Kosiba, 2013: Comparison of Mobile-Radar Measurements of Tornado Intensity with Corresponding WSR-88D Measurements. *Weather and Forecasting*, **28**, 418–426, doi:10.1175/WAF-D-12-00019.1.

Tran, T. V., K. M. de Beurs, and J. P. Julian, 2016: Monitoring forest disturbances in Southeast Oklahoma using Landsat and MODIS images. *International Journal of Applied Earth Observation and Geoinformation*, **44**, 42–52, doi:10.1016/j.jag.2015.07.001.

Trusilova, K., S. Schubert, H. Wouters, B. Früh, S. Grossman-Clarke, M. Demuzere, and P. Becker, 2015: The urban land use in the COSMO-CLM model: a comparison of three parameterizations for Berlin. *Meteorologische Zeitschrift*, **25**, 231–244.

Tucker, C. J., 1979: Red and photographic infrared linear combinations for monitoring vegetation. *Remote Sensing of Environment*, **8**, 127–150, doi:10.1016/0034-4257(79)90013-0.

Turner, C. L., T. R. Seastedt, M. I. Dyer, T. G. F. Kittel, and D. S. Schimel, 1992: Effects of management and topography on the radiometric response of a tallgrass prairie. *Journal of Geophysical Research: Atmospheres*, **97**, 18 855–18 866, doi:10.1029/92JD00654.

United Nations, 2014: World Urbanization Prospects: The 2014 Revision, Highlights. Report, United Nations Department of Economic and Social Affairs, 32 pp.

United States Census Bureau, 2010: Census Urban and Rural Classification and Urban Area Criteria. URL http://www.census.gov/geo/reference/ua/urban-rural-2010.html.

USGS, 2016: Landsat – Earth observation satellites (ver. 1.1, August 2016). U.S. Geological Survey Fact Sheet 2015-3081, United States Geological Survey, 4 pp. doi:10.3133/fs20153081.

van den Heever, S. C., and W. R. Cotton, 2007: Urban Aerosol Impacts on Downwind Convective Storms. *Journal of Applied Meteorology and Climatology*, **46**, 828–850, doi:10.1175/JAM2492.1.

Wagner, M. A., S. W. Myint, and R. S. Cerveny, 2012: Geospatial assessment of recovery rates following a tornado disaster. *IEEE Transactions on Geoscience and Remote Sensing*, **50**, 4313–4322, doi:10.1109/TGRS.2012.2191973.

Walker, J. J., K. M. de Beurs, and G. M. Henebry, 2015: Land surface phenology along urban to rural gradients in the U.S. Great Plains. *Remote Sensing of Environment*, **165**, 42–52, doi:10.1016/j.rse.2015.04.019.

Wang, D., N. Takagi, T. Watanabe, H. Sakurano, and M. Hashimoto, 2008: Observed characteristics of upward leaders that are initiated from a windmill and its lightning protection tower. *Geophysical Research Letters*, **35**, L02 803, doi:10.1029/2007GL032136.

Warner, T. A., K. L. Cummins, and R. E. Orville, 2012: Upward lightning observations from towers in Rapid City, South Dakota and comparison with National Lightning Detection Network data, 2004–2010. *Journal of Geophysical Research: Atmospheres*, **117**, D19 109, doi:10.1029/2012JD018346.

Warner, T. A., T. J. Lang, and W. A. Lyons, 2014: Synoptic scale outbreak of self-initiated upward lightning (SIUL) from tall structures during the central U.S. blizzard of 1–2 February 2011. *Journal of Geophysical Research: Atmospheres*, **119**, 9530–9548, doi:10.1002/2014JD021691.

Watson-Watt, R. A., and J. F. Herd, 1926: An instantaneous direct-reading radiogoniometer. *J. Inst. Elect. Eng.*, **64**, 611–622.

Westcott, N. E., 1995: Summertime Cloud-to-Ground Lightning Activity around Major Midwestern Urban Areas. *Journal of Applied Meteorology*, **34**, 1633–1642, doi:10.1175/1520-0450-34.7.1633.

Whitney Jr., L. F., 1963: Severe Storm Clouds as Seen from TIROS. *Journal of Applied Meteorology*, **2**, 501–507, doi:10.1175/1520-0450(1963)002<0501:SSCASF>2.0.CO;2.

Whiton, R. C., P. L. Smith, S. G. Bigler, K. E. Wilk, and A. C. Harbuck, 1998a: History of Operational Use of Weather Radar by U.S. Weather Services. Part I: The Pre-NEXRAD Era. *Weather and Forecasting*, **13**, 219–243, doi:10.1175/1520-0434(1998)013<0219:HOOUOW>2.0.CO;2.

Whiton, R. C., P. L. Smith, S. G. Bigler, K. E. Wilk, and A. C. Harbuck, 1998b: History of Operational Use of Weather Radar by U.S. Weather Services. Part II: Development of Operational Doppler Weather Radars. *Weather and Forecasting*, **13**, 244–252, doi:10.1175/1520-0434(1998)013<0244:HOOUOW>2.0.CO;2.

Wilkinson, D. W., and M. K. Crosby, 2010: Rapid assessment of forest damage from tornadoes in Mississippi. *Photogrammetric Engineering and Remote Sensing*, **76**, 1298–1301.

Wilks, D. S., 2006: *Statistical Methods in the Atmospheric Sciences: An Introduction*. Academic Press, 467 pp.

Wind Science and Engineering Center, 2006: A recommendation for an enhanced Fujita scale (EF-Scale). Wind science and engineering center technical report, Texas Tech University, 95 pp.

Witt, A., M. D. Eilts, G. J. Stumpf, E. De Wayne Mitchell, J. T. Johnson, and K. W. Thomas, 1998a: Evaluating the Performance of WSR-88D Severe Storm Detection Algorithms. *Weather and Forecasting*, **13**, 513–518, doi:10.1175/1520-0434(1998)013<0513:ETPOWS>2.0.CO;2.

Witt, A., M. D. Eilts, G. J. Stumpf, J. T. Johnson, E. D. W. Mitchell, and K. W. Thomas, 1998b: An Enhanced Hail Detection Algorithm for the WSR-88D. *Weather and Forecasting*, **13**, 286–303, doi:10.1175/1520-0434(1998)013<0286:AEHDAF>2.0.CO;2.

Woodcock, C. E., and Coauthors, 2008: Free access to landsat imagery. *Science*, **320**, 1011–1011, doi:10.1126/science.320.5879.1011a.

Wulder, M. A., J. G. Masek, W. B. Cohen, T. R. Loveland, and C. E. Woodcock, 2012: Opening the archive: How free data has enabled the science and monitoring promise of Landsat. *Remote Sensing of Environment*, **122**, 2–10, doi:10.1016/j.rse.2012.01.010.

Yuan, M., M. Dickens-Micozzi, and M. A. Magsig, 2002: Analysis of Tornado Damage Tracks from the 3 May Tornado Outbreak Using Multispectral Satellite Imagery. *Weather and Forecasting*, **17**, 382–398, doi:10.1175/1520-0434(2002)017<0382:AOTDTF>2.0.CO;2.

Zhang, Y., J. A. Smith, L. Luo, Z. Wang, and M. L. Baeck, 2014: Urbanization and Rainfall Variability in the Beijing Metropolitan Region. *Journal of Hydrometeorology*, **15**, 2219–2235, doi:10.1175/JHM-D-13-0180.1.

Zhou, H., G. Diendorfer, R. Thottappillil, H. Pichler, and M. Mair, 2012: Measured current and close electric field changes associated with the initiation of upward lightning from a tall tower. *Journal of Geophysical Research: Atmospheres*, **117**, D08 102, doi:10.1029/2011JD017269.

Zhu, Z., and C. E. Woodcock, 2012: Object-based cloud and cloud shadow detection in Landsat imagery. *Remote Sensing of Environment*, **118**, 83–94, doi:10.1016/j.rse.2011.10.028.